Metabolic Regulation of Ferroptosis in Pancreatic Cancer

by

Daniel M. Kremer

A dissertation submitted in partial fulfillment
of the requirements for the degree of
Doctor of Philosophy
(Chemical Biology)
in the University of Michigan
2020

Doctoral Committee:

Assistant Professor Costas A. Lyssiotis, Chair
Professor Ruma Banerjee
Professor Charles Burant
Associate Professor Tomasz Cierpicki
Professor Eric R. Fearon

Daniel M. Kremer

dmkremer@umich.edu

ORCID iD: 0000-0001-6224-0550

Dedication

To my peers and professors from the University of St. Thomas Department of Chemistry. Thank you for making science so fun.

Acknowledgements

At the time writing this we are living through a global pandemic, social unrest, and a potential global recession. During the quarantine, I have reflected a considerable amount on my graduate studies and striving to complete the research, herein, has been a positive outlet. The lockdown has provided an abundance of time to think about science and the people who have helped me along the way. I experienced tremendous growth and maturation during my graduate studies, and I would like to thank the people who have inspired me to produce my best work.

First, I need to thank my advisor, Costas, for trusting me and giving me the space to develop as a scientific professional. I have grown a tremendous amount over the last four years in your lab, both personally and professionally. When I first joined the lab, there were four people crammed in a single lab space. The lab has grown tremendously, now including fifteen full-time members. This growth is a testament to your commitment to scientific excellence and nurturing the next generation of scientific professionals. It was fun to be a part of a rapidly growing lab and see how the lab's scientific focus shifted over the years. I am lucky to have had an advisor who trusted me to lead my projects.

I would also like to thank my committee: Ruma Banerjee, Chuck Burant, Tomek Cierpicki, and Eric Fearon for the thoughtful guidance and career advice over the years. I am very grateful for the opportunity to share my work with you and to revive valuable feedback. I also need to thank Brent Martin, who was also on my thesis committee.

I would also like to thank the Lyssiotis Lab for being an energetic group of scientists. I always enjoyed sharing ideas with you. I especially enjoyed learning from the senior lab members: Zachary Tolstyka, Steve Kasperek, Lin Lin, Amy Myers, Chris Halbrook, Zeribe Nwosu, Ilya Kovalenko, Nneka Mbah, and Mengrou Shan. Thank you for your insightful feedback and the willingness to train me.

You have contributed immensely to my scientific development. Moreover, I am deeply grateful for the opportunity to work alongside Stephanie Wisner and mentor Nick Cusmano. Working with you allowed me to improve my leadership and communication skills. More importantly, this opportunity allowed me to get to know you better. Thank you for being great teammates, and I am excited to see what comes next for you all.

I also need to thank several friends who have kept me grounded throughout my time at Michigan. Thank you to Seth Wiley for running Publications to the Public with me. Running an organization is tough; funding an organization is tougher. Thank you for having fun with it and co-creating content. We certainly had a lot of laughs. Thank you, Ryan Smith, Tim Westmark, Alex Moran, Brennen Munley, the University of Michigan Club Hockey Team, and other cubs.

I would also like to thank the mentors who have helped me get here. Thank you to my undergraduate research advisor, Marites Guino-o, who gave me the chance to lead a project, despite being a novice. Working in your lab gave me the confidence to seek answers to my questions and think independently. Thank you for taking me on as a student. Researching at the University of St. Thomas was a fun experience. I would also like to thank Lisa Prevette for encouraging me to pursue my research in chemical biology.

I also need to thank my family. Thank you to my father, Dave, has always been there for me and encouraging me to be tough. Thank you for taking a deep interest in my studies. I am impressed by your new investment in biology, chemistry, and how much you read in general. You are a great role model. Thank you to my mother, Grace, for being a beautiful and sweet person. I am amazed by the things you have done, the places you have been, and all the people you know and love. You are both a constant source of inspiration and love.

Finally, I have to thank my partner, Dana. Your love, resolve, and desire to grow has been a source of inspiration. I am continually learning with you. Thank you for your empathy and support— for giving me the space I needed to finish my studies. I am lucky I am to be with you, and I am beyond excited for our next chapter.

Table of Contents

List of Figures

Abstract

Pancreatic ductal adenocarcinoma (PDA) is a notoriously deadly disease having the lowest 5-year survival rate of any major cancer, owing to a lack of effective therapeutic options. A growing body of evidence demonstrates that PDAs reprogram their metabolism to support growth and survival in response to a harsh metabolic tumor environment. This work studies the hypothesis that metabolism can reveal novel therapeutic targets. Uncovering novel nutrient vulnerabilities could provide new ways to target PDA selectively.

The goals of this work were two-fold. First, we developed analytical methods to identify metabolic changes in PDA and other biological samples. Employing mass spectrometry metabolomics, we profiled over two hundred metabolites in a single experiment across heterogeneous biological samples and experimental conditions. A meta-analysis of these metabolomics studies revealed insights into metabolite reproducibility, providing analytical benchmarks for quality control. Moreover, through systematic analysis we identified stable and dynamic metabolites, where dynamic metabolites play numerous roles in modulating gene expression and signaling. Together, this work provides benchmarks for metabolomics method development and robust analytical frameworks.

Second, we examined nutrient vulnerabilities in PDA to identify novel therapeutic opportunities. We found that pancreatic cancer cells were highly sensitive to cystine deprivation. Cystine was required for the biosynthesis of two versatile redox co-factors, glutathione and coenzyme-A. Starving pancreatic cancer cells and tumors from cysteine triggered ferroptosis: an oxidative, iron-dependent, non-apoptotic form of cell death. Inhibiting cystine metabolism was well tolerated in mice and showed substantial anti-tumor activity, suggesting a new therapeutic strategy for PDA.

In addition to identifying cystine as a metabolic vulnerability, we previously described that pancreatic cancers depend on a cytosolic aspartate aminotransaminase

(GOT1)-dependent pathway for redox balance. Inhibiting GOT1 slowed the growth of PDA cells and tumors. We sought to identify metabolic dependencies induced by GOT1 inhibition as a strategy to kill PDAs selectively. We found cystine, glutathione, and lipid antioxidant function were metabolic susceptibilities following GOT1 suppression. Targeting these metabolic nodes triggered ferroptosis in synergy with GOT1 and delayed tumor growth. This effect was due to labile iron release, which augments ferroptosis sensitivity. Together, this work describes the development of mass spectrometry metabolomics tools and reveals how metabolism and ferroptosis are linked.

This work presents new methods to study ferroptosis in diverse model systems, reconciling long-standing limitations in the field. We identify several metabolic nodes governing ferroptosis susceptibility, building upon the notion that ferroptosis is a metabolically-coupled form of cell death. Finally, we discuss several strategies to harness ferroptosis for therapy that could lead to novel treatments for PDA.

Chapter 1. Pancreatic Cancer: An Unmet Need and Opportunity for Metabolic Intervention

1.1 Disease Overview

As of 2020, the National Cancer Institute estimates that roughly 1.8 million people are diagnosed with cancer in the United States[1]. The most common cancer diagnosis is breast cancer, followed by lung cancer and prostate cancer. Overall, 600,000 people are estimated to die from cancer in the United States this year. Lung cancer is projected to account for most deaths, followed by colorectal and pancreatic cancer [1].

Despite a relatively rare diagnosis, pancreatic ductal adenocarcinoma (PDA) is one of the deadliest solid malignancies. PDA is the third leading cause of cancer-related death and has the lowest 5-year survival rate among the major cancer types. PDA is the most common cancer of the pancreas, accounting for 90% of all pancreatic malignancies[2]. Around 60-70% of PDAs are located in the head of the pancreas, while 20-25% are located in the body and tail[2]. PDA patients are often asymptomatic until late-stage disease, where abdominal pain, weight loss, asthenia, and anorexia are common symptoms[2]. Tumors in the head of the pancreas can cause jaundice, and PDA can induce type 3c diabetes mellitus, which is observed in 50% of patients[2]. PDA is the most lethal major cancer.

The 5-year overall survival of patients with PDA has improved slowly from 2.5% in 1970-1977 to 10% in 2019[1]. 70% of PDA deaths are due to metastatic disease, where the liver, abdomen, and lungs are primary metastatic sites. The remaining 30% of deaths are ascribed to bulky tumors, which impair proper digestive function. Screening, early detection, and novel therapies have enabled significant improvements in overall survival in several major cancers. By contrast, the slow increase in PDA survival rates has been hampered by late-stage diagnosis and therapeutic resistance.

1.2 Risk Factors

PDA is associated with several environmental risk factors. Age is a significant risk factor, as most patients are diagnosed at >50 years of age, with a disease incidence peaking around 70 years of age[3]. Other environmental risk factors include tobacco use and diet. Smokers have a two- to three-fold higher risk for developing PDA over non-smokers, where a higher number of cigarettes correlates with higher risk[4]. Smoking is a source of DNA damaging mutagens in pancreatic cells that increase the probability of gaining an oncogenic mutation. Some dietary patterns are associated with PDA risk. Meta-analysis have associated a “Western Diet” with PDA risk while a “healthy diet” was associated with decreased PDA risk[5]. Obesity and heavy alcohol consumption are also positive dietary risk factors[3]. However, the alcohol association may be confounded by chronic pancreatitis[6]. Chronic pancreatitis increases the risk of PDA by more than ten-fold[3]. Type 2 diabetes mellitus is a risk factor for PDA, where chronic diabetes mellitus doubles the risk for PDA[3]. Diabetes mellitus is also a consequence of early-stage pancreatic cancer. Type 3c diabetes mellitus, the sporadic onset of diabetes mellitus, can provide opportunities for the early diagnosis of PDA. Age, tobacco use, chronic pancreatitis, and type 2 diabetes mellitus are significant environmental risk factors for PDA.

Along with environmental risk factors, several genetic syndromes are associated with PDA risk. About 10% of PDA cases have a familial basis: 3% of these cases possess a causative germline mutation. The remaining 7% of cases lack a germline mutation, but maintain a family history of disease[3]. Hereditary conditions that increase the risk for PDA are linked to mutations in tumor suppressor or DNA damage response genes. Examples of germline mutations in DNA damage response genes include, BRCA1, BRCA2, and localizer of BRCA2 (PALB2), the Fanconi anemia genes *FANCC* and *FANCG*, and ataxia telangiectasia mutated (*ATM*)[3]. Mutations in these genes increase genomic instability during DNA replication and increase the chance for subsequent mutations[7]. Germline mutations in cyclin-dependent kinase (CDK) inhibitor 2A (*CDKN2A*, which encodes $p16^{INK4A}$ and $p19^{ARF}$), is responsible for familial atypical multiple mole melanoma (FAMMM) syndrome, which increases risk for PDA by 13-fold[8].

CDKN2A is a tumor suppressor gene that regulates the G1/S checkpoint of the cell cycle. Somatic mutations in *CDKN2A* contribute to PDA progression, in addition to germline mutations[7]. Patients with inherited mutations in these genes are considered high-risk and are monitored by screening.

Together, these risk factors highlight both environmental and genetic contributions to PDA and suggest potential in-roads for PDA prevention. Screening involves identifying patients with a family history of PDA or identifying patients possessing germline mutations associated with PDA. Periodic screening for high-risk patient groups is being implemented and has improved survival. A recent study demonstrated that early detection of localized cancer can boost 5-year survival to 31.5% from a 10% baseline[8]. Identifying patients who are predisposed to PDA is an attractive strategy. Still, PDA has a low incidence and a lifetime risk of 1.5% in the general population, making disease screening only feasible for high-risk patient groups. 90% of PDA cases lack a familial basis[3,8]. Thus, along with patient screening, research has focused on engineering early detection methods and developing novel therapies.

1.3 Early Detection

Late-stage diagnosis is a major contributing factor to PDA lethality. Often patients are asymptomatic until late-stage disease, and the field lacks sensitive and specific methods to detect early-stage tumors. PDA can take >10 years to generate metastases, which could provide a window for early detection and intervention[3]. Robust PDA markers are needed for early detection, monitoring disease progression, and response to therapy.

The most utilized biomarker is serum cancer antigen 19-9 (CA19-9), a sialylated Lewis-A antigen. CA19-9 is used to monitor PDA progression and therapy response. CA19-9 lacks the sensitivity and specificity required for early PDA detection or screening[3], and 10–15% of the population lack the enzyme necessary to synthesize CA19-9, making CA19-9 a sub-optimal marker[9,10]. By contrast, circulating tumor DNA can be detected in 50% of patients with localized disease and 85% of patients with metastatic disease. Circulating tumor DNA harboring mutant KRAS can be detected in 43% of patients with localized disease. KRAS is a small GTPase that functions as a

growth switch and harbors activating mutations in >90% of PDA patients. Identifying KRAS mutations in circulating tumor DNA is a promising alternative to CA19-9 for early PDA detection. Other blood-based markers include protein panels, exosomes, microRNAs, and the elevation of branched-chained amino acids[3,11]. While these tools could complement current PDA detection approaches in the future, they are currently experimental and have not exhibited clinical utility.

1.4 The PDA Therapeutic Landscape

The lack of effective therapies is a significant barrier to improving overall survival for PDA patients. In 2020 the 5-year overall survival of patients with PDA increased from 2.5% to 10%[1]. Still, PDA has lagged behind advances made in the treatments of other cancers. Early detection of pre-invasive PDA and surgery remains the only chance for a cure, however the majority of patients are diagnosed in later stages or are ineligible for surgery. Surgical resection is associated with a 5-year survival of 15-25%[3]. A Whipple Procedure removes the pancreatic head, while a distal pancreatectomy removes tumors in the pancreatic tail. 10-20% of patients have a resectable disease, and 30-40% of patients present with borderline resectable PDA. A majority (50-60%) of patients are ineligible for surgery and present with locally advanced/unresectable pancreatic cancer[3]. Among these patients eligible for surgery, 20% of patients will survive five years following surgical resection and adjuvant therapy[3]. Surgery is a mildly effective, but risky therapeutic option, for patients with localized disease.

Cytotoxic chemotherapies are the primary treatment option for patients with advanced or refractory disease. These therapies provide little survival benefit, as PDA is highly resistant to chemotherapy. The current standard of care is a chemotherapy cocktail consisting of 5-fluorouracil, leucovorin, irinotecan, and oxaliplatin (FOLFIRINOX) or combinations lacking 5-fluorouracil (mFOLFIRINOX)[12]. Therapeutic limitations include a low prevalence of tractable mutations[3], the lack of predictive biomarkers[12], a desmoplastic stroma that can impede drug delivery[13], and an immune suppressive tumor microenvironment[14]. Thus, novel therapies that overcome these limitations are desperately needed. Both pre-clinical and clinical research in targeted

therapy, immune therapy, and metabolic therapy offer novel therapeutic strategies for improving PDA treatment.

Targeted Therapy

The genomic landscape of PDA has been known for decades, but the translation of this information into novel therapies has recently emerged. Several studies have profiled the whole genomes of PDA patient cohorts to classify tumor subtypes to facilitate treatment and provide biomarkers for patient stratification[15–17]. These studies have revealed a small number (<14%) of clinically actionable mutations in DNA maintenance genes (*BRCA1, BRCA2* or *PALB2*) representing a "genomically unstable subtype."[15] Importantly, this molecular subtype predicted responsiveness to platinum-based chemotherapy.

Loss-of-function mutations in *BRCA1/2* or *PALB2*, which are essential for DNA damage repair, are potential markers for the application of poly (ADP-ribose) polymerase (PARP) inhibitors. PARP is a critical DNA damage repair enzyme that recognizes and repairs single-strand DNA breaks. PARP enzymes repair DNA damage in parallel with BRCA1/2 and PALB2. PARP inhibition combined with *BRCA1/2* or *PALB2* loss-of-function mutations results in cell death from a defective DNA damage response. Several clinical trials are investigating PARP inhibitors in patients with a germline or somatic BRCA1/2 or PALB2 mutations[12]. Only around 14% of PDA patients have these genetic alterations, and more broadly, up to 24% of patients have mutations in other genes that encode for DNA damage response proteins. PARP inhibitors as a single agent or in combination in patients harboring these genetic alterations are ongoing[12]. PARP inhibitors are promising, albeit limited, application of targeted therapy in PDA.

By contrast, oncogenic mutations in KRAS mutations are found in >90% and is the driver mutation in of PDA. Mutant KRAS isoforms have been notoriously difficult to target owing to their high affinity for GTP and GDP substrates[18]. Recently, allele-specific inhibitors against $KRAS^{G12C}$ have shown promise in both pre-clinical models and early phase trials[19]. These $KRAS^{G12C}$ inhibitors disrupt cancer cell growth and promote the infiltration of $CD8^+$ T cells into the immune microenvironment. For example, the $KRAS^{G12C}$ inhibitor AMG-510 combined, with a PD-1 inhibitor led to durable cures in

mice and protected mice against subsequent tumor challenge[19,20]. This observation was consistent with studies demonstrating that oncogenic KRAS signaling promotes an immune-suppressive tumor microenvironment. Despite these promising results, there are several limitations. The $KRAS^{G12C}$ mutation accounts for only ~1% of PDA patients[12]. Several groups are exploring the possibility of pan-RAS inhibitors, offering a promising alternative[20]. Tumor resistance is another caveat to RAS inhibition, and several mechanisms of resistance have been established in PDA and other cancers. Thus, combination therapy is likely needed to improve the anti-tumor efficacy of KRAS or RAS inhibitors[19–23]. Overall, the translation of targeted therapies against the genomic landscape of PDA is emerging.

Immune Therapy

Cancer is characterized by the expression of signals that distinguish them from normal cells[24]. Cancer neoantigens can be presented by MHC class I molecules on the surface of cancer cells, enabling recognition and activation of anti-tumor immunity[25]. Anti-tumor immunity is a highly regulated process requiring the coordination between innate and adaptive immune and cells in the tumor microenvironment[25]. The goal of cancer immune therapy is to direct the processes of anti-tumor immune regulation for therapeutic benefit.

Here, we refer to immune therapy as immune checkpoint inhibitors, which block negative regulators of a $CD8^+$ T cell anti-tumor response, although other immune therapy modalities exist. Established immune checkpoint inhibitors include anti-CTLA4, anti-PD1, and anti-PD-L1 blocking antibodies that have shown efficacy in specific tumor types but have been ineffective in PDA[12].

PDAs have been resistant to immunotherapy owing to a relatively low tumor mutational burden, a dense desmoplastic stroma, and an immune-suppressive tumor microenvironment. PDA has a low tumor mutational burden compared with tumors that respond to immune checkpoint inhibitors, where tumor mutational burden is associated with responsiveness to these therapies[26,27]. A high mutation burden can promote the formation of cancer neoantigens that facilitate tumor-specific killing by $CD8^+$ T cells[24]. The dense fibrotic stroma in PDA poses a physical barrier to cytotoxic T cells[28] and stromal cells release factors that inhibit $CD8^+$ T cell survival and function. For example,

inhibitory cell populations within the stroma, such as myeloid cells and Tregs, restrict anti-tumor immunity. Low mutational burden and an immune suppressive tumor microenvironment also hinder immunotherapy for PDA. Immune therapies would likely need to be harnessed in combination to achieve anti-tumor immunity.

Current efforts aim to identify combination therapies that block immune-suppressive components and augment immune checkpoint inhibitors. Example combinations harness targeted therapy, metabolic therapy, or other immune therapy strategies to improve immune checkpoint inhibitor safety and efficacy. Indeed, several clinical trials are evaluating this concept[12,32]. While immune therapy has emerged as a new treatment option for immunogenic tumor types, PDA has been refractory. Many clinical and pre-clinical studies are aiming to overcome immune suppression in PDA through combinations with immune checkpoint therapy.

Metabolic Therapy

Metabolic alterations accompany the onset of PDA and offer many therapeutic in-roads. Vascular collapse, impaired perfusion, and hypoxia follow the signature desmoplastic reaction. These collective insults promote a nutrient-deprived and harsh tumor microenvironment[28,29]. PDA cells adapt their metabolism to support survival and growth under these harsh conditions **(Figure 1)**[30]. These metabolic changes occur in PDA cells and the tumor microenvironment. Metabolic reprogramming of the tumor microenvironment contribute to therapeutic resistance. Importantly, cancer-specific metabolic reprogramming may provide a therapeutic window and reveal new therapeutic targets[31,32].Metabolic reprogramming in PDA cells is a result of oncogene activation. Two primary carbon sources include glucose and glutamine that provide biosynthetic and bioenergetic substrates[31]. Oncogenic KRAS promotes the upregulation of glycolysis and shunting of glucose carbon into biosynthetic pathways. Two of these upregulated pathways include the hexosamine biosynthetic pathway, which supports glycosylation, and the non-oxidative pentose phosphate pathway, which provides a carbon source for DNA and RNA synthesis **(Figure 1)**[33]. Oncogenic KRAS reprograms glutamine metabolism to support NADPH production and redox homeostasis[34]. Oncogenic KRAS enables nutrient scavenging through macropinocytosis **(Figure 1)**, a process involving the bulk engulfment of extracellular fluid.

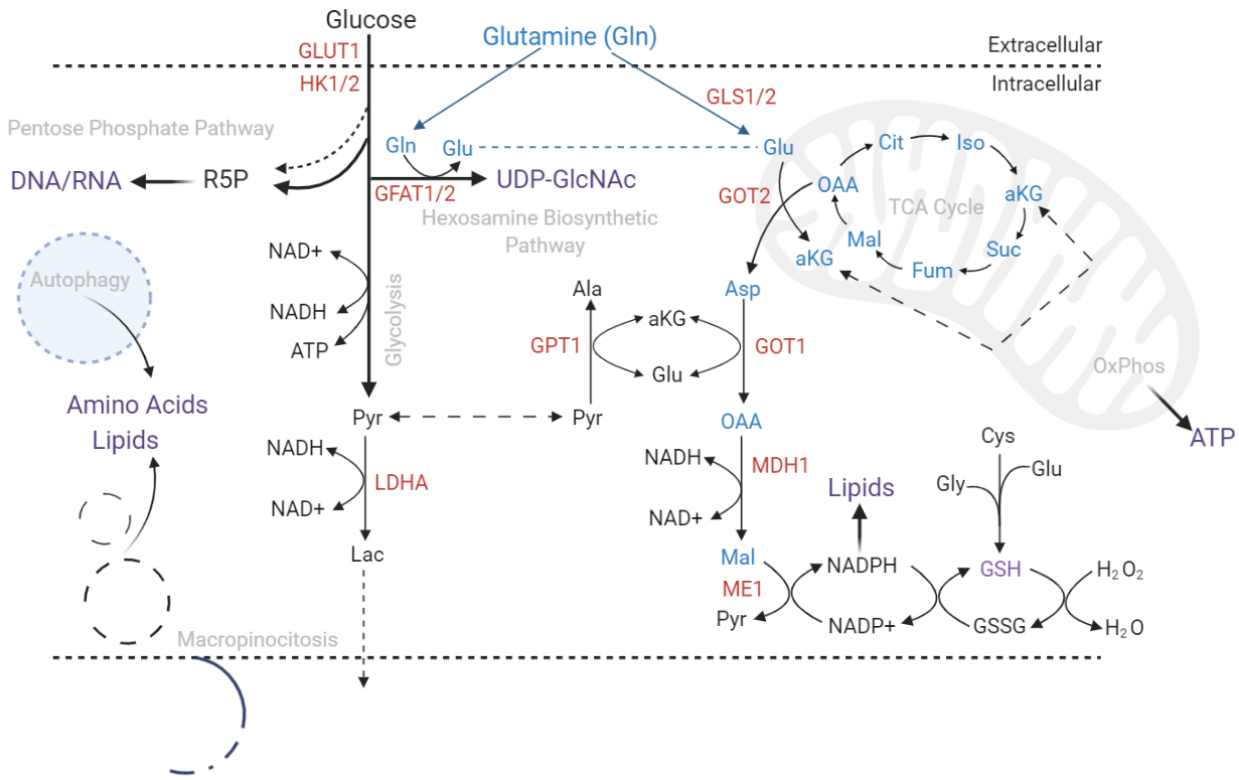

Figure 1. Metabolic reprogramming in PDA.
Glucose and glutamine are primary inputs to PDA metabolism. Major biosynthetic outputs include DNA/RNA, UDP-GlcNAc, amino acids, lipids, and reduced glutathione (GSH). Key enzymes in intermediary metabolism are in red. Glutamine metabolism is in blue. Adapted from reference #29.

Macropinocytosis is a mechanism by which PDA cells scavenge proteins,[35,36] lipids,[37] and necrotic cells[38] from the surrounding environment. Interestingly, oncogenic KRAS ablation promotes a population of resistant cells sensitive to inhibition of Oxidative Phosphorylation (OxPhos)[22,23]. Overall, oncogenic KRAS reprograms several metabolic pathways in PDA to support biosynthesis, redox balance, and nutrient acquisition.

PDA cells are highly influenced by the local nutrient environment, in addition to KRAS-mediated metabolic reprogramming. The metabolism of PDA is highly plastic and alters metabolic programs in response to nutrient availability[39]. Mayers et al. demonstrated differences in branched-chain amino acid catabolism in PDA versus cancers harboring KRAS[11]. PDAs have elevated autophagy **(Figure 1)**, a nutrient scavenging process that is regulated by nutrient access and energetic balance. Under conditions of metabolic stress, autophagy degrades cellular organelles and macromolecules to support metabolic homeostasis. Autophagy provides amino acids that facilitates PDA growth under nutrient deprevation[40,41,42]. PDAs are highly sensitive

to autophagy inhibition as genetic or pharmacological inhibition of autophagy machinery is sufficient to stunt tumor growth in PDA mouse models[40,42]. KRAS suppression or ERK inhibition enhances autophagy dependence. Inhibition of autophagy and ERK signaling synergizes *in vivo*, demonstrating a promising combination strategy[43]. Early phase clinical trials are targeting autophagy in combination with chemotherapy (NCT01506973) or ERK inhibition (NCT03825289). Overall, PDA exhibits extensive cell-autonomous metabolic reprogramming to support growth and survival.

Fibroblasts and immune cells outnumber cancer cells in PDA tumors and play a significant role in the metabolic reprogramming of PDA tumors. New data demonstrate that fibroblasts and immune cells share a dynamic metabolic relationship with PDA by engaging in reciprocal nutrient exchange[44]. PDAs are proficient in capturing metabolites through metabolite cross-talk with neighboring cells. PDA signal to cancer-associated fibroblasts (CAFs) to release alanine to support OxPhos in PDA cells[41] and CAFs can support PDA through metabolites released from exosomes[45].

PDA cells can also participate in metabolite transfer with the immune system. Tumor-educated macrophages (TEMs) release deoxycytidine that inhibits gemcitabine treatment in PDA[46]. At the same time, tumor-derived lactate promotes macrophage polarization toward the TEM state[47]. Lactate mediates the expression Ariginase1 (Arg1), which is a molecular marker for TEMs[47]. Arg1 degrades arginine, which promotes an immune suppressive environment. Arginine is unique among the amino acids because it mediates $CD8^+$ T cell survival, anti-tumor immunity, and memory[48]. The combination of Arg1 inhibitors and immune checkpoint inhibitors are undergoing clinical investigation in advanced-stage solid tumors (NCT02903914). These brief examples illustrate the complex metabolic interactions within the PDA tumor environment that provide novel opportunities for therapeutic harnessing.

Systemic metabolic reprogramming contributes to the onset of PDA. Conditions such as obesity and Type 2 diabetes mellitus are risk factors for PDA[3]. Obesity increases PDA risk by 20-50% and shows an increase in risk proportional to body mass index[49] and an increased number of PanIN lesions in patients[50]. Obesity may influence the onset of PDA through multiple and cooperative mechanisms. A high-fat diet, for example, is associated with the activation of inflammatory pathways and can contribute

to early-stage lesions[55,56] . A high-fat diet cooperates with oncogenic KRAS to promote tumorigenesis and is correlated with decreased survival in KRAS-Cre mice[57]. Thus, systemic metabolism can influence the onset of PDA.

PDA can influence systemic metabolism. PDA promotes cachexia, which is associated with more aggressive tumors and poor prognosis[30]. PDA can promote adipose tissue loss, which could be linked to declining exocrine pancreas function[58]. Tissue and muscle atrophy occur early in PDA development. Mayers et al. reported that elevated circulating branched chained amino acids (BCAAs) are present 2-5 years before tumor diagnosis. Elevated BCAA levels were associated with a 2-fold risk of developing PDA. A greater understanding of the reciprocal relationship between PDA and systemic metabolism could yield novel biomarkers and therapeutic opportunities.

New studies are harnessing dietary intervention for therapy. Diet can influence the local nutrient environment in tumors[51,52] and modulate therapeutic response[53,54]. In mice, a high-fat diet can promote tumor growth, while caloric restriction can inhibit tumor growth[52]. Recent studies are examining the possibility of combining dietary intervention with targeted therapy. For example, Hopkins et al. demonstrated that dietary manipulation of insulin improves the anti-tumor effect of PI3K inhibitors[54]. Understanding the mechanisms by which dietary intervention can influence therapy response is an attractive application of metabolic therapy.

PDA adapt their metabolism to facilitate survival and immune suppression. The metabolic reprogramming occurring in tumors has a far-reaching impact on systemic metabolism. Understanding the mechanisms of metabolic reprogramming in PDA is revealing novel therapeutic strategies.

1.5 Dissertation Summary

Better therapeutic strategies and early detection are needed to improve PDA outcomes. Targeted therapies, immune therapies, and metabolic therapies provide novel opportunities to combat PDA. This work studies the hypothesis that metabolism can reveal novel therapeutic targets, given that metabolism is heavily altered in this disease. Uncovering novel nutrient vulnerabilities could provide new ways to target PDA selectively.

Here, we developed a targeted mass spectrometry metabolomics platform to study the metabolism PDA **(Chapter 2)**. We then used this method to identify cysteine **(Chapter 3)**, redox, and iron metabolism **(Chapter 4)** as novel metabolic vulnerabilities. While these therapeutic opportunities are still in the early stages, the discoveries made here could lead to innovative therapeutic strategies **(Conclusions and Future Directions)**.

1.6 Chapter 1 References

1. Siegel, R. L., Miller, K. D. & Jemal, A. Cancer statistics, 2020. *CA: A Cancer Journal for Clinicians* **70**, 7–30 (2020).

2. Ryan, D. P., Hong, T. S. & Bardeesy, N. Pancreatic Adenocarcinoma. *New England Journal of Medicine* **371**, 1039–1049 (2014).

3. Kleeff, J. *et al.* Pancreatic cancer. *Nature Reviews Disease Primers* **2**, 1–22 (2016).

4. Bosetti, C. *et al.* Cigarette smoking and pancreatic cancer: an analysis from the International Pancreatic Cancer Case-Control Consortium (Panc4). *Ann Oncol* **23**, 1880–1888 (2012).

5. Lu, P.-Y., Shu, L., Shen, S.-S., Chen, X.-J. & Zhang, X.-Y. Dietary Patterns and Pancreatic Cancer Risk: A Meta-Analysis. *Nutrients* **9**, (2017).

6. Tramacere, I. *et al.* Alcohol drinking and pancreatic cancer risk: a meta-analysis of the dose-risk relation. *Int. J. Cancer* **126**, 1474–1486 (2010).

7. Kinzler, K. W. & Vogelstein, B. Gatekeepers and caretakers. *Nature* **386**, 761–763 (1997).

8. Llach, J., Carballal, S. & Moreira, L. Familial Pancreatic Cancer: Current Perspectives. *Cancer Manag Res* **12**, 743–758 (2020).

9. Bettegowda, C. *et al.* Detection of Circulating Tumor DNA in Early- and Late-Stage Human Malignancies. *Sci Transl Med* **6**, 224ra24 (2014).

10. Sausen, M. *et al.* Clinical implications of genomic alterations in the tumour and circulation of pancreatic cancer patients. *Nat Commun* **6**, 7686 (2015).

11. Mayers, J. R. *et al.* Elevation of circulating branched-chain amino acids is an early event in human pancreatic adenocarcinoma development. *Nature Medicine* **20**, 1193–1198 (2014).

12. Nevala-Plagemann, C., Hidalgo, M. & Garrido-Laguna, I. From state-of-the-art treatments to novel therapies for advanced-stage pancreatic cancer. *Nature Reviews Clinical Oncology* **17**, 108–123 (2020).

13. Olive, K. P. *et al.* Inhibition of Hedgehog Signaling Enhances Delivery of Chemotherapy in a Mouse Model of Pancreatic Cancer. *Science* **324**, 1457–1461 (2009).

14. Zhang, Y., Crawford, H. C. & Pasca di Magliano, M. Epithelial-Stromal Interactions in Pancreatic Cancer. *Annual Review of Physiology* **81**, null (2019).

15. Waddell, N. *et al.* Whole genomes redefine the mutational landscape of pancreatic cancer. *Nature* **518**, 495–501 (2015).

16. Bailey, P. *et al.* Genomic analyses identify molecular subtypes of pancreatic cancer. *Nature* **531**, 47–52 (2016).

17. Dreyer, S. B., Chang, D. K., Bailey, P. & Biankin, A. V. Pancreatic Cancer Genomes: Implications for Clinical Management and Therapeutic Development. *Clin Cancer Res* **23**, 1638–1646 (2017).

18. Cox, A. D., Fesik, S. W., Kimmelman, A. C., Luo, J. & Der, C. J. Drugging the undruggable RAS: Mission Possible? *Nature Reviews Drug Discovery* **13**, 828–851 (2014).

19. Canon, J. *et al.* The clinical KRAS(G12C) inhibitor AMG 510 drives anti-tumour immunity. *Nature* **575**, 217–223 (2019).

20. Sheridan, C. Grail of RAS cancer drugs within reach. *Nature Biotechnology* **38**, 6–8 (2020).

21. Kapoor, A. *et al.* Yap1 Activation Enables Bypass of Oncogenic Kras Addiction in Pancreatic Cancer. *Cell* **158**, 185–197 (2014).

22. Viale, A. *et al.* Oncogene ablation-resistant pancreatic cancer cells depend on mitochondrial function. *Nature* **514**, 628–632 (2014).

23. Muzumdar, M. D. *et al.* Survival of pancreatic cancer cells lacking KRAS function. *Nature Communications* **8**, 1–19 (2017).

24. Schumacher, T. N. & Schreiber, R. D. Neoantigens in cancer immunotherapy. *Science* **348**, 69–74 (2015).

25. Chen, D. S. & Mellman, I. Oncology Meets Immunology: The Cancer-Immunity Cycle. *Immunity* **39**, 1–10 (2013).

26. Alexandrov, L. B. *et al.* Signatures of mutational processes in human cancer. *Nature* **500**, 415–421 (2013).

27. Yarchoan, M., Hopkins, A. & Jaffee, E. M. Tumor Mutational Burden and Response Rate to PD-1 Inhibition. *New England Journal of Medicine* **377**, 2500–2501 (2017).

28. Koong, A. C. *et al.* Pancreatic tumors show high levels of hypoxia. *Int. J. Radiat. Oncol. Biol. Phys.* **48**, 919–922 (2000).

29. Halbrook, C. J. & Lyssiotis, C. A. Employing Metabolism to Improve the Diagnosis and Treatment of Pancreatic Cancer. *Cancer Cell* **31**, 5–19 (2017).

30. Perera, R. M. & Bardeesy, N. Pancreatic Cancer Metabolism: Breaking It Down to Build It Back Up. *Cancer Discov* **5**, 1247–1261 (2015).

31. Vander Heiden, M. G. Targeting cancer metabolism: a therapeutic window opens. *Nature Reviews Drug Discovery* **10**, 671–684 (2011).

32. Li, X. *et al.* Navigating metabolic pathways to enhance antitumour immunity and immunotherapy. *Nature Reviews Clinical Oncology* **16**, 425–441 (2019).

33. Ying, H. *et al.* Oncogenic Kras Maintains Pancreatic Tumors through Regulation of Anabolic Glucose Metabolism. *Cell* **149**, 656–670 (2012).

34. Son, J. *et al.* Glutamine supports pancreatic cancer growth through a KRAS-regulated metabolic pathway. *Nature* **496**, 101–105 (2013).

35. Commisso, C. *et al.* Macropinocytosis of protein is an amino acid supply route in Ras-transformed cells. *Nature* **497**, 633–637 (2013).

36. Kamphorst, J. J. *et al.* Human Pancreatic Cancer Tumors Are Nutrient Poor and Tumor Cells Actively Scavenge Extracellular Protein. *Cancer Res* **75**, 544–553 (2015).

37. Kamphorst, J. J. *et al.* Hypoxic and Ras-transformed cells support growth by scavenging unsaturated fatty acids from lysophospholipids. *PNAS* **110**, 8882–8887 (2013).

38. Kim, S. M. *et al.* PTEN Deficiency and AMPK Activation Promote Nutrient Scavenging and Anabolism in Prostate Cancer Cells. *Cancer Discov* **8**, 866–883 (2018).

39. Biancur, D. E. *et al.* Compensatory metabolic networks in pancreatic cancers upon perturbation of glutamine metabolism. *Nature Communications* **8**, 15965 (2017).

40. Yang, S. *et al.* Pancreatic cancers require autophagy for tumor growth. *Genes Dev.* **25**, 717–729 (2011).

41. Sousa, C. M. *et al.* Pancreatic stellate cells support tumour metabolism through autophagic alanine secretion. *Nature* **536**, 479–483 (2016).

42. Yang, A. *et al.* Autophagy Sustains Pancreatic Cancer Growth through Both Cell-Autonomous and Nonautonomous Mechanisms. *Cancer Discov* **8**, 276–287 (2018).

43. Bryant, K. L. *et al.* Combination of ERK and autophagy inhibition as a treatment approach for pancreatic cancer. *Nature Medicine* **25**, 628–640 (2019).

44. Lyssiotis, C. A. & Kimmelman, A. C. Metabolic Interactions in the Tumor Microenvironment. *Trends Cell Biol.* **27**, 863–875 (2017).

45. Zhao, H. *et al.* Tumor microenvironment derived exosomes pleiotropically modulate cancer cell metabolism. *eLife* **5**, e10250 (2016).

46. Halbrook, C. J. *et al.* Macrophage-Released Pyrimidines Inhibit Gemcitabine Therapy in Pancreatic Cancer. *Cell Metab.* **29**, 1390-1399.e6 (2019).

47. Colegio, O. R. *et al.* Functional polarization of tumour-associated macrophages by tumour-derived lactic acid. *Nature* **513**, 559–563 (2014).

48. Geiger, R. *et al.* L-Arginine Modulates T Cell Metabolism and Enhances Survival and Anti-tumor Activity. *Cell* **167**, 829-842.e13 (2016).

49. Bracci, P. M. Obesity and pancreatic cancer: Overview of epidemiologic evidence and biologic mechanisms. *Molecular Carcinogenesis* **51**, 53–63 (2012).

50. Rebours, V. *et al.* Obesity and Fatty Pancreatic Infiltration Are Risk Factors for Pancreatic Precancerous Lesions (PanIN). *Clin. Cancer Res.* **21**, 3522–3528 (2015).

51. Sullivan, M. R. *et al.* Quantification of microenvironmental metabolites in murine cancers reveals determinants of tumor nutrient availability. *eLife* **8**, e44235 (2019).

52. Lien, E. C. & Vander Heiden, M. G. A framework for examining how diet impacts tumour metabolism. *Nature Reviews Cancer* **19**, 651–661 (2019).

53. Nencioni, A., Caffa, I., Cortellino, S. & Longo, V. D. Fasting and cancer: molecular mechanisms and clinical application. *Nat Rev Cancer* **18**, 707–719 (2018).

54. Hopkins, B. D. *et al.* Suppression of insulin feedback enhances the efficacy of PI3K inhibitors. *Nature* **560**, 499–503 (2018).

55. Pushalkar, S. *et al.* The Pancreatic Cancer Microbiome Promotes Oncogenesis by Induction of Innate and Adaptive Immune Suppression. *Cancer Discov* **8**, 403–416 (2018).

56. Schulz, M. D. *et al.* High-fat-diet-mediated dysbiosis promotes intestinal carcinogenesis independently of obesity. *Nature* **514**, 508–512 (2014).

57. Philip, B. *et al.* A High-Fat Diet Activates Oncogenic Kras and COX2 to Induce Development of Pancreatic Ductal Adenocarcinoma in Mice. *Gastroenterology* **145**, 1449–1458 (2013).

58. Danai, L. V. *et al.* Altered exocrine function can drive adipose wasting in early pancreatic cancer. *Nature* **558**, 600–604 (2018).

Chapter 2. A Large-Scale Analysis of Targeted Metabolomics Data from Heterogeneous Biological Samples Provides Insights into Metabolite Dynamics[1]

2.1 Abstract

We developed a tandem mass spectrometry-based label-free targeted metabolomics analysis framework employing two distinct chromatographic methods, reversed-phase liquid chromatography (RPLC) and hydrophilic interaction liquid chromatography (HILIC), coupled with dynamic multiple reaction monitoring (dMRM), to detect over 200 metabolites in core metabolic pathways. We sought to establish a systematic framework to access measurement quality in biological replicate groups and to investigate metabolite abundance changes and patterns across different biological conditions. We applied our metabolomics instrument platform and analysis framework across wide-range of experimental systems including cancer cell lines, tumors, extracellular media, primary cells, immune cells, organoids, organs (e.g. pancreata), tissues, and sera from human and mice. We generated a compendium of 42 heterogeneous deidentified datasets with 635 samples using both RPLC and HILIC methods. Our method revealed metabolite signatures that correspond to various phenotypes of the heterogeneous datasets and involve several metabolic pathways. Moreover, we found the RPLC method shows overall better reproducibility than the HILIC method for most metabolites including polar amino acids. Correlation analysis reveals high confidence metabolites irrespective of experimental systems such asmethionine, phenylalanine, and taurine. We also identify homocystine, reduced glutathione, and phosphoenolpyruvic acid as highly dynamic metabolites across all

[1]The content of this chapter were adapted and reproduced from a published co-first authored article:
Lee, H.-J., **Kremer, D. M.***, Sajjakulnukit, P.*, Zhang, L. & Lyssiotis, C. A. A large-scale analysis of targeted metabolomics data from heterogeneous biological samples provides insights into metabolite dynamics. *Metabolomics* **15**, 103 (2019).

case-control paired samples. Overall, our study may serve as a reference point for a systematic analysis of label-free LC–MS/MS targeted metabolomics data in both RPLC and HILIC methods with dMRM.

2.2 Introduction

Mass spectrometry (MS) is a popular and powerful platform for metabolomics studies[99–101]. Although nuclear magnetic resonance (NMR)-based metabolomics is also widely used, MS is more easily coupled to various chromatographic columns to separate analytes prior to analysis, thereby reducing the complexity of a biological sample and increasing sensitivity for simultaneous detection of a large number of metabolites[102,103]

MS-based metabolomics is performed predominantly by subjecting samples to chromatographic separation before MS analysis. Chromatographic columns make it possible to separate complex analyte mixtures based on physicochemical properties of a wide range of compounds, including isomers. Liquid chromatography (LC) is most frequently used, while gas chromatography (GC) is preferred for measuring volatile compounds. LC methods include reversed-phase liquid chromatography (RPLC) and hydrophilic interaction liquid chromatography (HILIC). RPLC is typically used for a broad range of metabolites, especially nonpolar and weakly polar metabolites, whereas HILIC has a complementary usage for hydrophilic, polar, and ionic metabolites such as sugars, amino acids, and nucleic acids[104–109], where a recent study performed a systematic evaluation of chromatographic methods in LC–MS metabolomics[110].

We previously developed a tandem mass spectrometry-based targeted metabolomics system that profiles abundance of more than 200 metabolites as a steady-state snapshot of global metabolism. It utilizes both RPLC and HILIC methods with dynamic MRM (dMRM) as a means to maximize the coverage and sensitivity of target metabolites. Together with our customized computational and statistical analysis pipelines, this system has been recently applied in several biological contexts[39,50,111,112]. Herein, we report heterogeneous data sets generated from a wide-range of experiments and sample types using our LC–MS/MS targeted metabolomics platforms over a period of about 1 year from 2017 to 2018. The data were collected with no specific criteria to

both be unbiased and include as much data as possible. Using these, we carried out comprehensive global meta-analysis in which we systematically evaluated data quality of both RPLC and HILIC methods by statistical measures and characterized global patterns of metabolite changes and variability in case versus control groups.

2.3 Results

Global Visualization of LC-MS/MS Data across Heterogeneous Datasets

A flowchart overview of our approach in this study is depicted in **(Figure 2)**. We compiled 42 datasets of LC–MS/MS-based targeted metabolomics with both RPLC-Pos-dMRM and HILIC-Neg-dMRM methods. There are a total of 638 samples analyzed, which include cancer cell lines, tumors, extracellular media, primary cells, immune cells, organoids, organs (e.g. pancreata), tissues, sera, and shRNA/drug treatments in human and mice. A total of 448 measurements were made in both methods for 285 unique compound entities (due to multiple detection). We retained measurements for those

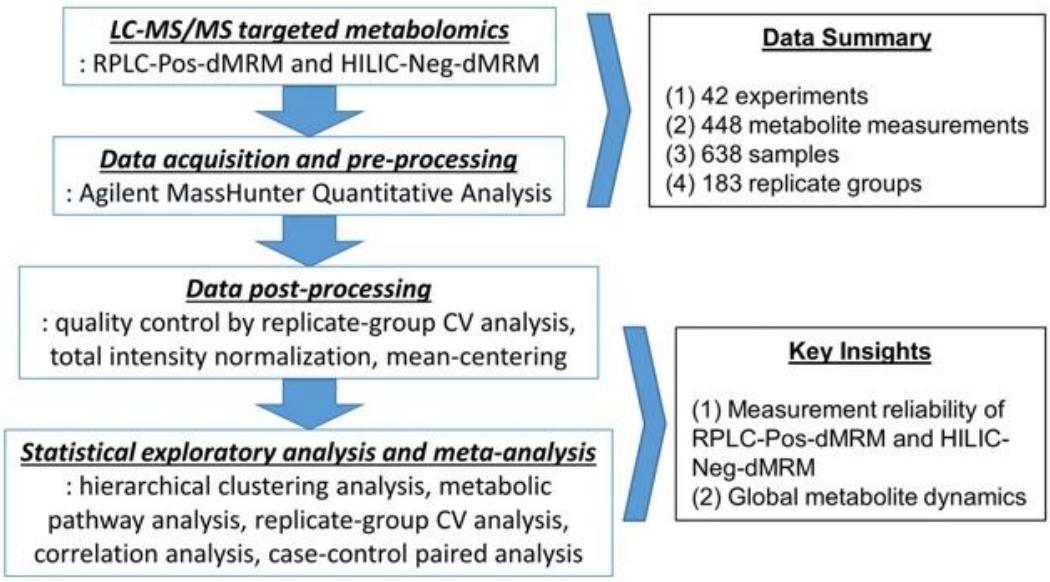

Figure 2. A flowchart and a summary of our LC-MS/MS analytical pipeline. Produced in collaboration with Dr. Ho-Joon Lee.

metabolites detected in both RPLC-Pos-dMRM and HILIC-Neg-dMRM methods as independent measurements. From this compendium we constructed a 448 by 638 data matrix for global characterization. 36.7% of the values in this data matrix were missing, and we removed 11 samples where no compound was measured. We find that this is a

generic problem associated with generating metabolomics data in a large number of heterogeneous samples, especially with the HILIC method. It relates to several factors including general metabolite stability (e.g. succinate and fumarate), poor ionization efficiency of some metabolites such as carbohydrates, large dynamic ranges of certain metabolites in different cell/tissue types (e.g. GABA and certain carbohydrates), and complex matrix effects.

Figure 3a depicts a correlation heat map and a hierarchical clustering of all metabolites in both RPLC-Pos-dMRM and HILIC-Neg-dMRM methods. **Figure 3b** shows a correlation heat map and a hierarchical clustering of all samples. We find that there are a few groups of highly correlated metabolites. For example, at the height of 6 in the dendrogram tree, the 31 metabolites in Cluster #1 are enriched in purine, pyrimidine, glycine/serine, and glutathione metabolism, and the 88 metabolites in Cluster #2 include metabolites in the TCA cycle, glycolysis, pyruvate, and phenylalanine/tyrosine/tryptophan metabolism **(Figure 3c)**. This suggests that those metabolites tend to change their abundance in the same direction across different conditions, which suggests that they are subject to pathway-level metabolic regulation. The lack of clustering among samples reflects the heterogeneous nature of all datasets and indicates that experimental bias is not driving clustering and influencing downstream analysis. In fact, the most highly correlated 25 samples (Cluster #3, **Figure 3c)** do not exhibit common phenotypes, and this cluster includes cell lines, murine tumors and several experimentally distinct variables. Therefore, it suggests the existence of general metabolic phenotypes that can arise from various perturbations, independent of cell/tissue types.

Analysis of Normalized Relative Abundance

Raw data from the LC–MS/MS analysis are peak areas of ion counts for each identified metabolite. These raw data do not reflect absolute abundance and cannot be compared directly between experiments run at different times. Instead we normalized each sample by the total ion counts of all metabolites to approximately correct equal sample loading. Then, each metabolite abundance value was divided by the mean of all abundance values across all samples in each experiment, defined as normalized relative abundance, i.e., $A*ij$ (see Materials and Methods).

We first examined normalized relative abundance distributions of all metabolites across all datasets using medians in replicate-group measurements. **Figure 4a** shows the number of median measurements for each metabolite across all 183 replicate groups. There are a total of 13,026 measurements for 448 metabolites in both RPLC-Pos-dMRM and HILIC-Neg-dMRM methods in the 42 experiments. 71 metabolites were measured in all 183 replicate groups **(Figure 4a)**. All of these came from the RPLC-Pos-dMRM method. This may indicate that the RPLC-Pos-dMRM method is more robust in detecting those metabolites than the HILIC-Neg-dMRM method. Those most

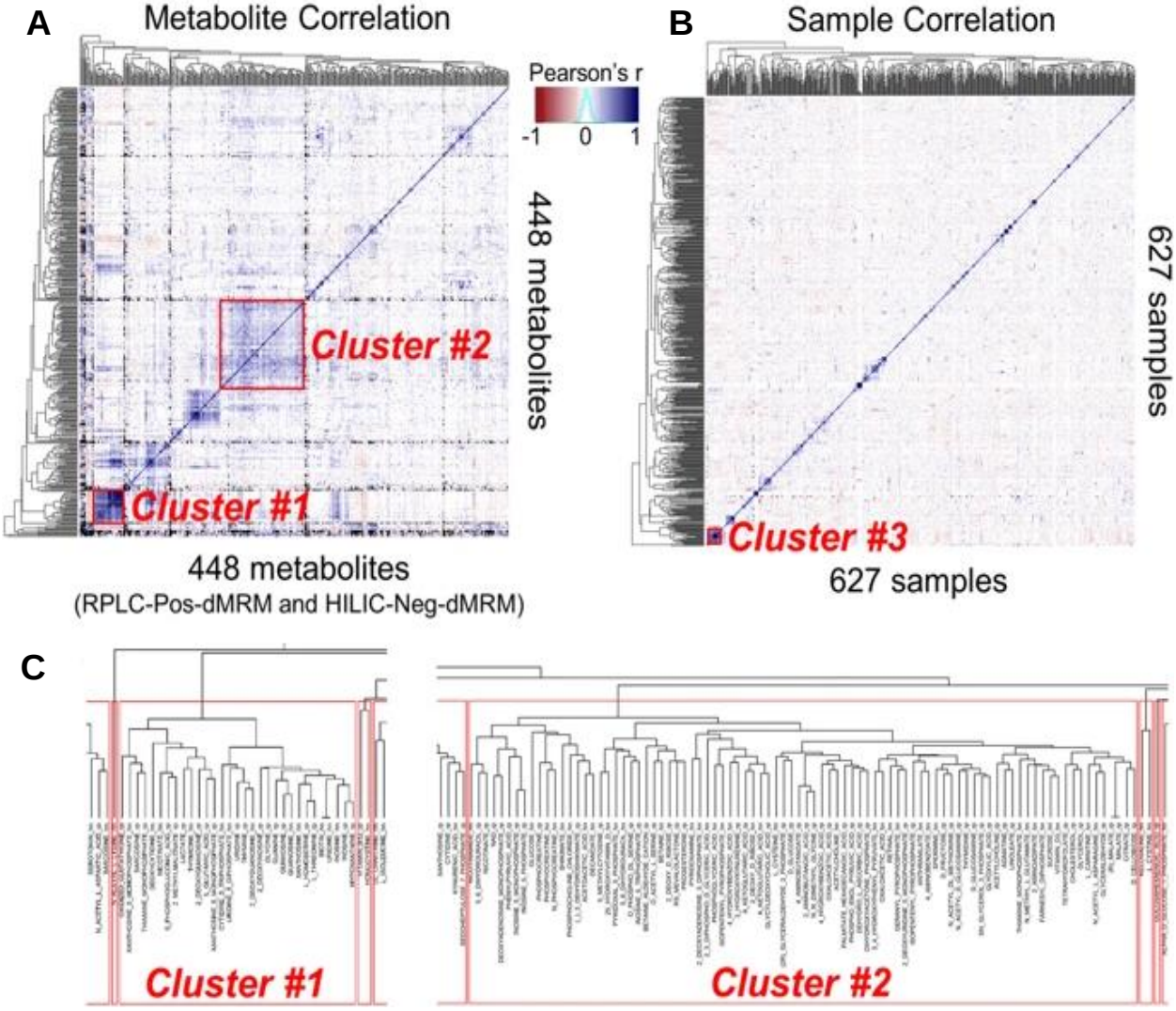

Figure 3. Global metabolite and sample profile.
A-C) Global metabolite and sample profile. **B)** Correlation heatmap of 448 metabolite measurements of relative normalized abundance from both RPLC-Pos-dMRM and HILIC-Neg-dMRM methods along with unsupervised hierarchical clustering. The color key is based on Pearson correlation coefficients. **C)** Pearson correlation heatmap of 627 samples along with unsupervised hierarchical clustering. **D)** Dendrogram trees of "Cluster #1 and #2" metabolites. Figures produced by Dr. Ho-Joon Lee.
Experiments were completed in collaboration with Peter Sajjakulnukit and Dr. Li Zhang.

frequently detected metabolites across different conditions are enriched in metabolism of amino acids, nitrogen, glutathione, and purine (MetaboAnalyst; FDR < 0.01). The remaining metabolites show a monotonic decrease in the number of measured replicate groups. It is unclear what is the generating function or mechanism of this linearly decreasing distribution.

We next calculated the average of all abundance values for each metabolite. **Figure 4b** shows a histogram of the average abundance values for all 448 metabolites and **Figure 4c** shows a distribution of the ordered average abundance values. Three of the top 20 metabolites are involved in cysteine/methionine metabolism (cystine, acetyl-serine, and glutathione) and others in glycolysis, hexosamine, amino acids, mevalonate, energy, and redox metabolism. We also find that one of the top 20 metabolites, phenylalanine, is among the most reproducible metabolites by both RPLC-Pos-dMRM and HILIC-Neg-dMRM methods, along with methionine and taurine, as discussed below. On the other hand, the bottom 20 metabolites include GDP-glucose, NADP+, fumaric acid, glycerol, dihydrofolate, leucine, docosahexaenoic acid, homocystine, TMP, sucrose, and deoxyadenosine. These metabolites are involved in many different metabolic pathways with no significant enrichment (MetaboAnalyst), suggesting that low abundance is not a pathway-specific or pathway-level feature. **Figure 4d** is a scatter plot of the average abundance and the number of replicate groups with measurements. The top five metabolites are highly abundant in 56–183 distinct groups on average, indicating the tendency of more frequent detection of more abundant metabolites. This analysis offers insight into the importance of those relatively high abundant metabolites in diverse conditions with potential effects on phenotypic differences.

Variability Analysis of RPLC-Pos-dMRM and HILIC-Neg-dMRM Data

The coefficient of variation or CV (= *SD*/*mean*) is a standard quantitative measure of statistical dispersion or variability[113]. We use CV to assess variability or consistency of replicate measurements in each replicate group for quality assessment. We calculated biological replicate-group CVs for both the RPLC-Pos-dMRM and HILIC-Neg-dMRM methods and examined their quality or reliability differences. **Figure 5a** shows a comparison of replicate-group CV distributions of the two methods. There are 28,765

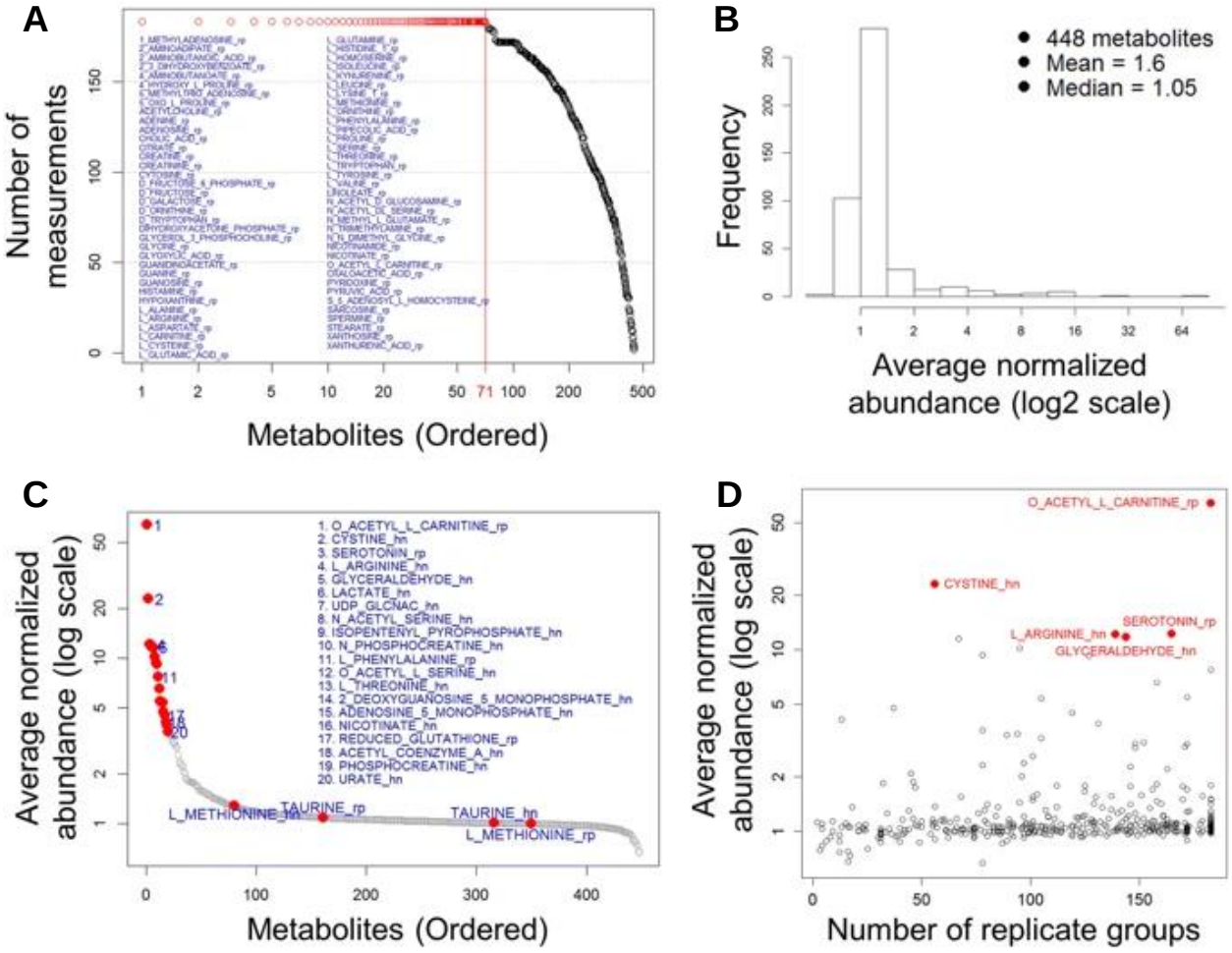

Figure 4. Relative abundance analysis.
A) Distribution of median measurements for 448 metabolites across all 183 biological replicate groups. There are 71 metabolites with measurements in the maximum 183 replicate groups as listed and as indicated in red circles. **B)** A histogram distribution of the average normalized abundance values for all 448 metabolites. **C)** Metabolite ranking of B. **D)** A scatter plot of the average normalized abundance of B or C and the numbers of replicate groups with measurements. The top 5 highly abundant metabolites are shown in red. Figures produced by Dr. Ho-Joon Lee. Experiments were completed in collaboration with Peter Sajjakulnukit and Dr. Li Zhang.

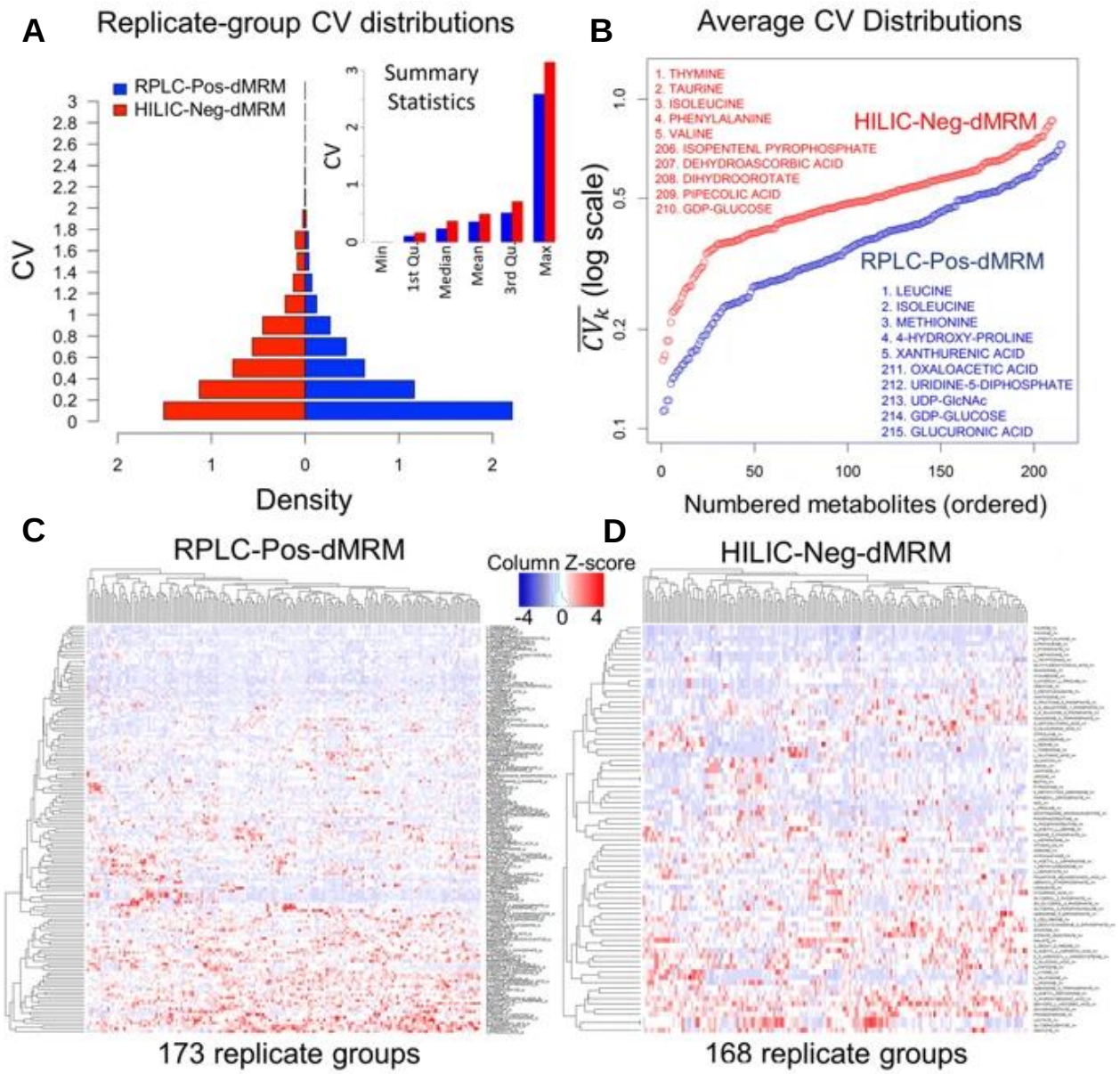

Figure 5. Analysis of CV across replicate groups.
A) Distribution of replicate-group CVs of the RPLC-Pos-dMRM and HILIC-Neg-dMRM methods. There are 28,765 CV values in RPLC-Pos-dMRM and 22,069 CV values in HILIC-Neg-dMRM from all 183 replicate groups for 220 and 228 metabolites, respectively. Summary statistics of all replicate-group CVs from the two methods are shown in the inset. **B)** Ordered distribution of $\overline{CV}k$ for individual metabolites from the RPLC-Pos-dMRM and HILIC-Neg-dMRM methods. **C)** Heatmap and hierarchical clustering of replicate-group CVs for 145 metabolites with missing values less than 30% across all replicate groups in the RPLC-Pos-dMRM method. **D)** Heatmap and hierarchical clustering of replicate-group CVs for 77 metabolites with missing values less than 30% across all replicate groups in the HILIC-Neg-dMRM method. Figures produced by Dr. Ho-Joon Lee. Experiments were completed in collaboration with Peter Sajjakulnukit and Dr. Li Zhang.

CV values in RPLC-Pos-dMRM and 22,069 CV values in HILIC-Neg-dMRM from all 183 replicate groups for 220 and 228 metabolites, respectively. RPLC-Pos-dMRM measurements show more CVs < 0.2 than HILIC-Neg-dMRM measurements by about

two-fold. The summary statistics also show overall better quality of RPLC-Pos-dMRM measurements than HILIC-Neg-dMRM.

The reliability of each metabolite measurement was assessed by the average CV in all replicate groups. **Figure 5b** shows an overview of average measurement reliability of all metabolites in each method. We then calculated the $\overline{CV}k$ where *k* is a specific metabolite normalized to the number of replicate groups with measurements. We calculated $\overline{CV}k$ only for metabolites that were measured in at least 20 replicate groups, which yielded 215 and 210 metabolites from RPLC-Pos-dMRM and HILIC-Neg-dMRM, respectively, 154 which were common. The reliability difference between the two methods is very clear, although Pearson's correlation of CVs from the two methods for the 154 common metabolites shows a significant positive relationship ($r = 0.37$; $p < 2.4e{-}6$). This suggests greater chromatographic regularity or compound stability in RPLC-Pos-dMRM than HILIC-Neg-dMRM, which is consistent with previous studies on HILIC[114,115]. It also suggests that most metabolites show a similar tendency of reliability in each method. The $\overline{CV}k$ measurements across our heterogeneous dataset could be used as a reliability index or a guidance in each method for other similar applications of LC–MS/MS targeted metabolomics. Among the 50 most reliable metabolites from each method, there are 20 overlapping metabolites including leucine/isoleucine, methionine, hydroxyproline, valine, nicotinamide, glutamate, phenylalanine, serine, glycine, and NAD, which are likely to exhibit high stability and efficient ionizations in both methods. Among the 50 least reliable metabolites from each method, there are 14 overlapping metabolites including GDP-glucose, uridine 5′-diphosphate, cytidine 5′-diphosphate, sucrose, malate, guanosine 5′-diphosphate, lactate, and glyceraldehyde, which would require more careful measurements and interpretations.

To examine the reliability in more detail, we further restricted our focus to those metabolites with measurements in at least 70% of the 183 replicate groups (i.e., CV missing values less than 30% or m ≥ 183 × 0.7 = 128m ≥ 183 × 0.7 = 128) for statistical robustness. There are 145 such metabolites for RPLC-Pos-dMRM and 77 such metabolites for HILIC-Neg-dMRM. The heat maps and hierarchical clustering in **(Figure 5c-d)** show groups of metabolites with low CVs (i.e., better reliability; rows in blue) in

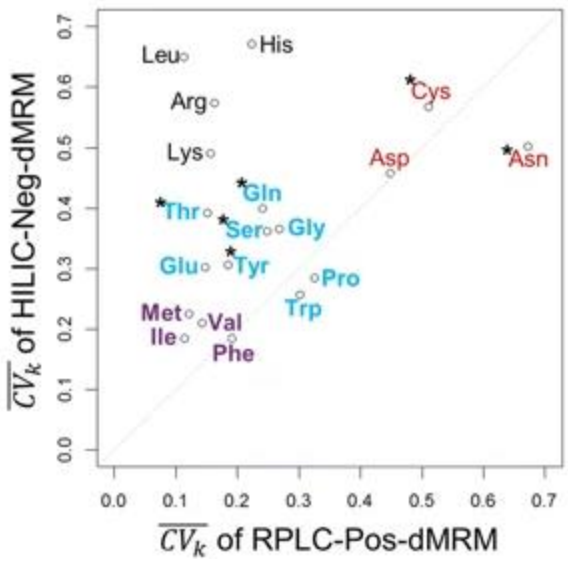

Figure 6. Scatter plot of (CV)$\overline{k}$.
19 amino acids show a reproducibility trend and patterns as color coded as a guidance for 3 groups. Figures produced by Dr. Ho-Joon Lee. Experiments were completed in collaboration with Peter Sajjakulnukit and Dr. Li Zhang.

each method. While we visually notice overall better reliability in RPLC-Pos-dMRM from the heat maps, there are metabolites with low CVs across all replicate groups in HILIC measurements such as taurine, thymine, phenylalanine, hypotaurine, pyridoxate, methionine, and tryptophan.

A pathway analysis of most reliable metabolites with $\overline{CV}k < 0.4$ (125 and 54 metabolites in RPLC-Pos-dMRM and HILIC-Neg-dMRM, respectively) shows that each method does not favor any unique pathway. Both methods tend to have reliable measurements for amino acids and nucleotides biosynthesis pathways, the main difference being the number of reliable metabolites given a threshold of $\overline{CV}k$. This pathway analysis supports the aforementioned positive correlation of $\overline{CV}k$ between the two methods. On the other hand, by focusing on 19 amino acids from both methods, we find that four amino acids show lower $\overline{CV}k$ in HILIC-Neg-dMRM than in RPLC-Pos-dMRM: phenylalanine, tryptophan, proline, and asparagine, the first three of which show similarly good measurement reproducibility as hydrophobic in both methods with $\overline{CV}k$ **(Figure 6)**. This suggests that those three amino acids may be used as most reliable reference metabolites in abundance measurements as well as in LC–MS/MS method development in both chromatographic column conditions. It is also observed that

asparagine, aspartate, and cysteine are less reliable in both methods **(Figure 6)**. We note that phenylalanine and tryptophan are often used as quality control standards in metabolomics laboratories on an empirical basis, corroborating our findings (Dr. Maureen Kachman, personal communication). We point out that all polar amino acids except asparagine show better reproducibility $\overline{CV}k$ in RPLC-Pos-dMRM than HILIC-Neg-dMRM **(Figure 6)**.

Correlation Analysis RPLC-Pos-dMRM and HILIC-Neg-dMRM Data

We continued to examine differences between RPLC-Pos-dMRM and HILIC-Neg-dMRM from a correlation point of view by focusing on those metabolites that were measured in at least 70% of all 42 experiments with both methods. We asked if abundance profiles of each metabolite from the two methods were well correlated in individual experiments as they were conducted on different days. A total of 3601 measurements were made for 237 metabolites in the 42 experiments. There were 221 metabolites that were measured in at least two experiments with both methods. 47 of them were measured in at least 70% of all 42 experiments.

For each metabolite in each experiment, we calculated the Pearson correlation coefficient between two abundance profiles measured by the two methods. **Figure 7a** shows a heat map of all RPLC-HILIC correlation coefficients, where the metabolites were sorted by the average correlation across all the experiments and the columns were sorted by the average correlation across all the metabolites. Larger circles in darker blues indicate good correlation between the two methods. The top metabolites with reliable measurements across most of the experiments include guanosine, 5-methlythio-adenosine, phosphocreatine, xanthine, proline, taurine, NAD+, and methionine, among others. On the other hand, linoleate, glucuronic acid, 4-hydroxy-L-proline, dehydro-L-ascorbic acid, and acetylcholine, among others show inconsistent measurements between the two methods, indicating that their retention mechanisms or ionization efficiency may greatly differ between the two methods from experiment to experiment on different days.

To further examine the 47 metabolites measured by the two methods, we next analyzed $\overline{CV}k$ correlations across all data sets as in the previous section. **Figure 7b** shows a distribution of $\overline{CV}k$ correlations where those metabolites on the left with

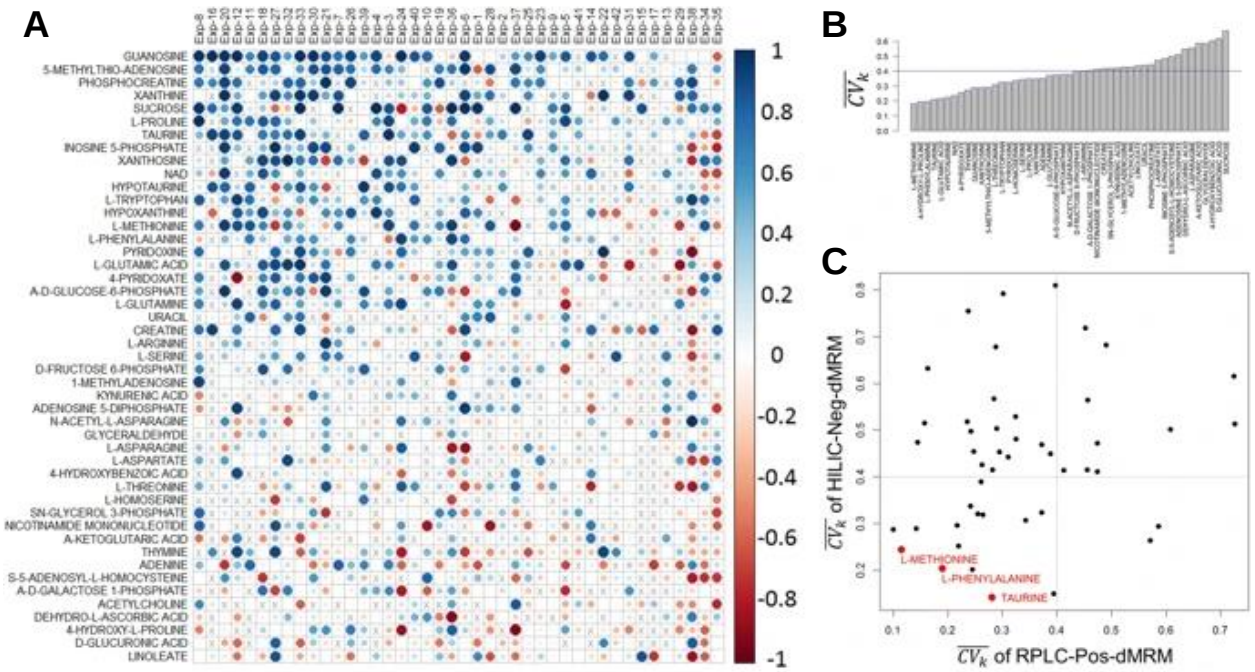

Figure 7. Correlation analysis across methods.
A-C) RPLC-HILIC correlation analysis. **A)** Heatmap of all RPLC-HILIC Pearson correlation coefficients for 47 metabolites that were measured in at least 70% of all 42 experiments. The size of the circles is proportional to absolute values of correlation coefficients. Larger circles in darker blues indicate good correlation between the RPLC-Pos-dMRM and HILIC-Neg-dMRM measurements. **B)** Distribution of $\overline{(CV)}$k across the 42 datasets in both RPLC-Pos-dMRM and HILIC-Neg-dMRM methods. **C)** A scatter plot of $\overline{(CV)}$ k from the RPLC-Pos-dMRM and HILIC-Neg-dMRM measurements for all 47 metabolites. The three most reproducible metabolites by both methods are shown in red. Figures produced by Dr. Ho-Joon Lee. Experiments were completed in collaboration with Peter Sajjakulnukit and Dr. Li Zhang.

smaller $\overline{CV}k$ are more reproducible and hence reliable across the 42 datasets by both methods on average. The top seven metabolites are methionine, 4-hydroxy-L-proline, phenylalanine, taurine, glutamic acid, hypotaurine, and NAD+ with $\overline{CV}k$ 0.3. We also calculated the average of $\overline{CV}k$ correlation in each of the two methods. The scatter plot in **(Figure 7c)** shows a distribution of $\overline{CV}k$ correlations from the two methods for all 47 metabolites. Given our reference value of $\overline{CV}k$ = 0.4, there are 15 metabolites with $\overline{CV}k$ 0.4 in both methods that we deem reproducible across diverse conditions. The three most reproducible metabolites from both methods are methionine, phenylalanine, and taurine. Phenylalanine was among the top 20 metabolites of high average abundance as discussed above. There are several metabolites which are reliable in either method alone based on a threshed of $\overline{CV}k$ =0.4. The RPLC-Pos-dMRM measurements are more reliable for 35 metabolites, whereas the HILIC-Neg-dMRM measurements are more reliable for 17 metabolites.

Analysis of Abundance Fold Changes for Effect Size and Variability

We then studied the direction and magnitude of metabolite changes following experimental perturbation. We analyzed fold changes (FC) of metabolite abundances across all case-control condition group pairs. For each pair and each metabolite, we calculated the median ($\tilde{m}$) of normalized abundance values in each group of replicates and the fold change of medians ($\tilde{F}$) of the medians, defined $\tilde{F} = \tilde{m}_{case}/\tilde{m}_{control}$. We then calculated the average of absolute values of $log_2(\tilde{F})$ for all case-control pairs for each metabolite, mean ($|log_2(\tilde{F})|$), which represents the average magnitude of the fold change in the case group for each metabolite. The magnitude or absolute value of mean ($|log_2(\tilde{F})|$) is also the effect size.

We analyzed a total of 448 metabolites in 176 case-control pairs from both RPLC-Pos-dMRM and HILIC-Neg-dMRM methods. 62.7% of the data were intact. A missing value occurs when no measurement was made in either a case or control condition. For a hierarchical clustering of the full data, we removed those metabolites and case–control pairs that have more than 50% missing values across all case–control pairs and all metabolites, respectively.

Figure 8a shows a heat map of the 294 by 161 data matrix of $log_2(\tilde{F})$ values along with hierarchical clustering dendrograms on both axes. The full 448 by 176 data matrix of fold changes gives us a histogram of all average fold-change magnitudes defined by mean ($|log_2(\tilde{F})|$) and their ordered distribution in **(Figure 8c**). The average fold-change magnitudes for most metabolites are less than 2 (the peak of the histogram) and the top 20 metabolites with the highest average effect sizes are mostly involved in glycolysis, redox, pyrimidine, and methionine/cysteine/folate metabolism. Homocystine shows the largest average FC magnitude of more than 20, and lactate/glyceraldehyde the second largest of more than 9. We note that lactate and glyceraldehyde were not distinguishable in our HILIC-Neg-dMRM method with identical data. Most of the top 20 metabolites were measured in more than 70 case–control pairs, except homocystine in nine pairs in the HILIC method and NADP in 12 pairs in the HILIC method **(Figure 8c)**. In addition, we calculated the standard deviation (SD) of the effect sizes for each metabolite to examine the effect-size variability in all case-control pairs for that metabolite.

Figure 8d shows a histogram of the SDs and an ordered SD distribution. The SDs for most metabolites are less than 1 and there are seven metabolites with SD > 3 including lactate/glyceraldehyde and orotate. We also performed an analysis of median absolute deviation (MAD) to complement the SD analysis. **Figure 8e** shows a MAD histogram and an ordered MAD distribution. The top 20 most variable metabolites with

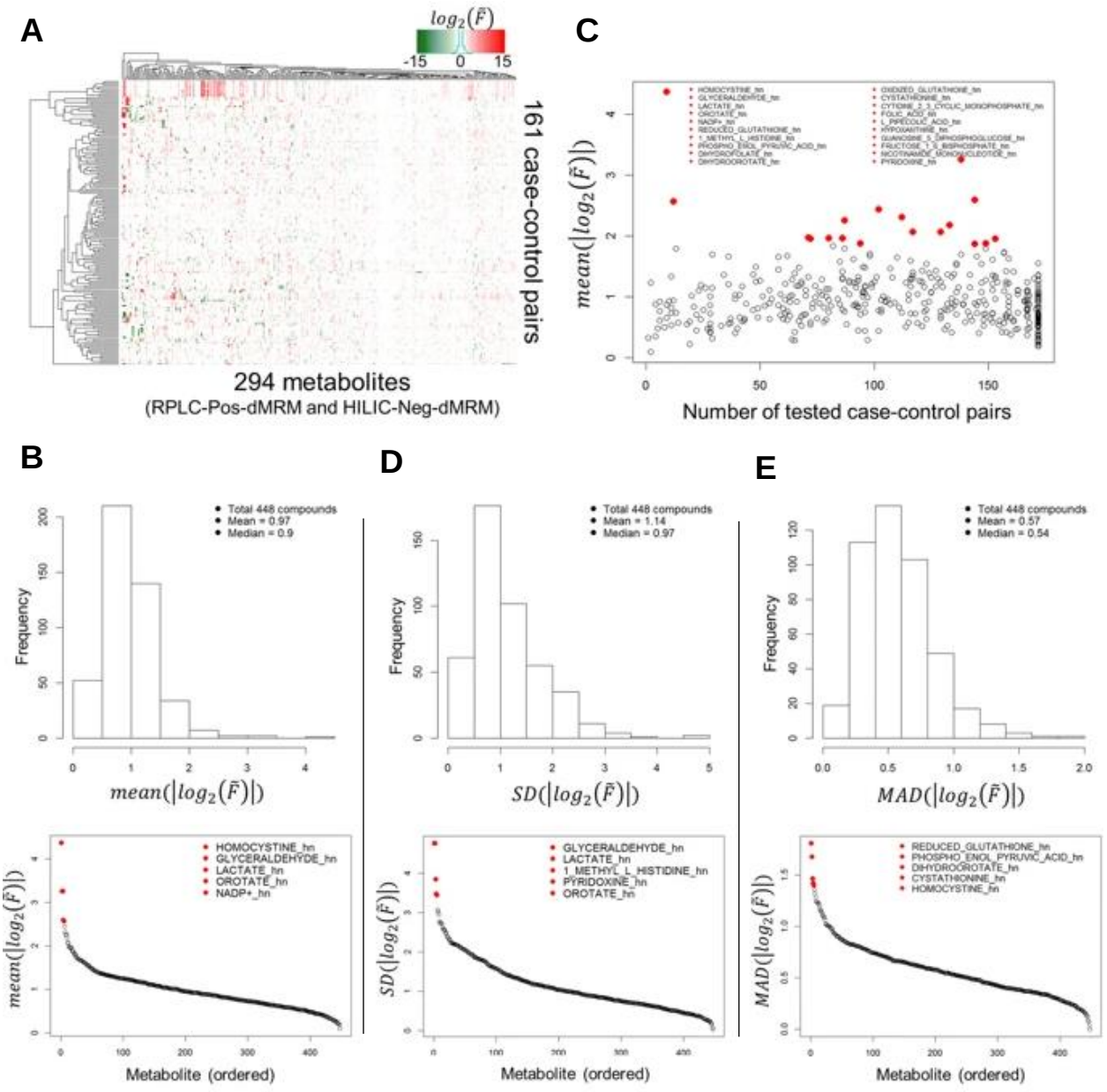

Figure 8. Metabolite abundance analysis.
A) Heatmap of $\log_2(\tilde{F})$ for all 294 metabolites and 161 case-control sample pairs. **B)** Histogram of all average effect sizes and an ordered distribution of all average magnitudes. **C)** Scatter plot of the average fold change magitudes and the numbers of tested case-control pairs. **D)** Standard deviation of the effect size. **E)** Median absolute deviation (MAD) of effect sizes. Figures produced by Dr. Ho-Joon Lee. Experiments were completed in collaboration with Peter Sajjakulnukit and Dr. Li Zhang.

the highest MADs are involved in glycolysis, redox, pyrimidine, energy, and methionine/cysteine/folate metabolism. **Figure 9a-b** show good positive correlations between the average effect sizes and the SD and MAD variability, respectively. Homocystine, lactate/glyceraldehyde, orotate, GSH, and dihydrofolate have both the highest average effect size and the largest variability by both SD and MAD among the top 20, which suggests that they are most dynamic and responsive metabolites across this diverse array of conditions.

We note that we have not performed analysis of batch effects in this study because it is challenging to analyze and model batch effects in all 42 datasets in a reasonable way. Any attempt to correct batch effects globally may introduce mathematical artifacts into certain data points locally, making biological interpretations more complex or unreasonable across all datasets. We consider the analysis of batch effects an independent topic for a future study. Therefore, our analysis and results should be interpreted within the constraints of this limitation.

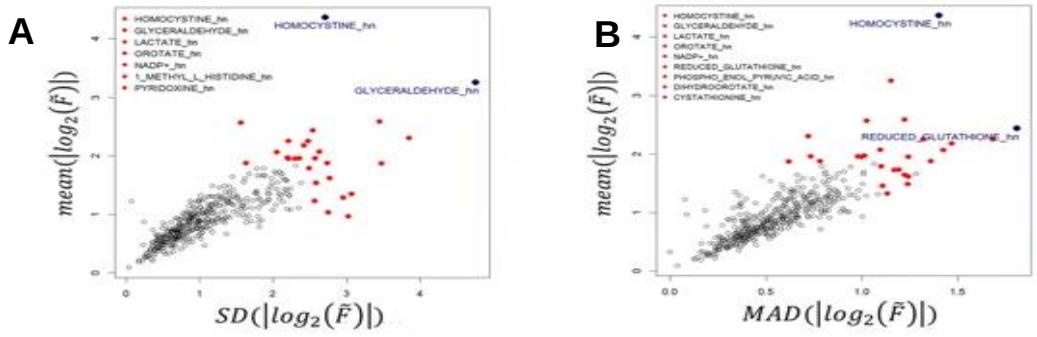

Figure 9. Scatter plot of variability metrics.
A-B) Scatter plots of variability metrics. **A)** Average effect size versus the SD per metabolite. **B)** Average effect size versus MAD. Figures produced by Dr. Ho-Joon Lee. Experiments were completed in collaboration with Peter Sajjakulnukit and Dr. Li Zhang.

2.4 Discussion

Here we performed LC-MS/MS targeted metabolomics to generate 42 data sets in a wide range of experimental perturbations and divers sample types using the same platform. We conducted a meta-analysis to systematically assess data quality of both methods in biological replicate groups to quantify the reliability of measurements for both RPLC-Pos-dMRM and HILIC-Neg-dMRM methods. We find that the RPLC-Pos-dMRM method tends to generate more reproducible measurements compared with the

HILIC-Neg-dMRM method. Several metabolites are reliably measured in both methods, including methionine, phenylalanine, and taurine. Phenylalanine is among the most abundant metabolites profiled across our heterogeneous sample set along with acetylcarnitine, cystine, arginine, lactate/glyceraldehyde, UDP-GlcNAc, AMP, GSH, and acetyl-CoA.

Comparing the changes in metabolite abundance and variability in case-control groups revealed dynamic and variable metabolites across heterogeneous conditions. These highly dynamic metabolites include homocystine, lactate/glyceraldehyde, and GSH and metabolite involved in cysteine metabolism (taurine, cystine, homocystine), and glycolysis (glyceraldehyde, lactate), hexosamine biosynthesis (UDP-GlcNAc), redox balance (GSH), fatty acid metabolism (acetylcarnitine, acetyl-CoA). The dynamic nature of these metabolites may reflect regulatory or signaling roles outside of intermediary metabolism. For example, the abundances of lactate, taurine, methionine, and acetylcarnitine frequently differ in tumors compared with normal tissues[39,50,111,112,116]. Overall, our study provides a systematic approach for targeted metabolomics analysis for RPLC-Pos-dMRM or HILIC-Neg-dMRM methods and provides a reference for accessing the reliability of metabolite measures using LC-MS/MS targeted metabolomics.

2.5 Materials and Methods

Sample Preparation

Samples were prepared and published previously[13–16,21]. Each experimental condition possesses a minimum of three biological replicate samples prepared from distinct cell culture plates, preparations, or animals.

Primary and Cultured cells

Biological replicates with $n \geq 3$ were seeded at equivalent density and harvested in log phase by media aspiration. Aqueous metabolites of adherent primary or cultured cells on 6-well or 10 cm^2 plates were extracted by adding 1 mL or 4 mL of 80% cold (− 80 °C) methanol, respectively, followed by incubation at − 80 °C for 10 min. Cells were scrapped and all material were collected and subjected to centrifugation at 14,000 rpm at 4 °C for 10 min to pellet the insoluble material. Suspension cells were gently

centrifuged to pellet and media was completely aspirated. The procedure is done on a bucket of dry ice and as quickly as possible in order to stop metabolism immediately. Samples were normalized by the volume corresponding to protein concentration measured from parallel prepared lysates (typically, 1–2 million cells at 70–80% confluence). Then, samples were dried under vacuum and suspended in a 1:1 H_2O/methanol solution for LC–MS analysis.

Tissues, organs, and tumors

Samples of 50–200 mg ($n \geq 3$) were placed in a tube containing 1 mL of 80% cold (− 80 °C) methanol and then homogenized using steel beads and a Qiagen Tissue Lyser by multiple rounds of 45-second shaking at room temperature before centrifugation at 14,000 rpm at 4 °C for 10 min. Samples were normalized by taking the volume corresponding to 10 mg of the tumor weight and further processed as above for LC–MS analysis.

Cultured media and sera

Metabolites from equivalent volumes of media or sera ($n \geq 3$; typically, ~ 200 µL) were extracted by adding 100% cold (− 80 °C) methanol with a 1:4 ratio of the sample to methanol (i.e., 80% methanol final) and further processed as above for LC–MS analysis.

LC–MS/MS metabolomics analysis

Our LC–MS/MS metabolomics analysis was performed as described previously[13–15]. In brief, an Agilent 1290 UHPLC and 6490 Triple Quadrupole (QqQ) mass spectrometer (LC–MS/MS) were used for label-free targeted metabolomics analysis. Agilent MassHunter Optimizer and Workstation Software LC–MS Data Acquisition for 6400 Series Triple Quadrupole B.08.00 was used for standard optimization and data acquisition. Agilent MassHunter Workstation Software Quantitative Analysis Version B.0700 for QqQ was used for initial raw data extraction and analysis. Each MRM transition and its retention time of left delta and right delta of 1 min. Additional parameters include mass extraction window of 0.05 Da right and left from the extract m/z, Agile2 integrator algorithm, peak filter of 100 counts, noise algorithm RMS, noise SD multiplier of 5 min, S/N 3, Accuracy Max 20% max %Dev, and Quadratic/Cubic

Savitzky-Golay smoothing algorithm with smoothing function width of 14 and Gaussian width of 5. For RPLC, a Waters Acquity UPLC BEH TSS C18 column (2.1 × 100 mm, 1.7 µm) was used in the positive ionization mode with mobile phase (A) consisting of 0.5 mM NH_4F and 0.1% formic acid in water; mobile phase (B) consisting of 0.1% formic acid in acetonitrile. Gradient program: mobile phase (B) was held at 1% for 1.5 min, increased to 80% at 15 min, then to 99% at 17 min and held for 2 min before going to initial condition and held for 10 min. For HILIC, a Waters Acquity UPLC BEH amide column (2.1 × 100 mm, 1.7 µm) was used in the negative ionization mode with mobile phase (A) consisting of 20 mM ammonium acetate (NH_4OAc) in water at pH 9.6; mobile phase (B) consisting of acetonitrile (ACN). Gradient program: mobile phase (B) was held at 85% for 1 min, decreased to 65% at 12 min, then to 40% at 15 min and held for 5 min before going to the initial condition and held for 10 min. Both columns were at 40℃ and 3 µL of each sample was injected into the LC–MS with a flow rate of 0.2 mL/min. Calibration was achieved through Agilent ESI-Low Concentration Tuning Mix. Optimization was performed on the 6490 QqQ in the RPLC-positive or HILIC-negative mode for each of 245 standard compounds (215 and 217 compounds for RPLC-positive and HILIC-negative, respectively) to obtain the best fragment ion and MS parameters such as fragmentation energy for each standard. Retention time (RT) for each standard was measured from a pure standard solution or a mixture standard solution. The LC–MS/MS methods were created with dynamic MRM (dMRM) with RTs, RT windows, and transitions of all 245 standard compounds. Key parameters of electrospray ionization (ESI) in both the positive and the negative acquisition modes are: Gas temp 275℃, Gas Flow 14 l/min, Nebulizer at 20 psi, Sheath Gas Heater 250℃, Sheath Gas Flow 11 L/min, and Capillary 3000 V. For MS: Delta EMV 200 V or 350 V for the positive or negative acquisition mode respectively and Cycle Time 500 ms and Cell Acc 4 V for both modes. In this study we denote the dMRM method with RPLC in the positive ionization mode by RPLC-Pos-dMRM and the dMRM method with HILIC in the negative ionization mode by HILIC-Neg-dMRM. We note that our methods do not distinguish stereoisomers, hence care should be taken in interpretation of such data.

Computational data processing, quality control, and statistical analysis

Pre-processed data with Agilent Mass Hunter Workstation Software Quantitative Analysis were post-processed for further quality control in the programming language R. Let A_{ij} be a data matrix of raw abundance with M metabolites and N samples, i.e., $i = 1$ to M and $j = 1$ to N. First, we examined the distribution of sums of all metabolite abundance peak areas across individual samples, $\{S_j = \sum_{i=1}^{M} A_{ij} : j = 1 \; to \; N\}$, in a given experiment as a measure for equal sample loading into the instrument. Any outlier sample was removed, which is defined by a loading difference of greater than 70% compared to the average of the total abundance sums. The choice of 70% is based on our experience, rather than an optimization technique, and this has consistently yielded interpretable data and biologically relevant results in all experiments on our platform[13–16]. Next, we calculated coefficients of variation (CVs) in all biological replicate groups ($n \geq 3$) for each metabolite given a cut-off value of peak areas in each of the RPLC-Pos-dMRM and the HILIC-Neg-dMRM methods. We then compared distributions of CVs for the whole dataset for a set of peak area cut-off values of 0, 1000, 5000, 10000, 15000, 20000, 25000 and 30000 in each method. A noise cut-off value of peak areas in each method was chosen by manual inspection of the CV distributions. The noise-filtered data of individual samples were then normalized by the total intensity of all metabolites. We retained only those metabolites with at least two replicate measurements for a given experimental variable. The remaining missing value in each condition for each metabolite was filled with the median value of the other replicate measurements. Let $A'_{ij}(\frac{1}{N'}\sum_{k=1}^{N'} A'_{ik})$ ("normalized relative abundance" hereafter), for comparisons, statistical analyses, and visualizations among metabolites. This normalization and scaling method has been used in our previous studies with biologically meaningful results[14–16]. A comparison analysis with other alternative methods[22–25] is beyond the scope of this study. Finally, we visually inspected a correlation heat map profile of the samples of the resultant data to identify and remove any further outlier samples based on hierarchical clustering and abnormal heat map patterns. Heat maps were generated with the function, *heatmap.2*, from the Bioconductor package, *gplots*, and hierarchical clustering was performed with default parameters in *heatmap.2*. Pathway analysis was done using the web tool, MetaboAnalyst[26].

2.6 Chapter 2 References

1. Johnson, C. H., Ivanisevic, J. & Siuzdak, G. Metabolomics: beyond biomarkers and towards mechanisms. *Nature Reviews Molecular Cell Biology* **17**, 451–459 (2016).

2. Patti, G. J., Yanes, O. & Siuzdak, G. Metabolomics: the apogee of the omics trilogy. *Nature Reviews Molecular Cell Biology* **13**, 263–269 (2012).

3. Wishart, D. S. Emerging applications of metabolomics in drug discovery and precision medicine. *Nature Reviews Drug Discovery* **15**, 473–484 (2016).

4. Zhou, J. & Yin, Y. Strategies for large-scale targeted metabolomics quantification by liquid chromatography-mass spectrometry. *Analyst* **141**, 6362–6373 (2016).

5. Griffiths, W. J. *et al.* Targeted Metabolomics for Biomarker Discovery. *Angewandte Chemie International Edition* **49**, 5426–5445 (2010).

6. Buszewski, B. & Noga, S. Hydrophilic interaction liquid chromatography (HILIC)—a powerful separation technique. *Anal Bioanal Chem* **402**, 231–247 (2012).

7. Cubbon, S., Antonio, C., Wilson, J. & Thomas-Oates, J. Metabolomic applications of HILIC–LC–MS. *Mass Spectrometry Reviews* **29**, 671–684 (2010).

8. Ivanisevic, J. *et al.* Toward 'Omic Scale Metabolite Profiling: A Dual Separation–Mass Spectrometry Approach for Coverage of Lipid and Central Carbon Metabolism. *Anal. Chem.* **85**, 6876–6884 (2013).

9. Lu, W., Bennett, B. D. & Rabinowitz, J. D. Analytical strategies for LC–MS-based targeted metabolomics. *Journal of Chromatography B* **871**, 236–242 (2008).

10. Rojo, D., Barbas, C. & Rupérez, F. J. LC–MS metabolomics of polar compounds. *Bioanalysis* **4**, 1235–1243 (2012).

11. Tang, D.-Q., Zou, L., Yin, X.-X. & Ong, C. N. HILIC-MS for metabolomics: An attractive and complementary approach to RPLC-MS. *Mass Spectrometry Reviews* **35**, 574–600 (2016).

12. Xie, B. *et al.* Isotope Labeling-Assisted Evaluation of Hydrophilic and Hydrophobic Liquid Chromatograph–Mass Spectrometry for Metabolomics Profiling. *Anal. Chem.* **90**, 8538–8545 (2018).

13. Sousa, C. M. *et al.* Pancreatic stellate cells support tumour metabolism through autophagic alanine secretion. *Nature* **536**, 479–483 (2016).

14. Schofield, H. K. *et al.* Mutant p53^{R270H} drives altered metabolism and increased invasion in pancreatic ductal adenocarcinoma. *JCI Insight* **3**, (2018).

15. Halbrook, C. J. *et al.* Macrophage-Released Pyrimidines Inhibit Gemcitabine Therapy in Pancreatic Cancer. *Cell Metab.* **29**, 1390-1399.e6 (2019).

16. Svoboda, L. K. *et al.* Menin regulates the serine biosynthetic pathway in Ewing sarcoma. *The Journal of Pathology* **245**, 324–336 (2018).

17. Carobene, A., Braga, F., Roraas, T., Sandberg, S. & Bartlett, W. A. A systematic review of data on biological variation for alanine aminotransferase, aspartate aminotransferase and γ-glutamyl transferase. *Clinical Chemistry and Laboratory Medicine (CCLM)* **51**, 1997–2007 (2013).

18. Hao, Z., Xiao, B. & Weng, N. Impact of column temperature and mobile phase components on selectivity of hydrophilic interaction chromatography (HILIC). *Journal of Separation Science* **31**, 1449–1464 (2008).

19. Rhoades, S. D. & Weljie, A. M. Comprehensive optimization of LC–MS metabolomics methods using design of experiments (COLMeD). *Metabolomics* **12**, 183 (2016).

20. Reznik, E. *et al.* A Landscape of Metabolic Variation across Tumor Types. *Cell Systems* **6**, 301-313.e3 (2018).

21. Yuan, M., Breitkopf, S. B., Yang, X. & Asara, J. M. A positive/negative ion–switching, targeted mass spectrometry–based metabolomics platform for bodily fluids, cells, and fresh and fixed tissue. *Nature Protocols* **7**, 872–881 (2012).

22. Kirpich, A. S. *et al.* SECIMTools: a suite of metabolomics data analysis tools. *BMC Bioinformatics* **19**, 1–11 (2018).

23. Berg, R. A. van den, Hoefsloot, H. C., Westerhuis, J. A., Smilde, A. K. & Werf, M. J. van der. Centering, scaling, and transformations: improving the biological information content of metabolomics data. *BMC Genomics* **7**, 1–15 (2006).

24. Wanichthanarak, K., Fan, S., Grapov, D., Barupal, D. K. & Fiehn, O. Metabox: A Toolbox for Metabolomic Data Analysis, Interpretation and Integrative Exploration. *PLOS ONE* **12**, e0171046 (2017).

25. Li, B. *et al.* NOREVA: normalization and evaluation of MS-based metabolomics data. *Nucleic Acids Res* **45**, W162–W170 (2017).

26. Chong, J. *et al.* MetaboAnalyst 4.0: towards more transparent and integrative metabolomics analysis. *Nucleic Acids Res* **46**, W486–W494 (2018).

Chapter 3. Cysteine Depletion Induces Pancreatic Tumor Ferroptosis in Mice[2]

3.1 Abstract

Ferroptosis is a form of cell death that results from the catastrophic accumulation of lipid reactive oxygen species (ROS). Oncogenic signaling elevates lipid ROS production in many tumor types and is counteracted by metabolites that are derived from the amino acid cysteine. In this work, we show that the import of oxidized cysteine (cystine) via system x_C^- is a critical dependency of pancreatic ductal adenocarcinoma (PDA), which is a leading cause of cancer mortality. PDA cells used cysteine to synthesize glutathione and coenzyme A, which, together, down-regulated ferroptosis. Studying genetically engineered mice, we found that the deletion of a system x_C^- subunit, *Slc7a11*, induced tumor-selective ferroptosis and inhibited PDA growth. This was replicated through the administration of cyst(e)inase, a drug that depletes cysteine and cystine, demonstrating a translatable means to induce ferroptosis in PDA.

3.2 Introduction

Pancreatic ductal adenocarcinoma (PDA) is a deadly cancer that is resistant to traditional therapies. More than 90% of PDAC cases harbor mutations in KRAS that both promote proliferation and alter cellular metabolism. A by-product of mutant-KRAS signaling is the increased production of reactive oxygen species (ROS), which can damage cellular components. To compensate, PDAC cells up-regulate metabolic programs that detoxify ROS using cysteine-derived metabolites such as glutathione (GSH)[1]. Most cellular cysteine is acquired through the system x_C^- antiporter, which

[2] The Contents of this chapter were adapted and reproduced from a published co-first authored article: Badgley, M. A., **Kremer, D. M.***, Maurer, H.C.* *et al.* Cysteine depletion induces pancreatic tumor ferroptosis in mice. *Science* **368**, 85–89 (2020).

exchanges extracellular, oxidized cysteine (cystine) for intracellular glutamate. Yet, germline deletion of the system x_C^- gene, *SLC7A11*, is well tolerated in unstressed mice[2], which suggests that normal cells have low basal cystine import requirements. We hypothesized that cystine import is a critical dependency of PDA that may be selectively targeted as an anticancer therapy.

3.3 Results

Exogenous Cystine Starvation Induces Ferroptosis in Pancreatic Cancer Cells

To investigate the role of cysteine metabolism in PDAC, we measured the viability of human PDAC cell lines cultured for 24 hours in media with varying concentrations of cystine or the system x_C^- inhibitor imidazole ketone erastin (IKE) **(Figures 10a-b)**[3]. In four of five PDAC lines, cystine starvation reduced cell viability by >80%; this was largely prevented by addition of the lipophilic antioxidant Trolox. Cystine-starved cells underwent catastrophic destabilization of their plasma membranes, without visual evidence of nuclear fragmentation **(online movie)**. IKE treatment mimicked the effects of cystine withdrawal, quickly killing most cells from the four sensitive PDAC lines in a manner that was visually identical to that of cystine starvation but distinct from staurosporine-induced apoptosis **(Figure 11a and online movies 2 and 3)**. Neither cystine starvation nor system x_c^- inhibition (collectively referred to as cysteine depletion) induced caspase 3 cleavage **(Figure 11b)**, which indicates that the cell death was not apoptotic. Rather, the oxidative cell death resembled ferroptosis, a form of iron-dependent, non-apoptotic cell death previously associated with system x_C^- inhibition[4].

We found that co-treatment of human PDAC cells with either deferoxamine (DFO, an iron chelator), ferrostatin-1 (Fer1, a ferroptosis inhibitor), or N-acetylcysteine (NAC, a cell-permeable analog of cysteine) markedly reduced cell death from cysteine depletion, whereas inhibitors of apoptosis or necroptosis had little impact on cell death, consistent with previous reports **(Figures 10c)**[5]**.** Autophagy inhibition had variable effects in different lines, likely reflecting the known effect of ferritinophagy on ferroptosis[6]**.** Using the fluorescent probe C11-BODIPY, we observed a large increase in

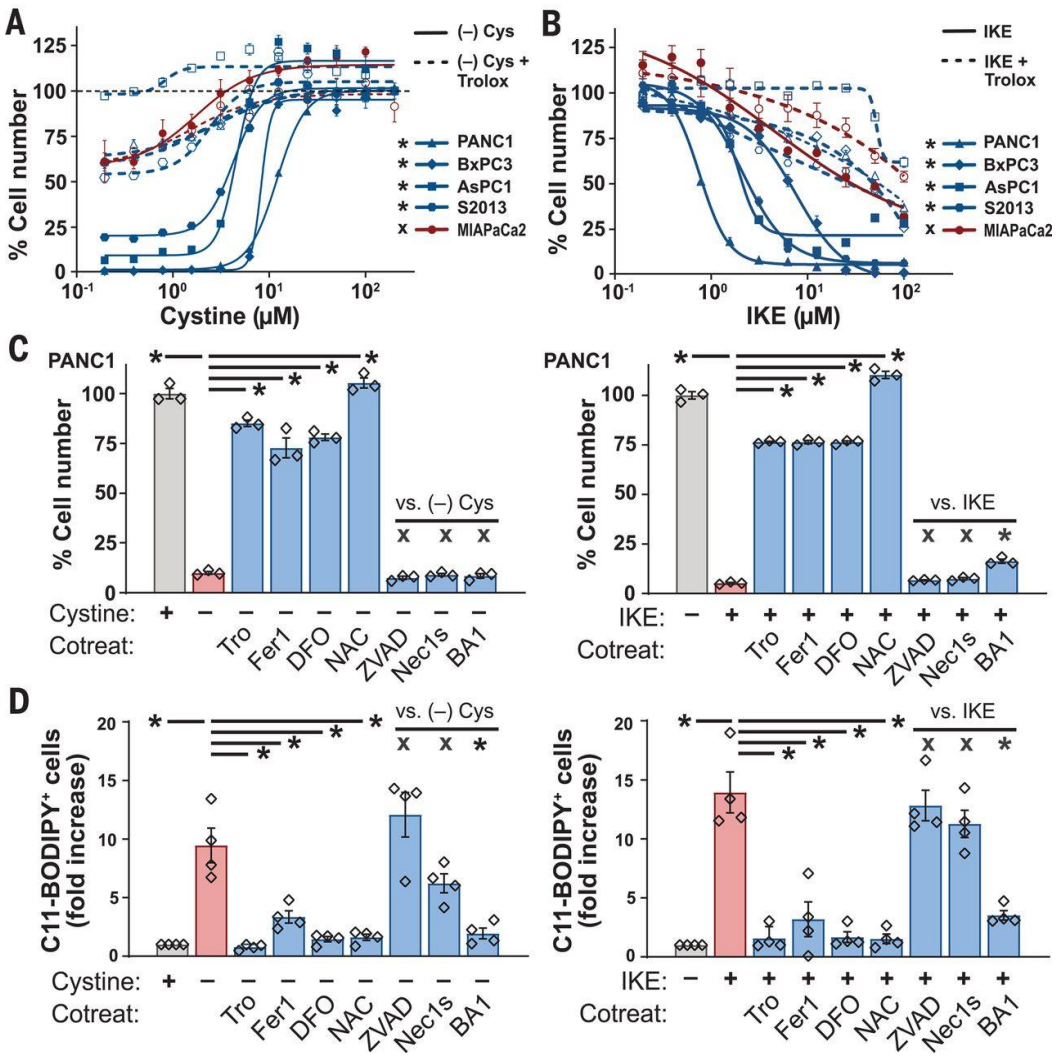

Figure 10. Pancreatic cancer cells require exogenous cystine to avert ferroptosis.
(A-B) Viability of human PDAC lines after 24 hours culture in varying concentrations of cystine **(A)** or IKE **(B)**, alone or in combination with 100 μM Trolox. Student's t test was performed, comparing maximal cytotoxicity ± Trolox. **(C)** Viability of PANC-1 cells cultured for 24 hours in cystine-free media (left) or treated with 10 μM IKE (right), alone or in combination with 100 μM Trolox (Tro), 500 nM ferrostatin-1 (Fer1), 100 μM deferoxamine (DFO), 1mM N-acetyl cysteine (NAC), 50 μM ZVAD-FMK, 1 nM Bafilomycin A1 (BA1), or 10 μM Necrostatin-1s (Nec1s). Tukey test was performed. **(D)** Flow cytometry of C11-BODIPY fluorescence in PANC-1, AsPC-1, BxPC-3, and S-2013 cells after 6 to 8 hours of treatment with conditions from **(C)**. Tukey test was performed. All data are means ± SEM of three independent experiments. *P < 0.05; x, no significant difference. Experiments were conducted in collaboration with Dr. Michael A. Badgley et al. Figures were produced by Drs. Michael A. Badgley and Ken Olive.

lipid oxidation (a hallmark of ferroptosis) prior to cell death in response to cysteine depletion; this was prevented by cotreatment with Trolox, Fer-1, NAC, and DFO **(Figures 10d and 12a-b)**. By contrast, elevated total ROS levels induced by cysteine depletion were not prevented by these agents, which argues against a more general oxidative process **(Figure 12c)**. We conclude from these experiments that most PDAC

lines rely on cysteine to prevent ferroptotic cell death. An analysis of *SLC7A11* expression across human datasets revealed a modest overexpression in PDAC versus normal tissues, enrichment in the malignant epithelial compartment of PDAC, and an association with signatures of redox stress **(Figure 13)**. Across multiple human cancers, *SLC7A11* was frequently overexpressed and associated with reduced survival **(Figure 14)**.

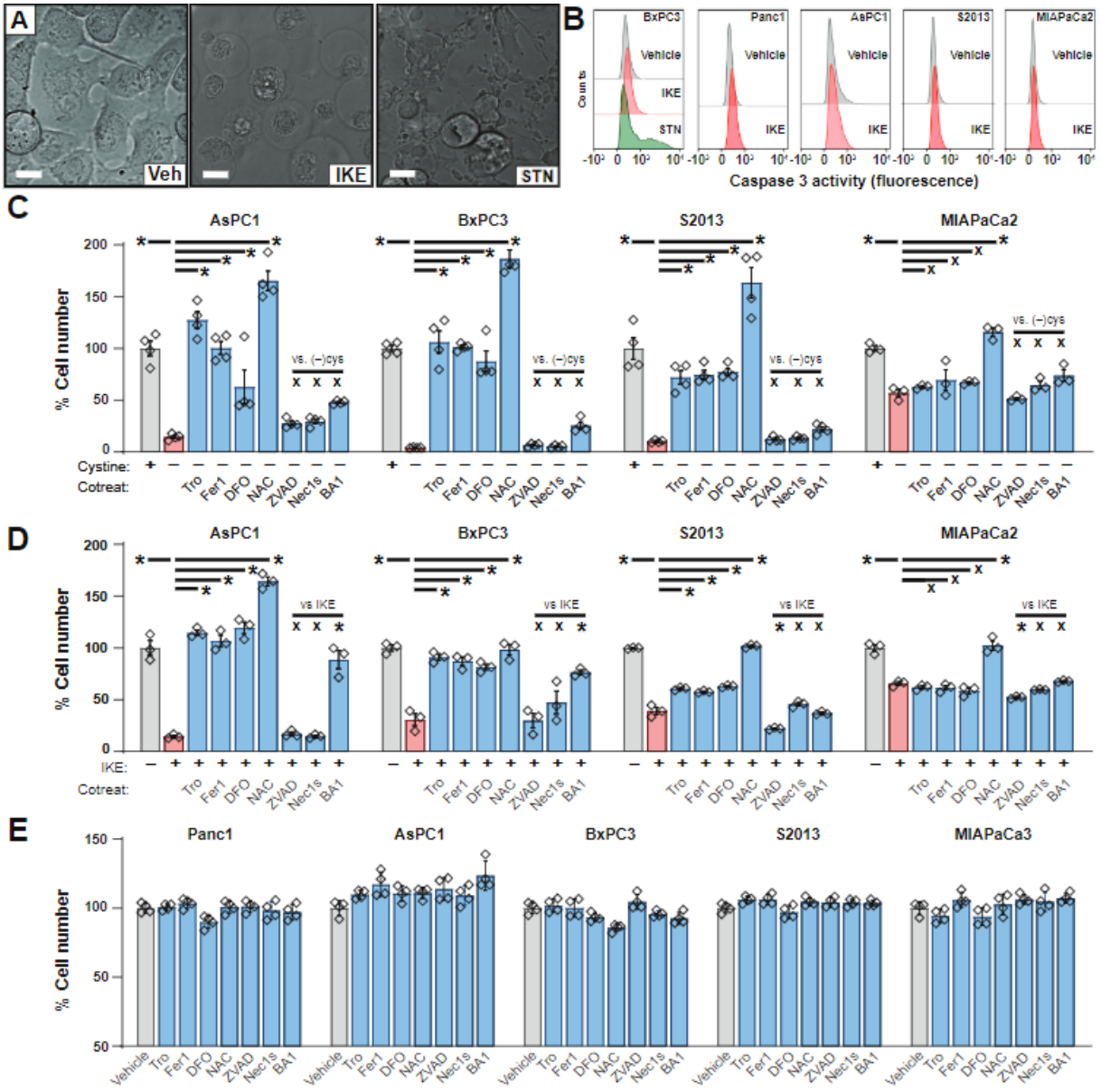

Figure 11. Cystine deprevation or IKE induce ferroptosis in PDA cell lines.
(A) High magnification image of PANC-1 cells cultured in the presence ofvehicle (0.1% DMSO), 5 μM IKE or 0.2 μM staurosporine (STN), a known inducer of apoptosis, after 16 hours. Bar = 15 μm. **(B)** Flowcytometric analysis of cleaved caspase 3 activation in cell lines stained with a FITC-based active caspase 3 antibody. Cells were treated with vehicle (0.1% DMSO, gray) and IKE (5 μM, red). In BxPC-3 cells, staurosoporine (STN) treatment is used as a positive control (0.2 μM, green). **(C)** Cell viability of a panel of human pancreatic cancer cells cultured in vehicle (0.1% DMSO and 1mM HCl veh, shown in gray), the absence of cystine (no cys, shown in red), and in the absence of cystine but in the presence of100 μM Trolox (Tro, shown in blue), 500 nM ferrostatin-1 (Fer-1, ferroptosis inhibitor),100 μM deferoxamine (DFO, iron chelator),1 mM NAC (NAC), 50 μM ZVAD-FMK (ZVAD, apoptosis inhibitor), 1 nM bafilomycin A1 (BA1, autophagy inhibitor), and 10μM Necrostatin 1s (Nec1s,necroptosis inhibitor). Viability was assessed after 24 hours of treatment. Error equals +/- SEM. n = 3 biological replicates. * = $p < 0.05$with Tukey's test. x = no statistically significant difference(D)Cell viability of a panel of human pancreatic cancer cells cultured in vehicle (0.2% DMSO, veh), 5 μM IKE, and the aforementioned compounds and the concentrations indicated in Fig. S1C. Viability was accessed at 24 hours after treatment. Error equals+/- SEM. n = 3 biological replicates. * = $p < 0.05$ with Tukey's test. x = no statistically significant difference. **(E)** Single treatment controls for all experiments figure 10 c-d and 11 c-d. Experiments were conducted in collaboration with Dr. Michael A. Badgley et al. Figures were produced by Drs. Michael A. Badgley and Ken Olive.

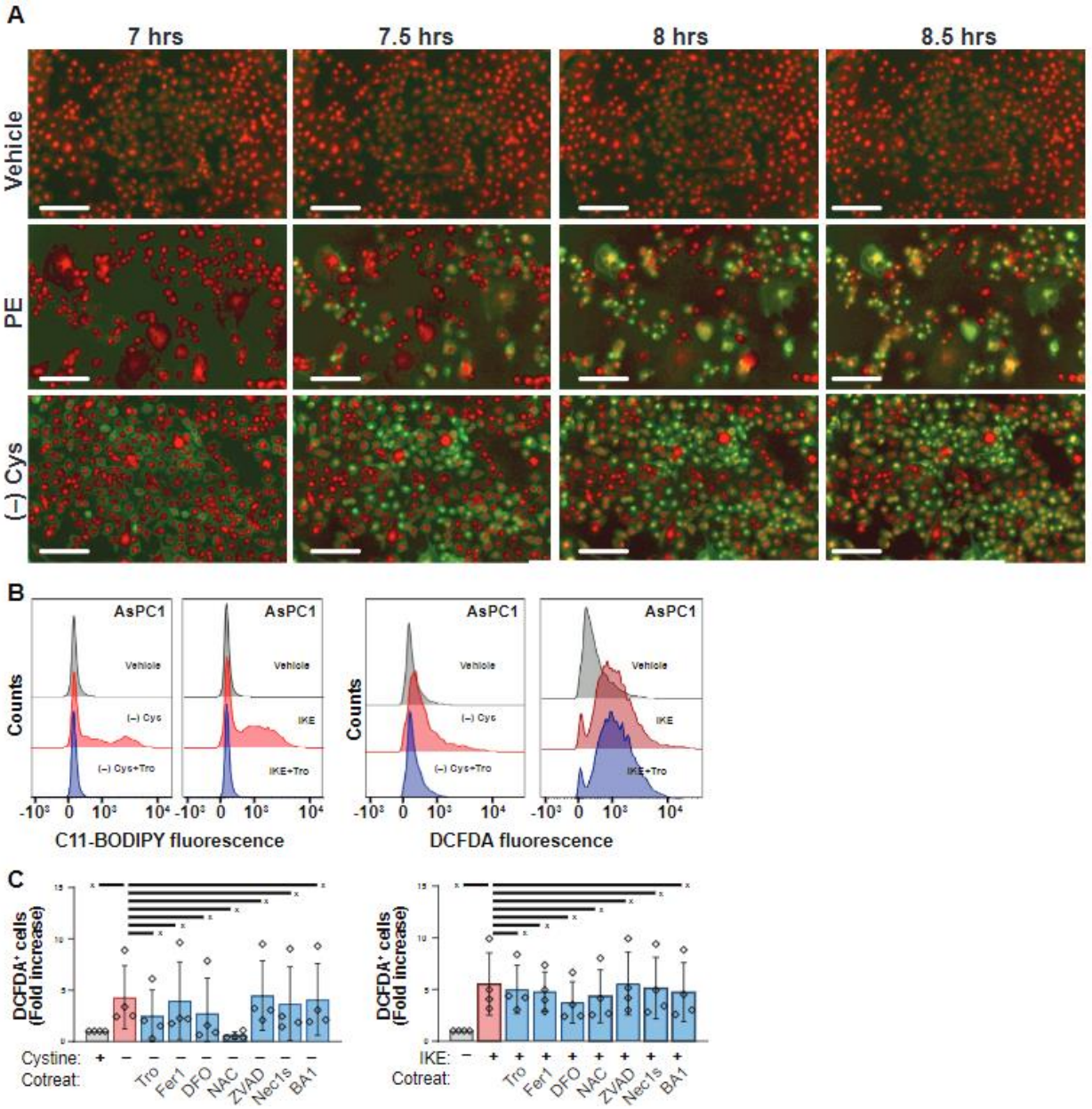

Figure 12. Lipid oxidation in PDA cell lines following cysteine depletion.
(A) Time-lapse fluorescent images of PANC-1 cells cultured in indicated conditions for indicated times. - cys indicates no cystine present in extracellular media. PE was present at 1 μM. Here, vehicle is 0.01% DMSO. Cells are stained with C-11 BODIPY, a lipid ROS indicator. Green staining highlights oxidized lipids and red staining shows reduced lipids. White bars indicate scale of 300 μm. **(B)** Flow cytometric analysis of AsPC-1 cells stained with C11-BODIPY, a marker of lipid oxidation; or H2-DCFDA, a marker of general oxidative stress, after 6-8 hours of treatment with vehicle or no cystine (left panel) or 5 μM IKE (right panel), alone or in combination with 100 μM Trolox.**(C)** Quantification of flow cytometric analysis of PDAC cells stained with general oxidation sensor when treated with indicated conditions (cystine depletion carried out for 8 hours, IKE treatment carried out for 6 hours). Data represented as fold change in number of positive cells, with error = ± SD, with n = 4 independent cell lines tested in triplicate. x = no significant difference by Tukey's test. Experiments were conducted in collaboration with Dr. Michael A. Badgley et al. Figures were produced by Drs. Michael A. Badgley and Ken Olive.

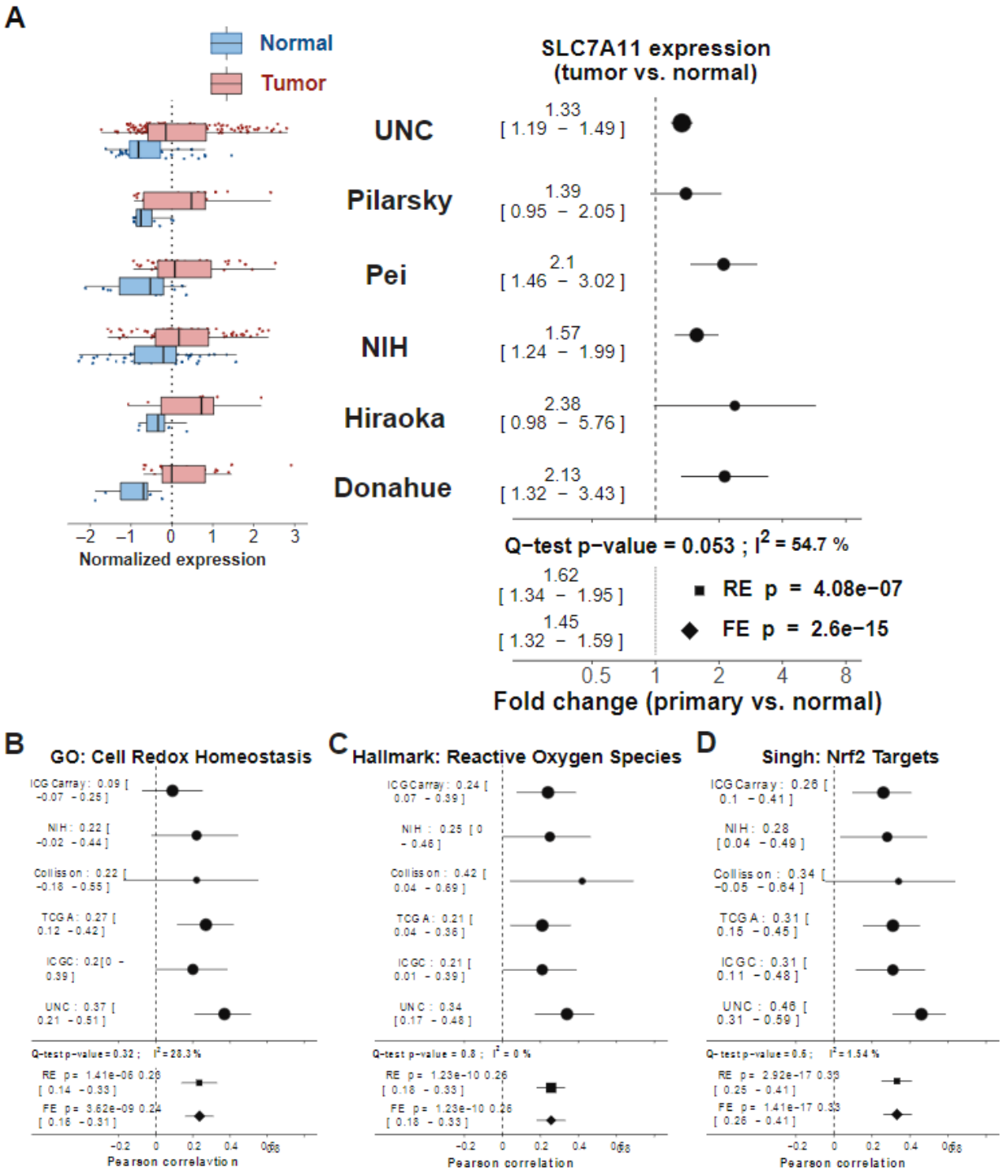

Figure 13. Expression and outcome associations of SLC7A11.
(A) SLC7A11 is overexpressed in primary PDAC tumors (red) as compared to normal control (blue) tissue in multiple pancreatic cancer data sets. Effect size estimates of data are shown in the right half of the panel with their 95% confidence interval per study as well as meta-analytic summaries using random (RE) and fixed effect (FE) models. Q-test and indicate measures of inter-study heterogeneity. **(B-D)** Correlation of SLC7A11 expression with curated gene sets. Panels show effect size estimates with their 95% confidence interval per study as well as meta-analytic summaries using random (RE) and fixed effect (FE) models. Q-test and indicate measures of inter-study heterogeneity. Experiments were conducted in collaboration with Dr. Michael A. Badgley et al. Figures were produced by Drs. Michael A. Badgley and Ken Olive.

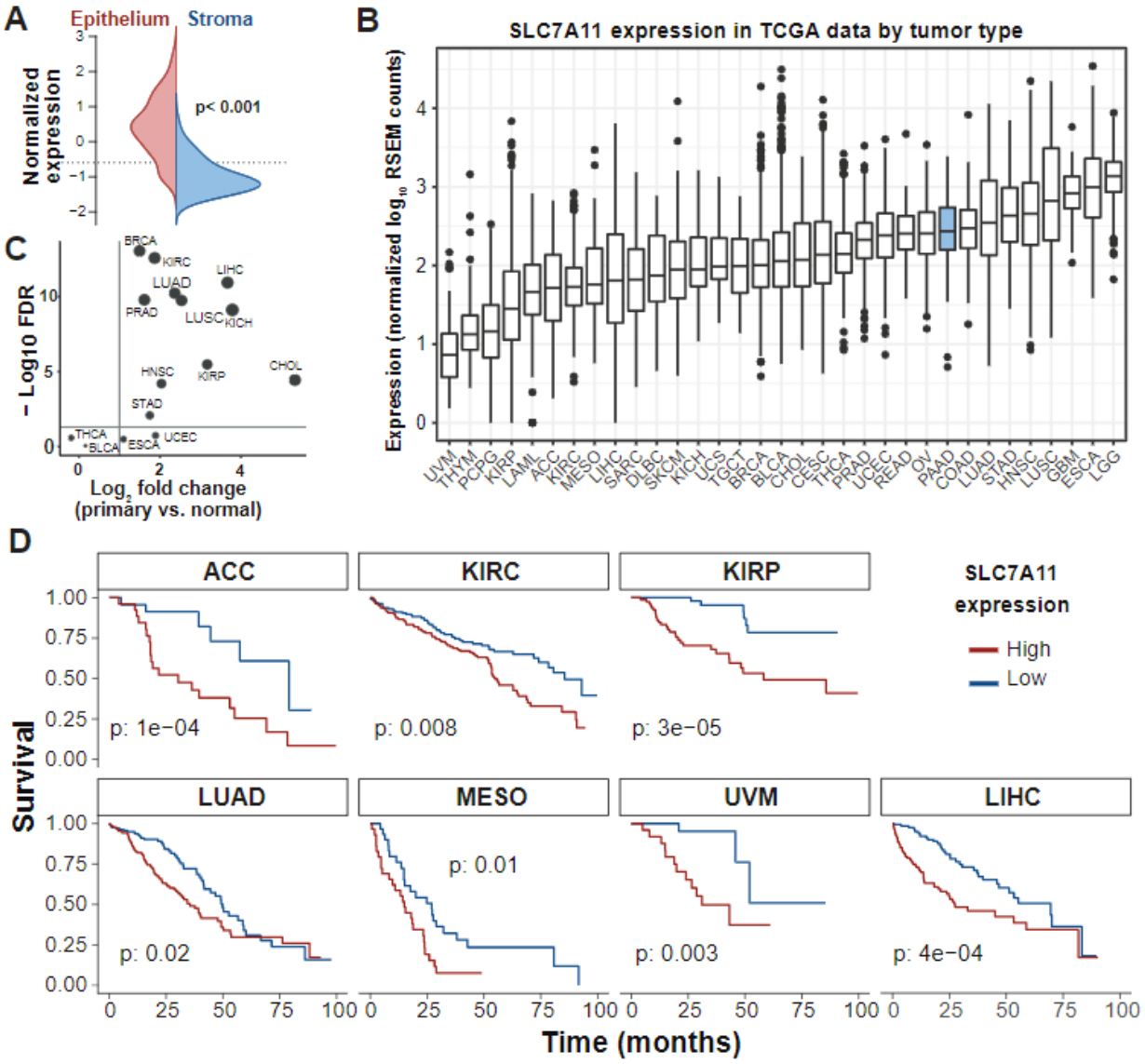

Figure 14. Expression of SLC7A11 in PDAC.
(A) Laser-captured, micro dissected (LCM) RNA-Seq from matched human PDAC epithelium and stroma shows enrichment of expression in epithelial tissue (distribution shown in red) when compared to neighboring stromal tissue, which is not malignant (distribution shown in blue). **(B)** Normalized expression of SLC7A11 across 31 tumor types from TCGA data showing high overall expression in pancreatic ductal adenocarcinoma (PAAD, blue), with generally low variance. **(C)** Analysis of SLC7A11 mRNA expression in TCGA data sets of tumors for which at least 6 normal samples were available shows overexpression of SLC7A11 in most tumor types **(D)** for which there is a difference in outcome between patients expressing varying levels of SLC7A11, high levels are consistently associated with a worse prognosis (log rank test p-values indicated, survival curves shown in red). Abbreviations used according to standard TCGA nomenclature. Experiments were conducted in collaboration with Dr. Michael A. Badgley et al. Figures were produced by Drs. Michael A. Badgley and Ken Olive.

SLC7A11 Deletion in KPC Mice Induces Tumor Ferroptosis and Extends Survival

To learn whether pancreatic tumors in mice depend on system x_c^- for survival, we employed a dual recombinase genetic engineering strategy based on the KPC mouse model[7].

Kras$^{FSF.G12D/+}$; *Tp53*$^{R172H/+}$; *Pdx1FlpO*$^{tg/+}$; *Slc7a11*$^{Fl/Fl}$; *Rosa26*$^{CreERT2/+}$ (KPFSR) mice **(Figure 15)** spontaneously develop PDAC driven by FlpO-dependent activation of mutant *Kras* and germline expression of mutant *Tp53*. These tumors are identical in genotype and phenotype to the KPC model, but the administration of tamoxifen induces systemic deletion of *SLC7A11* through the action of Cre recombinase expressed from the *Rosa26* locus **(Figure 15 and 16a-c)**.

To test the effect of SLC7A11 deletion in established pancreatic tumors, We randomized KPFSR mice bearing 4 to 7 mm tumors to receive six daily doses of vehicle or tamoxifen and monitored tumor growth by ultrasound[8]. Deletion of *SLC7A11* in established tumors of KPFSR mice nearly doubled median survival compared with vehicle treatment **(Figure 17a)**. Most recombined tumors exhibited a period of stable disease or partial response—and one underwent a complete regression—but these responses were never observed in vehicle-treated mice **(Figures 17b, 16d-f, and 18a)**. Critically, the addition of NAC to the drinking water of tamoxifen-treated mice restored baseline survival and eliminated tumor responses, supporting a link to cysteine metabolism **(Figures 17, a-b)**. At necropsy, escaped tumors exhibited evidence of incomplete *SLC7A11* recombination by polymerase chain reaction and restored protein expression by Western blotting, which suggests the outgrowth of un-recombined tumor cells **(Figure 18b-c)**.

The study of *in vivo* ferroptosis has been hindered by the lack of a validated, selective biomarker and the absence of a histopathological characterization of the phenomenon in tissues. Within tamoxifen-treated KPFSR tumors, we observed numerous lesions of ballooned epithelial cells with lipid droplet-like structures and intermittent mega-mitochondria, often juxtaposed to necrotic regions—a phenotype only occasionally observed in vehicle-treated KPFSR and untreated KPC tumors **(Figures 13c-d, and 18d).** These lesions exhibited no alterations in apoptosis or proliferation markers **(Figures 19a-b)**, but they did display accumulation of 4-hydroxynonenal (4HN)

(Figures 19c-e), a by-product of lipid peroxidation, making them candidates for *in vivo* ferroptosis. Critically, no pathologies were observed in non-pancreatic tissues of tamoxifen-treated KPFSR mice, indicating a tumor-selective phenotype. Transmission electron microscopy (TEM) and Oil Red O staining of tamoxifen-treated KPFSR tumors confirmed the presence of abnormally large lipid droplets **(Figures 17d and 19f)**. TEM also revealed structural aberrations in the mitochondria of malignant epithelial cells, including disrupted cristae and compromised membrane integrity **(Figure 17)**, which is consistent with the results of prior *in vitro* studies[9]. Finally, we performed laser capture microdissection and RNA sequencing to isolate malignant epithelial cells from KPFSR tumors. We found that genes up-regulated in response to *SLC7A11* deletion were enriched in a ferroptotic expression signature from erastin-treated HT-1080 cells **(Figure 17f)**[10]. We conclude that the phenotype observed in tamoxifen-treated KPFSR tumors is a histologically identifiable, *in vivo* manifestation of ferroptosis.

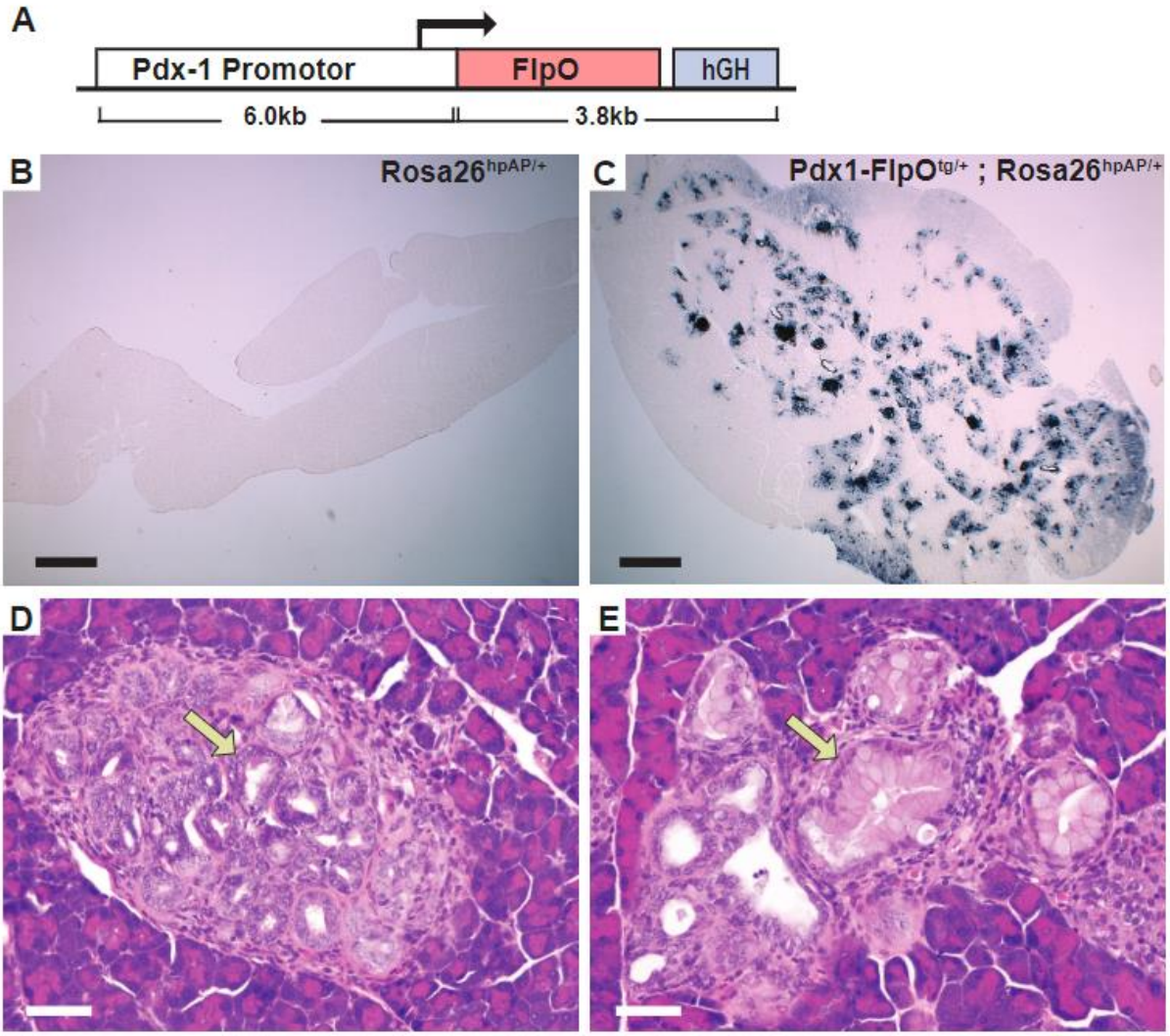

F

Effective genotypes of KPFSR tissues:	Pancreas		Non-pancreas	
	Vehicle	Tamoxifen	Vehicle	Tamoxifen
	Kras$^{12D/+}$	*Kras*$^{12D/+}$	*Kras*$^{+/-}$	*Kras*$^{+/-}$
	Tp53$^{172H/+}$	*Tp53*$^{172H/+}$	*Tp53*$^{+/-}$	*p53*$^{+/-}$
	Slc7a11$^{+/+}$	*Slc7a11*$^{-/-}$	*Slc7a11*$^{+/+}$	*Slc7a11*$^{-/-}$

Figure 15. Pdx1-FlpO allele design and validation.
(A) Design of the Pdx1-FlpOallele (B and C) Pdx1-FlpO founders were crossed to alkaline phosphatase. Flp reporter mice (gift, Dr. Susan Dymecki, Harvard University) to visualize recombination in the pancreas. Frozen sections of pancreata from Rosa26hpAP/+ **(B)** or Pdx1-FlpO; Rosa26hpAP/+ **(C)**. Mice were stained for alkaline phosphatase activity (dark blue). Founder lines exhibiting prominent alkaline phosphatase activity in the pancreas were used in further breeding. Bars = 200μm. **(D-E)** The Pdx1-FlpO strain was crossed with additional strains to generate KrasLSL.G12D/+; p53R172H/+; Pdx1-FlpOtg/+; Slc7a11Fl/Fl (KPFS) mice. Histopathological examination of the pancreas of young KPFS mice revealed the spontaneous acinar-to-ductal metaplasia (ADM indicated with arrow, panel D) and pancreatic intraepithelial neoplasia (PanIN indicated with arrow, panel E), both precursors to tumor development. Bar = 50μm. **(F)** Table indicating effective genotypes of tissues in the KPFSR mouse. Experiments were conducted in collaboration with Dr. Michael A. Badgley et al. Figures were produced by Drs. Michael A. Badgley and Ken Olive.

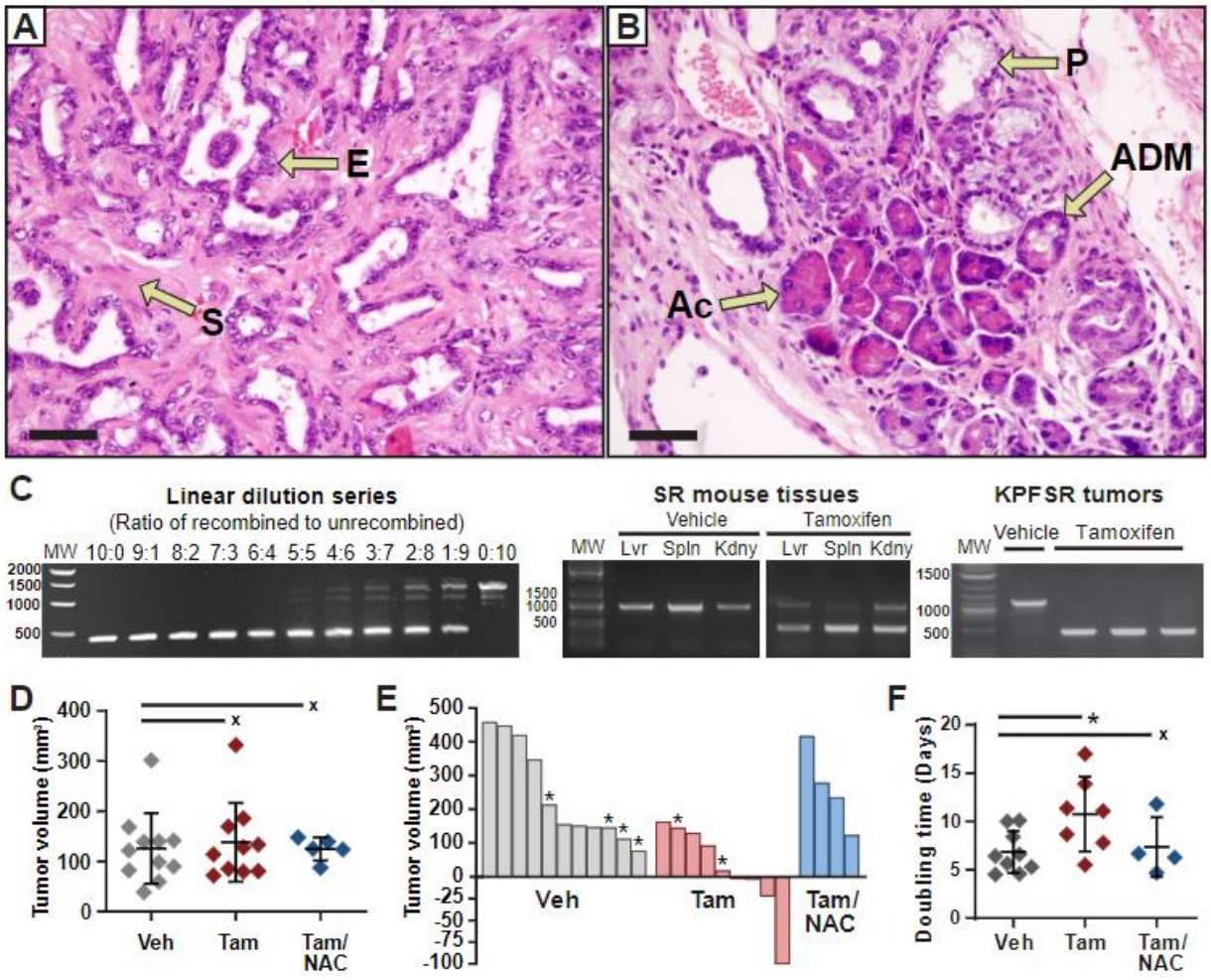

Figure 16. Analyses of KPFSR tumors.
(A) Representative KPFSR tumor stained with hematoxylin and eosin (H&E). Desmoplastic stroma is stained in pink while nuclei are stained in purple. Scale bar is 50 µm. Arrows indicate malignant epithelial structure **(E)** versus the stromal component (S). **(B)** Representative precursor lesions from KPFSR pancreas stained with H&E. Arrows highlight a normal acinus (Ac), acinar-to-ductal metaplasia (ADM), and an early pancreatic intraepithelial neoplasia (PanIN). Scale bar is 50 µm. **(C)** Left panel: Dilution series of mixtures of completely recombined DNA to unrecombined DNA, in the indicated ratios. Note preferential detection of recombined allele, with detection of only a faint unrecombined band in the 4:6 lane. Unrecombined, 1285bp; Recombined, 450bp. Middle panel: PCR analysis of DNA recombination in tissues (liver, Lvr; spleen, Spln; kidney, Kdny) from SR mice treated with tamoxifen. Right panel: recombination as detected by PCR in KPFSR tumors treated for 6 days with tamoxifen. **(D)** Analysis of tumor volumes at the time of enrollment on preclinical survival study. Data show mean± SD. x = Not statistically significant by Tukey's test. **(E)** Waterfall plots of tumor growth that shows either best regression relative today 0 or the % tumor volume increase at day 10 (interpolated value for all tumors lacking an ultrasound at day 10.) Mice that died prior to day 10 are indicated by an asterisk. **(F)** Tumor growth rates from tumors in the survival study. Data show mean ± SD, n = 9 for vehicle, n = 7 for tamoxifen, n = 4 for tamoxifen/NAC (only tumors with at least 4 volumes are utilized in analysis). * = $p < 0.05$, x = not significant. Analyzed by Student's t-test. Experiments were conducted in collaboration with Dr. Michael A. Badgley et al. Figures were produced by Drs. Michael A. Badgley and Ken Olive.

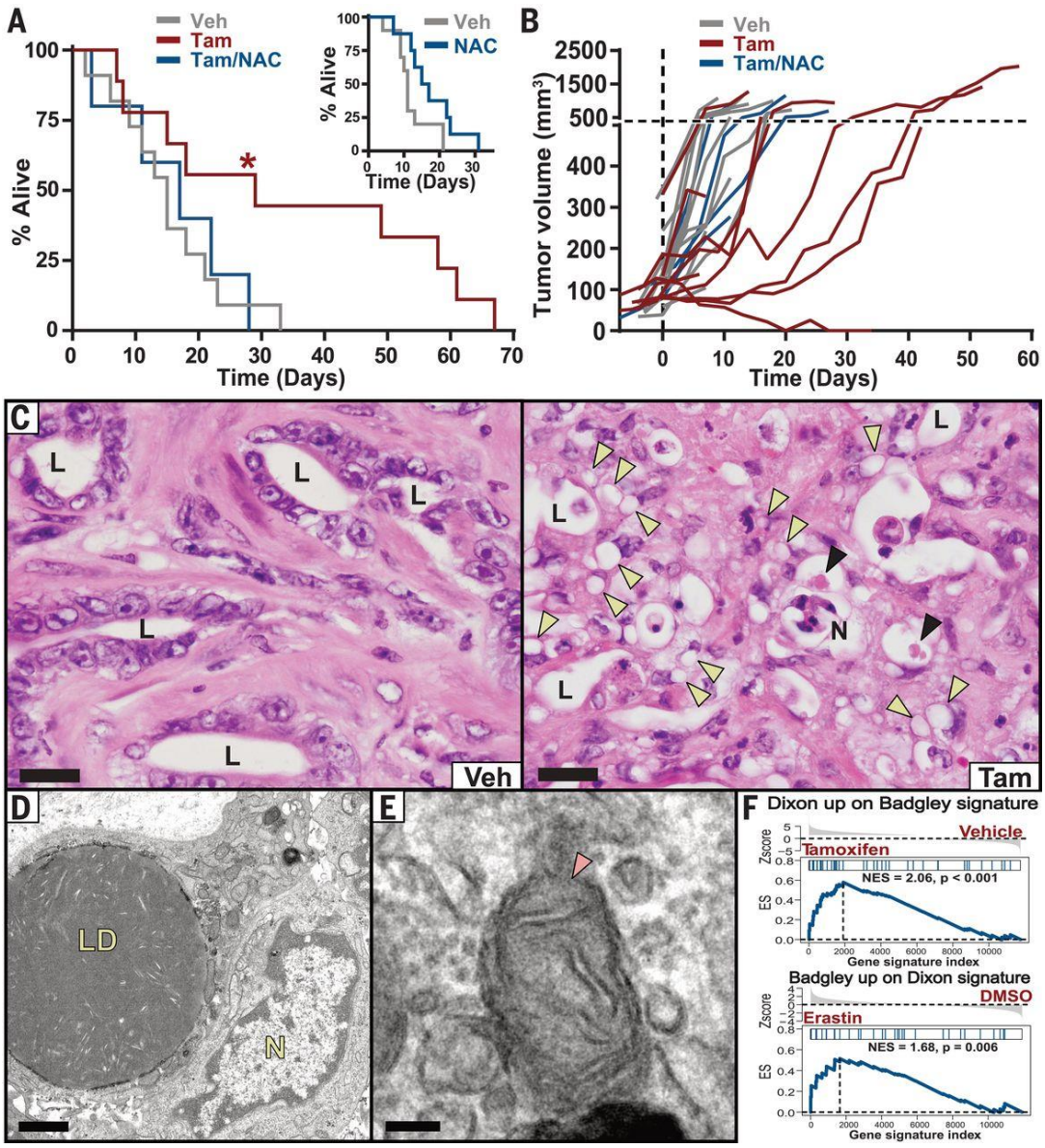

Figure 17. Deletion of Slc7a11 in KPC mice induces tumor ferroptosis.
A) Survival of KPFSR mice treated with vehicle (Veh) (n = 11, median 15 days), tamoxifen (Tam) (n = 9, median 29 days), or tamoxifen/NAC (n = 5, median 17 days). *P < 0.0295, log-rank. Inset shows the survival of KPC mice treated with NAC alone (n = 8, median 16 days) versus historical saline-treated controls (n = 10, median 11 days). **B)** Growth curves for each KPFSR tumor. **C)** Hematoxylin and eosin (H&E)–stained sections of tumor tissue from KPFSR mice treated with vehicle (left) or tamoxifen (right). L, lumen of malignant epithelium; N, necrosis; yellow arrowheads, lipid droplets; black arrowheads, megamitochondria; scale bars, 20 μm. D-E) TEM images from tamoxifen-treated KPFSR tumors. LD, lipid droplets; N, nucleus; arrowhead indicates damaged mitochondrion. Scale bar **(D)**, 1μm; scale bar **(E)**, 100 nm. **F)** Gene set enrichment analysis. Top panel depicts enrichment of a published ferroptosis expression signature (Dixon) among genes differentially expressed in tamoxifen-treated KPFSR epithelia (Badgley) (P < 0.001). Bottom panel depicts the reciprocal comparison (P < 0.006). NES, normalized enrichment score; DMSO, dimethyl sulfoxide. Experiments were conducted in collaboration with Dr. Michael A. Badgley et al. Figures were produced by Drs. Michael A. Badgley and Ken Olive.

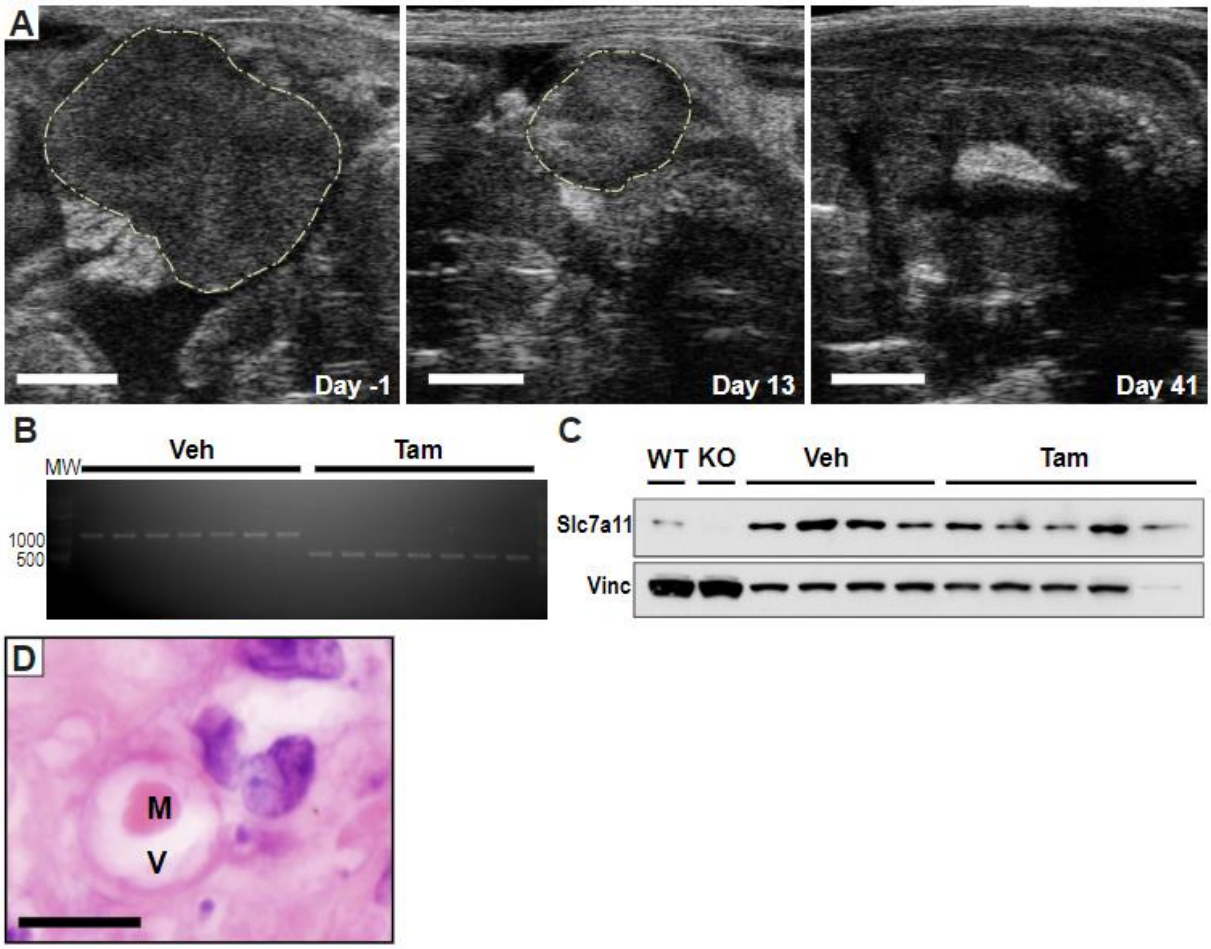

Figure 18. Ultrasound, recombination, and histopathology of KPFSR tumors.
(A) Ultrasounds from a tamoxifen-treated KPFSR mouse that underwent complete regression, on study days -1, 13, and 41 of treatment. Hashed yellow lines indicates tumor. Scale bar = 2 mm. **(B)** PCR analysis of recombination in endpoint tumors from randomized survival study. Results indicate > 60% recombination of SLC7A11 in endpoint samples (See Fig S6). **(C)** Western blot of SLC7A11 in endpoint tumor samples show limited changes in protein levels in control or tamoxifen treated groups. Controls are wildtype (WT) mouse embryonic fibroblasts (MEFs) and knockout (KO) MEFs generated from the conditional SLC7A11 allele. **(D)** High magnification image of ferroptoptic lesion, containing megamitochondria (M) and cytoplasmic vacuolization (V). Scale bar = 10μm. Experiments were conducted in collaboration with Dr. Michael A. Badgley et al. Figures were produced by Drs. Michael A. Badgley and Ken Olive.

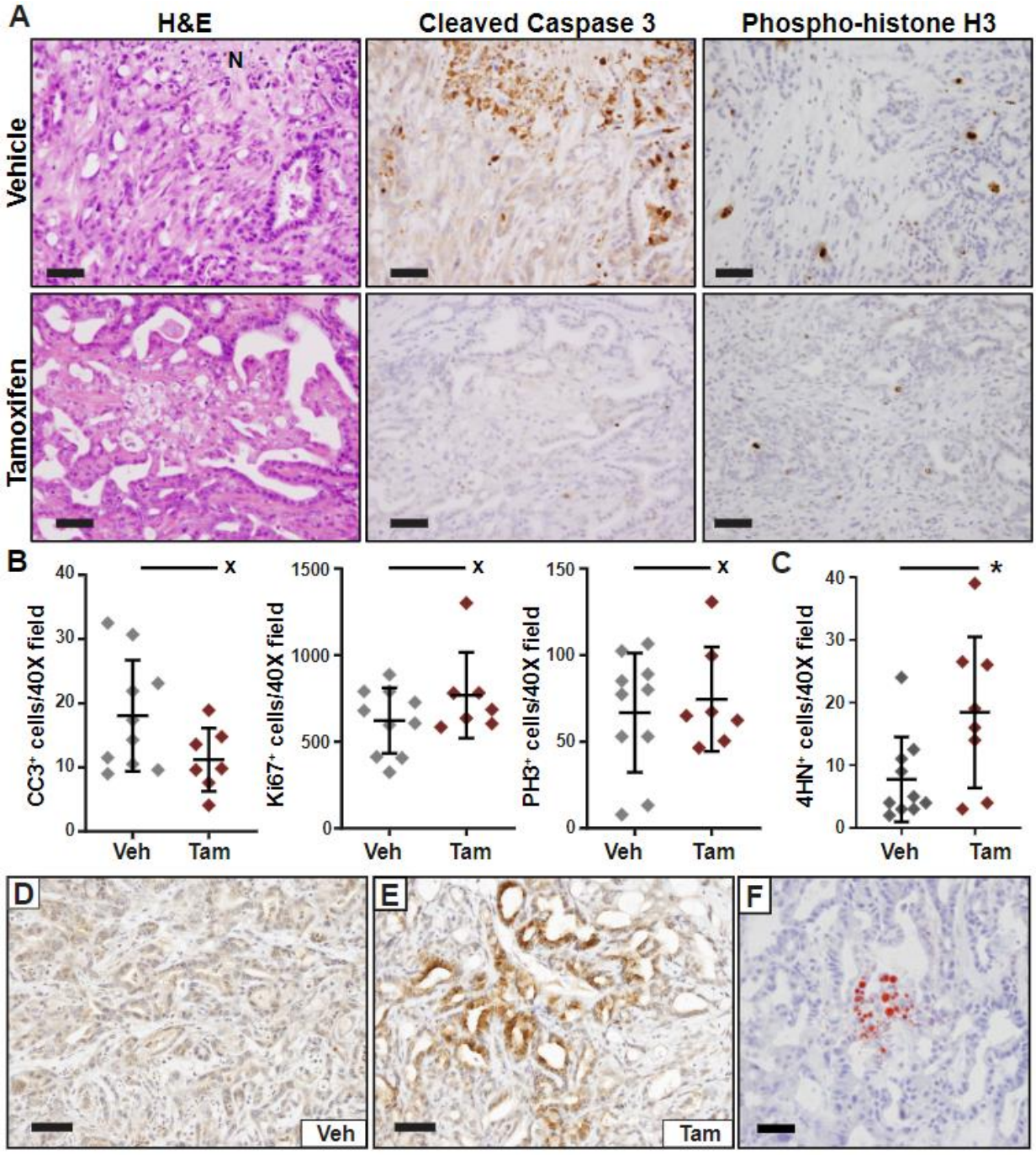

Figure 19. Histopathological and immunohistochemical analyses of KPFSR tumors.
(A) H&E, cleaved caspase 3 (CC3), and phospho-histone H3 (PH3) staining of KPFSR tumors from vehicle and tamoxifen treated mice. Tamoxifen treated sample shows an example of tissue damaged from SLC7A11 deletion. This region appears CC3 negative but does not exhibit notable changes in PH3 staining. Scale bar indicates 50μm. **(B-C)** Quantification of CC3, Ki67, PH3, and 4-hydroxynonenal (4HN) staining from both treatment groups. Data are mean± SD. No statistically significant changes are detected by Student's t-test when comparing vehicle and tamoxifen groups for any stain save 4HN (C) where * $p < 0.05$. **(D-E)** Images of 4HN stained tumors showing the enrichment of 4HN lesions in samples from tamoxifen treated mice. Scale = 50μm. (F) Oil Red O staining of tamoxifen treated tumors showing lipid droplets (in red) of large size. Scale bar is 50μm. Experiments were conducted in collaboration with Dr. Michael A. Badgley et al. Figures were produced by Drs. Michael A. Badgley and Ken Olive.

Human PDA Cells Require GSH and CoA to Prevent Ferroptosis

Prior studies have indicated that cysteine regulates ferroptosis primarily through the synthesis of GSH, a critical cofactor for the lipid peroxide–detoxifying enzyme GPX4[3]. We found that cysteine depletion rapidly reduced GSH levels in two human PDAC cell lines **(Figure 20a)**. Furthermore, co-treatment with the membrane-permeable GSH analog glutathione ethyl ester prevented lipid oxidation and ferroptosis **(Figure 20b-e)**. However, inhibition of GSH biosynthesis using buthionine sulfoximine (BSO) **(Figure 20f)** did not induce lipid ROS or reduce cell viability **(Figures 21, a-b)**, which demonstrates that GSH loss is not sufficient to induce ferroptosis in PDAC cells[11].

To investigate whether additional cysteine-derived metabolites contribute to the regulation of ferroptosis, we traced the metabolism of exogenous cystine by using ^{13}C-labeled cystine and measuring labeled metabolites by mass spectrometry. In addition to exhibiting rapid flux into GSH pools, cystine was also converted to coenzyme A (CoA) over 24 hours **(Figures 21c-d)**; no flux was observed into taurine, lactate, citrate, or glutamate **(Figure 20f)**. CoA is synthesized from cysteine via the pantothenate pathway and plays a role in many metabolic pathways, particularly lipid metabolism. Both CoA and a potential downstream product coenzyme Q_{10} (CoQ_{10}) have been shown to affect sensitivity to ferroptosis[12,13] We found that system x_C^- inhibition reduced CoA levels and increased levels of pantothenate **(Figure 21e)**, a metabolite upstream of cysteine incorporation in CoA synthesis. Moreover, treatment of PDAC cells with exogenous CoA[14] prevented IKE-induced ferroptosis **(Figure 21f)** whereas pantothenate kinase inhibition with PANKi sensitized cells to IKE **(Figures 22a-c)**. Notably, PANKi combined synergistically with BSO to induce ferroptosis **(Figures 21g and 22d)**. Co-treatment with idebenone (a membrane-permeable analog of CoQ_{10}) or a monounsaturated fatty acid blocked BSO/PANKi-induced ferroptosis, whereas saturated or polyunsaturated fatty acids did not **(Figure 22e)**, similar to prior observations with IKE[15]. Together, these experiments demonstrate that CoA and GSH cooperate to regulate ferroptosis in human PDAC cells **(Figure 22f)**.

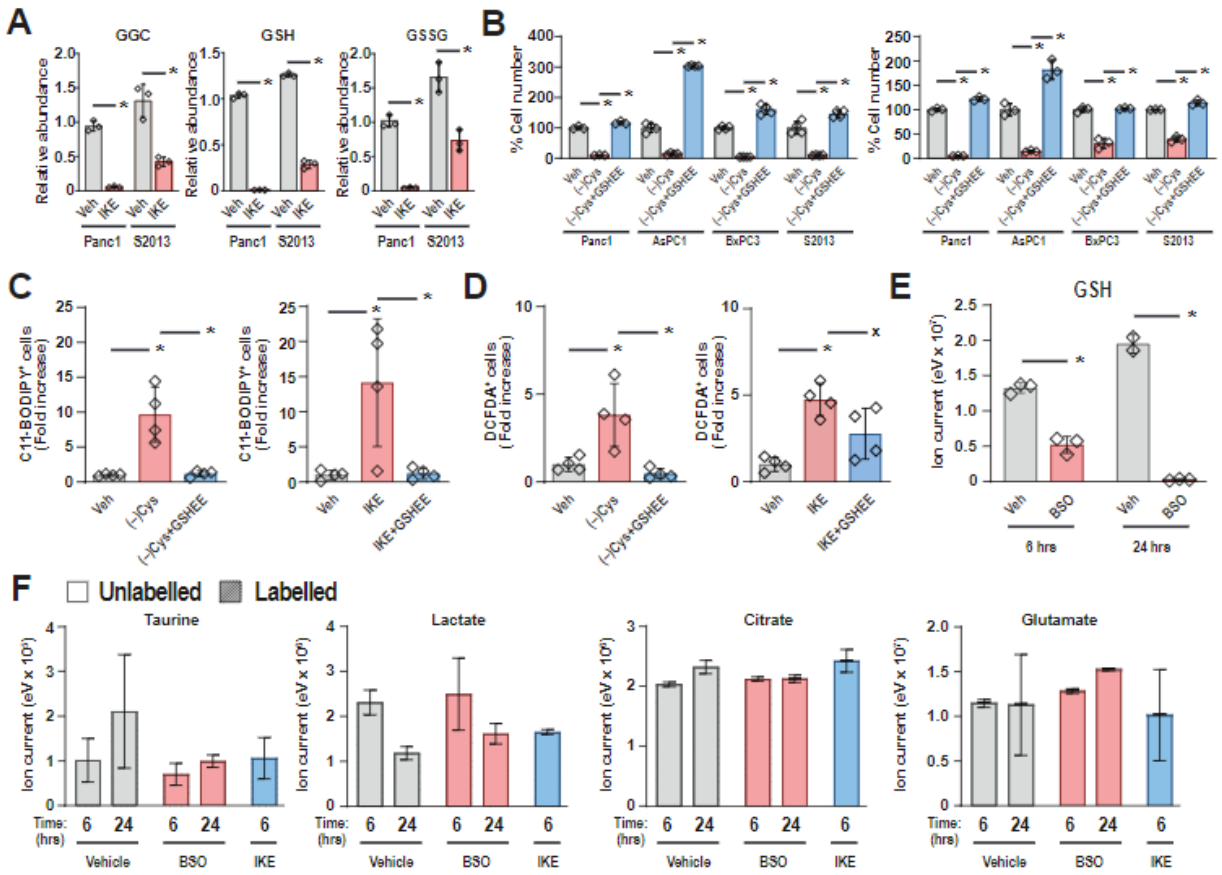

Figure 20. Metabolomics analysis of cysteine and GSH utilization.
(A) Measurement of gamma glutamyl cysteine (gGC), GSH, and GSSG in two sensitive cell lines treated with 0.1% DMSO (Veh) or 5μM IKE for six hours. Data are mean±SD with n = 3 biological replicates. * $p < 0.05$, Student's t-test. **(B)** GSH-EE rescue of cystine withdrawal and system xC– inhibition in sensitive cell lines. Data are mean ± SEM with n = 3 independent experiments.* $p < 0.05$ by Tukey's test. **(C-D)** Flow cytometric analyses of sensitive cell lines grown without cystine (-cys) or with 5μM IKE and in the presence of GSH-EE for 6-8 hours. Cells were stained with C-11 BODIPY and DCFDA to mark lipidoxidative stress and general oxidative stress, respectively. Data are means ± SD with n = 4 independent cell lines tested in triplicate. * $p < 0.05$ by Tukey's test. x = not significant. **(E)** GSH levels as measured by mass spectrometry in PANC-1 cells treated with vehicle or 600μM BSO for listed time points. Data aremeans± SD with n = at least 2 biological replicates.* $p < 0.05$ by Student's t test. **(F)** Measurement of labeled and unlabeled levels of taurine, lactate, glutamate, and citrate in PANC-1 treated with vehicle (0.05% DMSO), 5μM IKE, or 600μM BSO for indicated times. (All comparisons not significant by Tukey's test). No labeled species for these metabolites were detected. Experiments were conducted in collaboration with Dr. Michael A. Badgley et al. Figures were produced by Drs. Michael A. Badgley and Ken Olive.

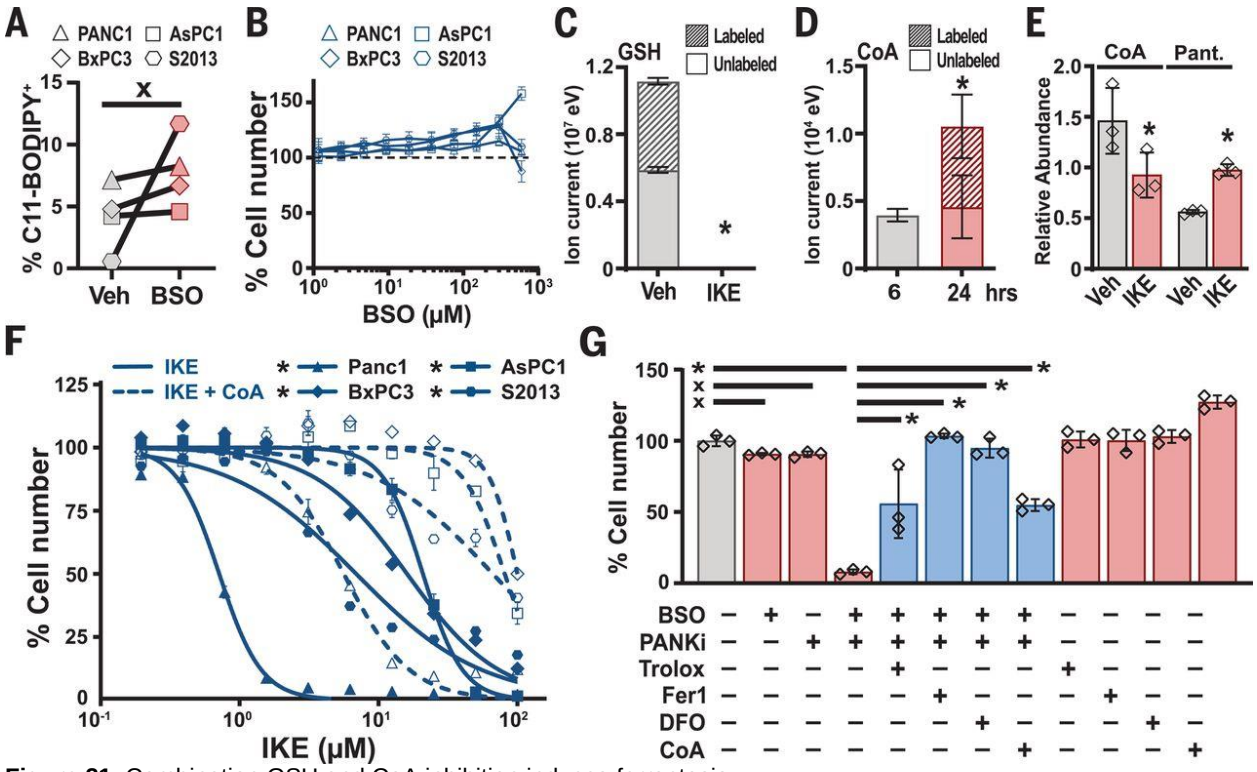

Figure 21. Combination GSH and CoA inhibition induces ferroptosis.
A) Flow cytometry for C11-BODIPY fluorescence in four human PDAC lines treated for 6 hours with 150 μM BSO. Paired t test was performed. **B)** Viability of human PDAC cells treated for 24 hours with indicated concentrations of BSO. **C)** Liquid chromatography time-of-flight mass spectrometry (LC-TOF-MS) analysis of GSH in PANC-1 cells labeled for 6 hours with 13C-cystine combined with vehicle or 5μM IKE. Student's t test was performed. **D)** LC-TOF-MS analysis of CoA in PANC-1 cells labeled for 6 hours with 13C-cystine, after 6 or 24 hours. Student's t test was performed. **E)** Liquid chromatography triple quadrupole tandem mass spectrometry measurements of CoA and pantothenate (Pant.) levels in Panc-1 cells treated with vehicle and IKE for 6 hours. Student's t test was performed. **F)** Viability of human PDAC cell lines treated with IKE, alone or in combination with 200 μM CoA. Student's t test comparing maximal cytotoxicity ± CoA was performed. **G)** PANC-1 cells treated for 24 hours with combinations of 300 μM BSO and 5 μM PANKi along with Trolox, Fer-1, DFO, or CoA, as described in Fig. 1C. Tukey test was performed. In **(A)** to **(G)**, *P < 0.05 and x indicates not significantly different. In **(A)**, **(B)**, **(E)**, and **(F)**, data are means ± SEM from three independent experiments. In **(C)** and **(D)** data are means ± SD from three biological replicates. In **(E)**, *P < 0.05 comparing maximal cytotoxicity in CoA-treated versus untreated conditions for each line, Student's t test. In **(F)**, *P < 0.05, one-way ANOVA with posthoc Tukey test. Experiments were conducted in collaboration with Dr. Michael A. Badgley et al. Figures were produced by Drs. Michael A. Badgley and Ken Olive.

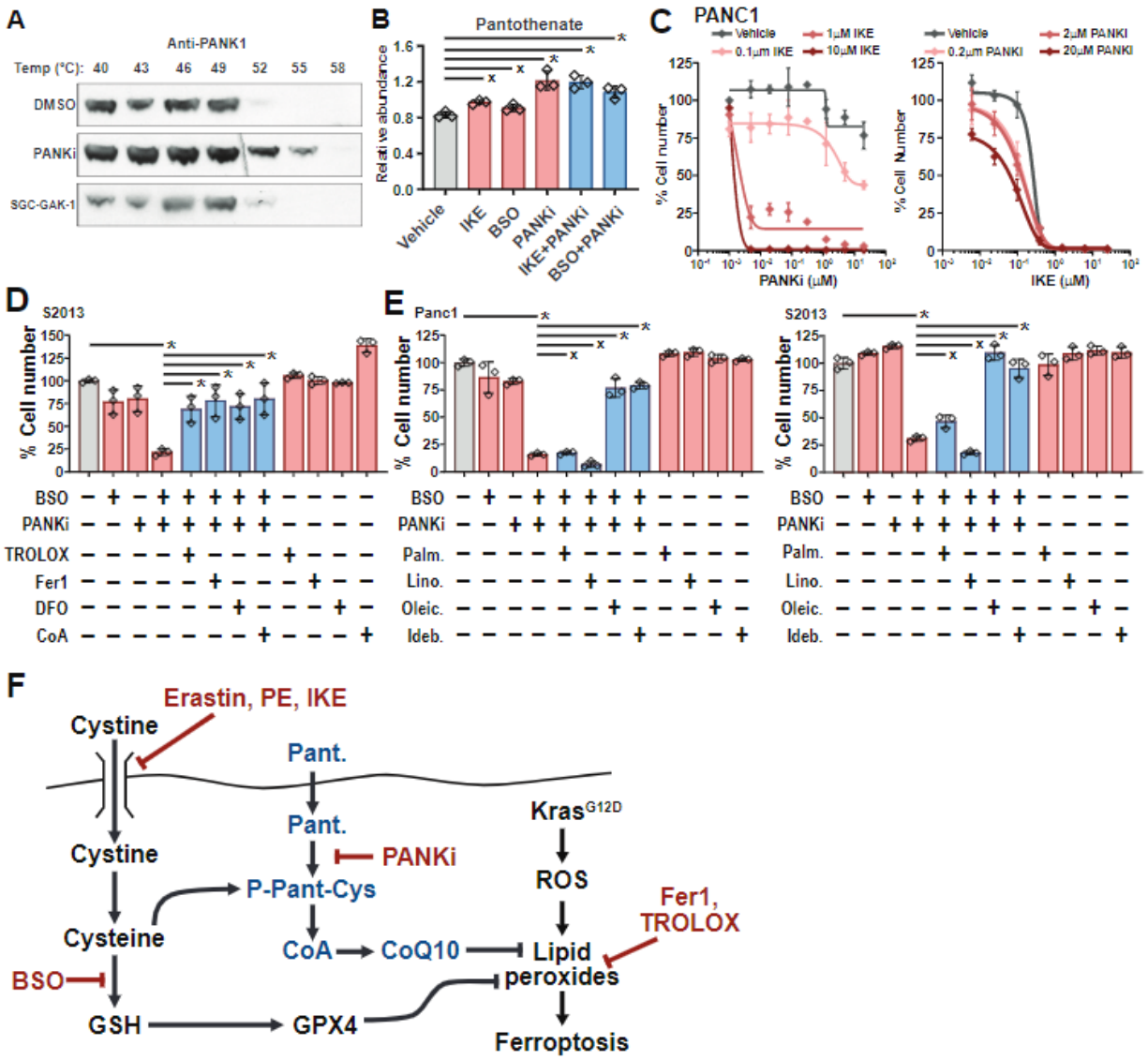

Figure 22. GSH and Coenzyme A synthesis in ferroptosis.
(A) Cell based thermal shift assay confirms target engagement of PANK inhibitor. **(B)** Mass spectrometry measurements of pantothenic acid in given treatment conditions: vehicle (0.1% DMSO), IKE (5μM), BSO (75μM), PANKi (5μM), and various combinations. **(C)** Dose response curves of PANKi in combination with different concentrations of IKE andthe inverse experiment. **(D)** Treatment of S-2013 PDAC cell line with combinations of BSO, PANKi, and ferroptosis rescue agents. **(E)** Treatment of PANC-1 and S-2013 PDAC cells with combinations of BSO, PANKi, palmitic acid (a saturated fatty acid), linoleic acid (a poly-unsaturated fatty acid), oleic acid (a mono-unsaturated fatty acid) and idebenone. **(F)** Model of the roles of cysteine utilization in suppressing ferroptosis. All data are means± SEM of three independent experiments. *p < 0.05 by Tukey's test. x = not significant. . Experiments were conducted in collaboration with Dr. Michael A. Badgley et al. Figures were produced by Drs. Michael A. Badgley and Ken Olive.

Cyst(e)inase Treatment Induces Tumor-Selective Ferroptosis in KPC Mice

Finally, we sought a pharmacological means to target cysteine metabolism in pancreatic tumors. Drug delivery is compromised in PDAC because of the effects of fibrosis on tissue perfusion[16]. Although current system x_C^- inhibitors are not optimized for the PDAC microenvironment, the engineered enzyme cyst(e)inase is well-tolerated in mammals, has a long half-life, and potently degrades both cystine and cysteine in circulation[17]. In vitro, cyst(e)inase treatment induced lipid oxidation and reduced the viability of IKE-sensitive PDAC lines; this was largely prevented by co-treatment with ferroptosis inhibitors **(Figures 23a-c and 24a-b)**. To determine the effects of cyst(e)inase on pancreatic tumors in vivo, we treated tumor-bearing KPC mice for 10 days with vehicle, low-dose cyst(e)inase, or high-dose cyst(e)inase (n = 2 for each treatment). Histopathological examination of cyst(e)inase-treated tumors revealed a severe ferroptosis phenotype, with extensive lipid droplet formation, stromal disruption, decompressed blood vessels, and necrosis **(Figures 23d-e and 25a-b)**. TEM revealed enlarged lipid droplet formation, extracellular lipid droplets, and mitochondrial defects, preferentially in cyst(e)inase-treated KPC tumors **(Figures 15f-i)**. Ferroptotic lesions were generally 4HN positive and cleaved caspase 3 negative **(Figure 26)**. Finally, four additional KPC mice were treated with high-dose cyst(e)inase, and their tumor growth was monitored by ultrasound. Notably, all four tumors exhibited stabilizations or regressions, whereas historical vehicle-treated controls never stabilized **(Figure 23j)**. Thus, we conclude that the therapeutic depletion of cysteine (cystine) can induce ferroptosis in Kras/p53 mutant pancreatic tumors in mice.

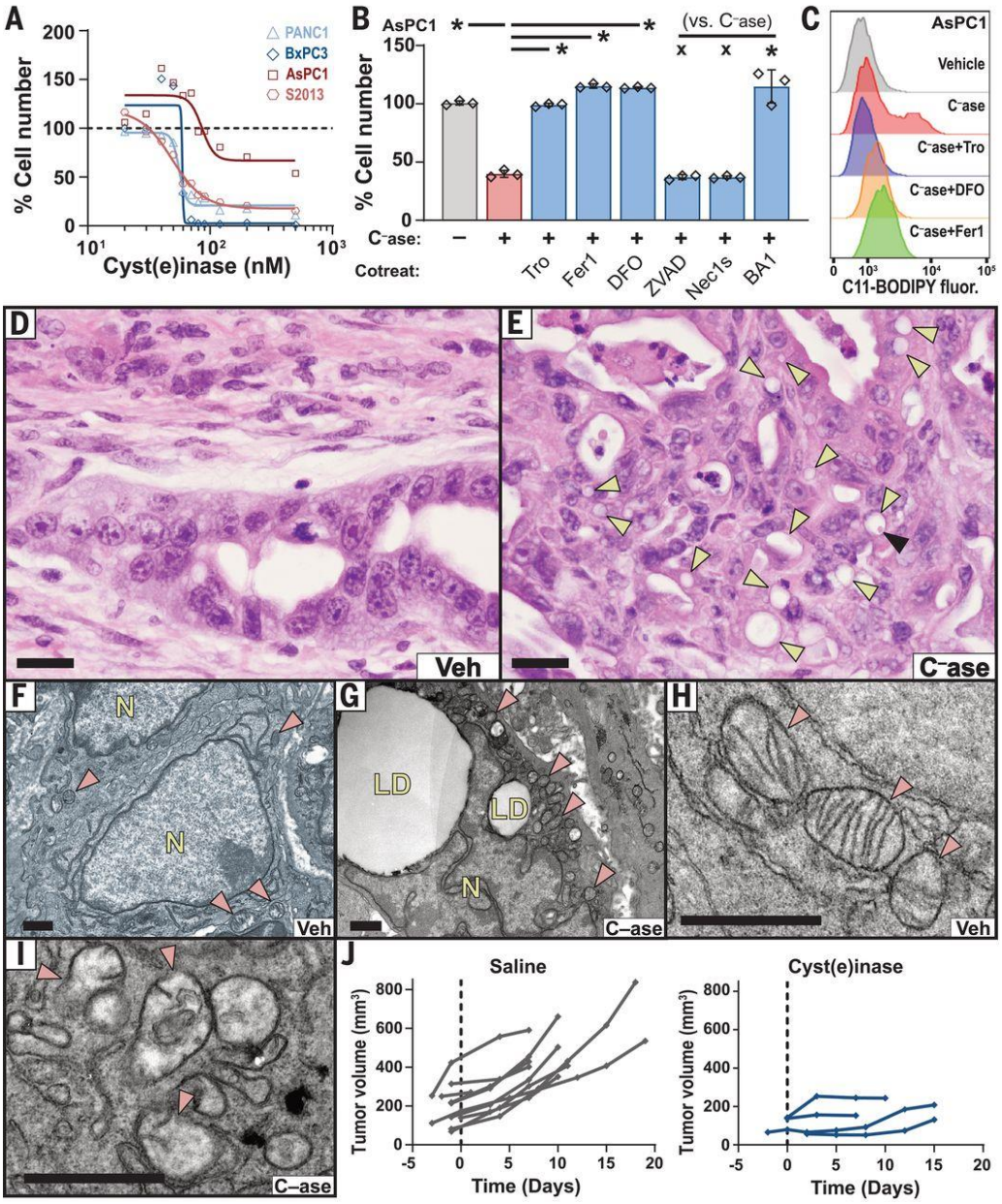

Figure 23. Cyst(e)inase treatment induces tumor-selective ferroptosis in KPC mice.
A) Viability of human PDAC lines cultured with varying concentrations of cyst(e)inase for 48 hours (AsPC1) or 72 hours (PANC-1, BxPC3, and S2-013). **B)** Viability of AsPC1 cells treated with 90 nM cyst(e)inase (C⁻ase) for 72 hours, alone or in combination with indicated agents, under conditions described in Fig. 1C. **C)** C11-BODIPY fluorescence was measured by flow cytometry in AsPC-1 cells after 24 hours of treatment with 90 nM cyst(e)inase, alone or in combination with indicated agents, under conditions described in Fig. 1C. **D-E)** H&E-stained sections of pancreatic tumors from KPC mice treated with vehicle or cyst(e)inase. Yellow arrowheads indicate lipid droplets; black arrowhead indicates megamitochondrion; scale bars, 20 μm. **F-I)** TEM of pancreatic tumors from the KPC model treated with vehicle [**(F)** and **(H)**] or cyst(e)inase [**(G)** and **(I)**]. Red arrowheads indicate mitochondria; LD, lipid droplets; N, nucleus; scale bars, 1 μm. **J)** Tumor growth curves from KPC mice treated with saline (historical controls) or 100 mg/kg cyst(e)inase, every other day, intraperitoneally. For **(A)** and **(B)**, data depict mean of three biological replicates. *$P < 0.05$; x, not significant. Experiments were conducted in collaboration with Dr. Michael A. Badgley et al. Figures were produced by Drs. Michael A. Badgley and Ken Olive.

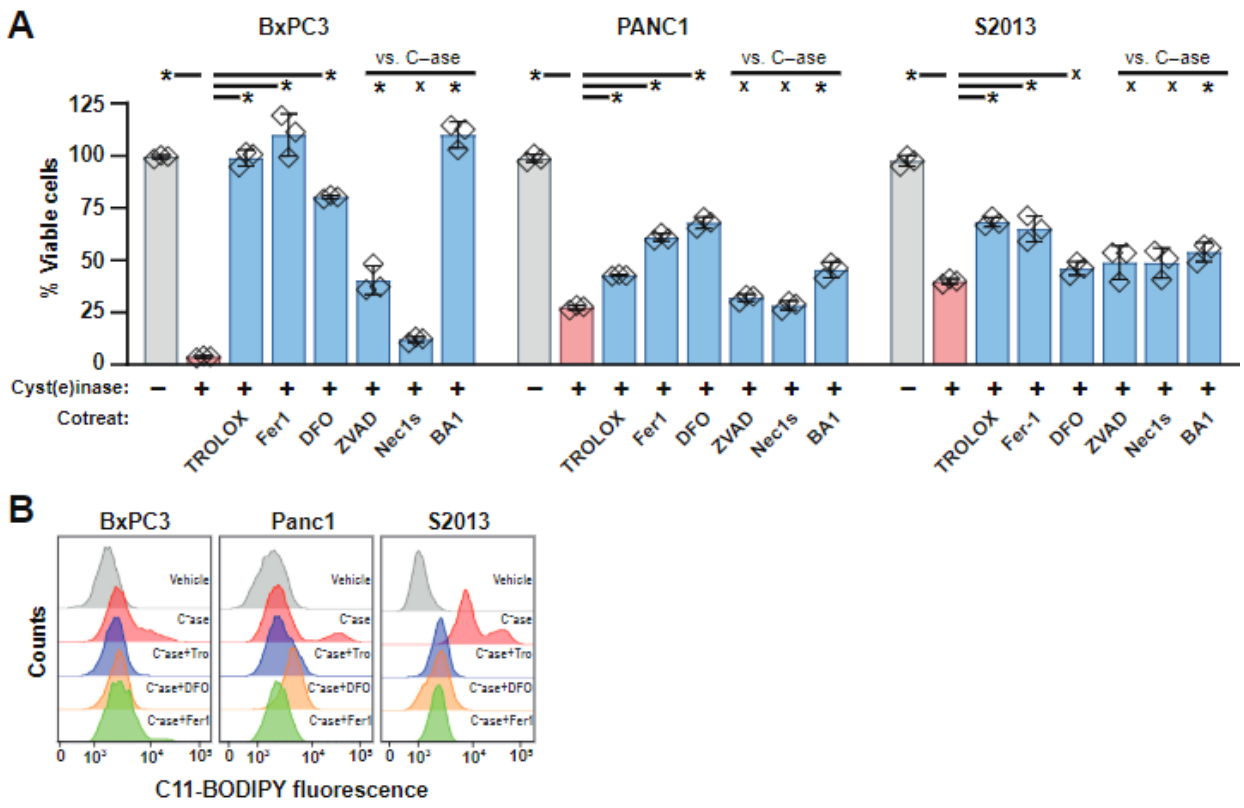

Figure 24. Cyst(e)inase in vitro studies.
(A) Viability of human PDAC cells treated with cyst(e)inase, alone or in combination with Trolox, Fer1, DFO, ZVAD-FMK, Necrostatin-1S, or Bafilomycin A (see Fig. 1C for details on compounds. Data are mean±SEM with n = 3 independent experiments. * $p < 0.05$ by Tukey's test. x = not significant. **(B)** C11-BODIPY fluorescence for human PDAC cells treated with cyst(e)inase alone or in combination with Trolox, DFO, or Fer-1.

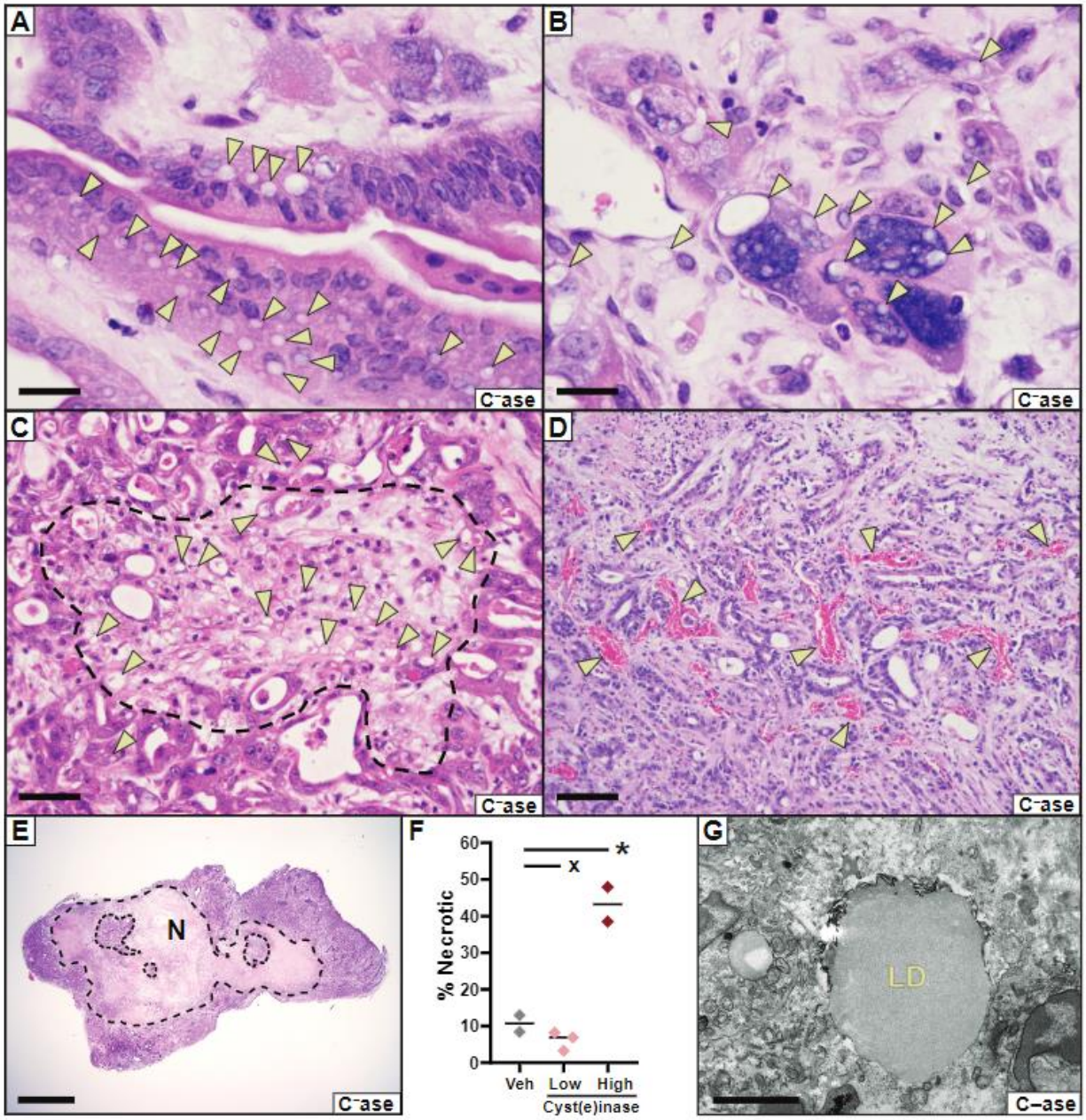

Figure 25. Histopathology of cyst(e)inase treated KPC pancreatic tumors.
(A-F) H&E stained microscopic images of pancreatic tumor tissues treated from KPC mice treated with cyst(e)inase. Arrowheads show lipid droplets. Images of well (A) and poorly (B) differentiated PDAC treated with cyst(e)inase and exhibiting lipid droplet formation. Bars = 20 µm. **(C)** Focal lesion (hashed line) exhibiting large numbers of lipid droplets. Bar = 50 µm. **(D)** In some cyst(e)inase tumors, decompressed blood vessels(arrows) were noted. Bar = 100 µm. **(E)** Regional necrosis (hashed line) of varying degrees was noted inall cyst(e)inase treated KPC tumors. (Bar = 2 mm). **(F)** Quantification of necrotic regions in various treatment samples. *p < 0.05 by unpaired Student's t-test. **(G)** TEM of KPC pancreatic tumor from cyst(e)inase treated mouse showing a larger lipid droplet (LD). Scale = 2 µm

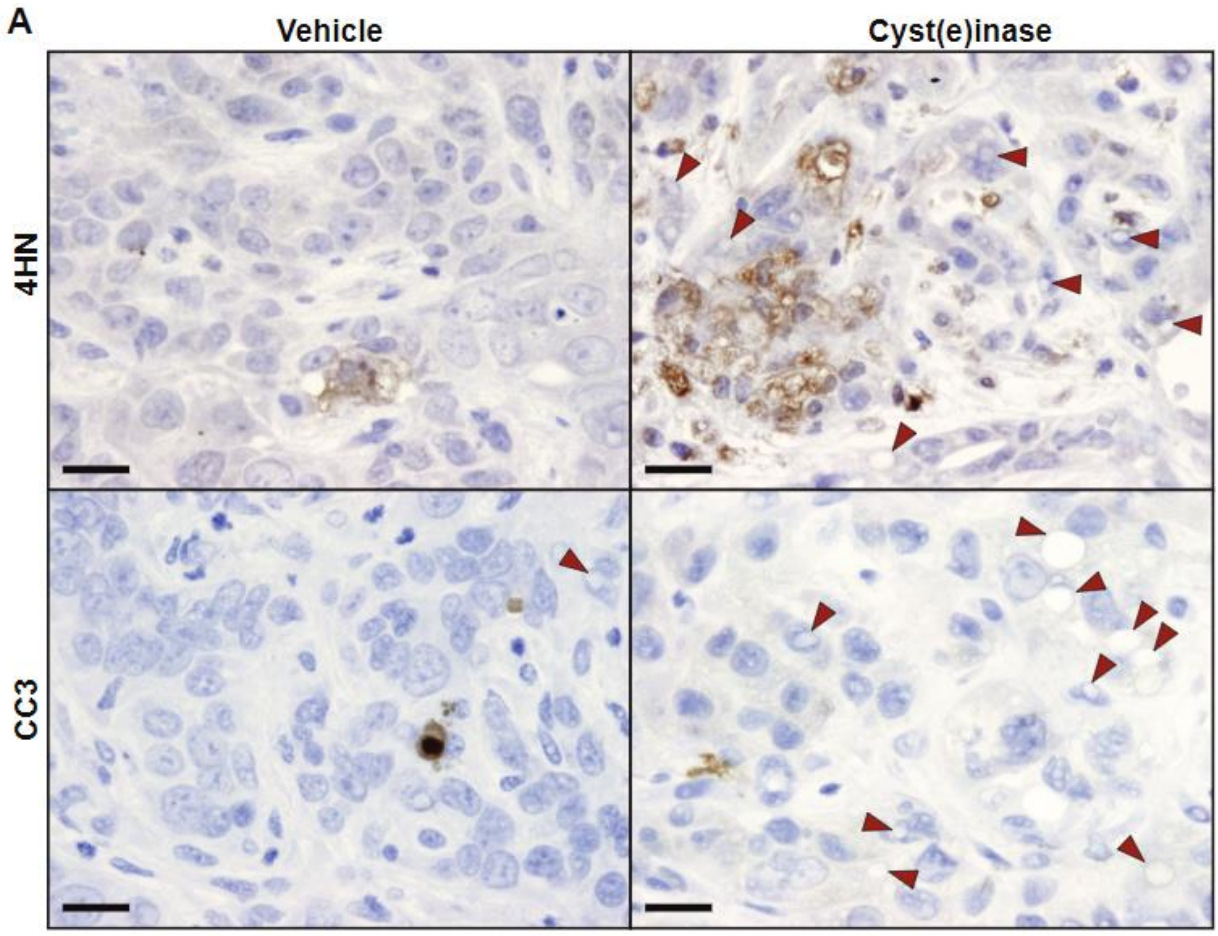

Figure 26. Response of KPC tumors to cyst(e)inase.
(A) Immunohistochemistry for 4-hydroxynonenal and cleaved caspase 3 from representative KPC pancreatic tumors treated with vehicle or cyst(e)inase in the 10-day short term response study. Red arrows indicate lipid droplets.

3.4 Discussion

In summary, our data add to a growing body of evidence showing that certain cancers, including PDAC, rely on cysteine metabolism to avert ferroptosis. Previously, *SLC7A11* deletion via CRISPR-Cas9 was shown to induce ferroptosis in cultured PDAC cells and slow xenograft engraftment and growth[18], and system x_C^- inhibition was shown to limit the growth of lymphoma xenografts, inducing a lipid oxidative signature and other indicators of ferroptosis[15]. However, cysteine depletion in a PDAC xenograft model had little effect on tumor growth, perhaps indicating that the nutrient-deprived, hypoxic microenvironment of autochthonous pancreatic tumors may contribute to the tumor-selective cysteine dependency we observed in genetically engineered mouse models of PDAC. Although it is not yet known whether human PDAC is also susceptible to ferroptosis from cysteine depletion, the clinical development of cyst(e)inase for treatment of the metabolic disorder cystinuria provides a pathway for future translation of this concept.

3.5 Materials and Methods

Cell culture

All cell lines were obtained from ATCC and tested negatively for mycoplasma infection. Cells were maintained under standard conditions at 37ºC and 5% CO2. Cells were grown in DMEM (Life Technologies, 12430-054) supplemented with penicillin and streptomycin (Corning, 30-003-CI), 10% FBS (Life Technologies, 10438-034), and MEM NEAA (Life Technologies,11140-050), unless otherwise indicated. For cystine starvation experiments, cells were cultured in DMEM lacking glutamine, methionine, and cystine (Life Technologies, 21013-024), supplemented with 200 mM methionine (Sigma, M9625), 4 mM glutamine (Life Technologies,25030-081), 10% FBS, penicillin and streptomycin, and varying concentrations of cystine (Sigma, C8755), depending on the given experiment. For cysteine starvation and IKE related cell viability experiments, cells were plated in a 96-well plate format. PANC-1 and S2-013 cells were plated at 4,000 cells per well; MIA PaCa-2, BxPC-3, and AsPC-1 cells were plated at 8000cells per well. Cells were allowed to seed overnight, and subsequently treated with compounds at indicated concentrations and for indicated lengths of time. Viability was

assessed using the Alama rBlue reagent (Thermofisher, 88952) according to the manufacturer's instructions. In brief,10 µL of Alamar Blue reagent was added each well containing 100 µL of experimental media .Plates were gently agitated for 1 minute to promote adequate mixing. Once wells had reached uniform color, plates were incubated at standard culture conditions indicated above for 1-4hours. Plates were subsequently assessed for fluorescent readout on a Promega plate reader using the green filter. For viability assays testing PANK inhibition and combinatorial BSO treatment, cells were plated in a 96-well plate format at 1000 cells per well, allowed to seed overnight, and then treated with compounds at indicated concentrations and for indicated lengths of time. These viability assays utilized the Cell-Titer-Glo 2.0 reagent (Promega, G9243) according to the manufacturer's instructions. Briefly, all wells from 96-well plates were aspirated followed by the addition of 100 µL of Cell-Titer-Glo 2.0 reagent to each experimental well. Plates were gently agitated for 10 minutes to promote adequate mixing. Luminescence was subsequently measured using a SpectraMax M3 plate reader.

For cyst(e)inase experiments, cells were plated in a 96-well plate format as follows: PANC-1 and S2-013 cells were plated at 2000 cells per well; MIA PaCa-2, BxPC-3, and AsPC-1 cells were plated at 3000 cells per well. Cells were allowed to grow overnight, and subsequently treated with the indicated compounds for the indicated length of time. After 48 hours of incubation, 10 µL of Alamar Blue reagent (Thermofisher, 88952) were added to each well containing 100 µL of experimental media. Plates were incubated at standard culture conditions for 4 hours before measuring fluorescent level on a Promega plate reader using the green filter.

Cell Culture Reagents

The following is a list of chemical compounds used in cell culture experiments: Trolox (Sigma, 238813), ZVAD-FMK (SelleckChem, S7023), Bafilomycin A1 (Sigma, B1793), Necrostatin-1s (BioVision, 2263-1), Ferrostatin-1 (Sigma, SML0583), N-acetyl-L-cysteine (Sigma, A9615), buthionine sulfoxamine (Sigma, B2515), deferoxamine (Sigma, D9533), GSH-ethyl ester (Sigma, G1404), staurosporine (Sigma, S4400), PE and IKE (provided by Brent Stockwell), CoA (Sigma, C3144). Specifically for the in vitro cyst(e)inase experiments the following compounds were used: Cyst(e)inase (provided

by Everett Stone and George Georgiou), Trolox (Sigma, 238813), ZVAD-FMK (SelleckChem, S7023), Bafilomycin A1 (Sigma, B1793), Necrostatin-1s (BioVision, 2263-1), Ferrostatin-1 (Sigma, SML0583), N-acetyl-L-cysteine (Sigma, A9615), deferoxamine (Sigma, D9533). 2

For PANKi and BSO combination studies, the following compounds were used: Pantothenate kinase inhibitor (Calbiochem, 537983), L-Buthionine-(S,R)-Sulfoximine (Cayman,14484), Imidazole ketone erastin (Medchem express, HY-114481), Ferrostatin-1 (Cayman, 17729), Trolox (Cayman, 10011659), Deferoxamine (Cayman, 14595), Coenzyme A (Cayman, 16147), Glutathione ethyl ester (Cayman, 14953), Palmitate (calcium salt) (Cayman, 10010279), Oleic Acid (Cayman, 90260), Linoleic Acid (Cayman, 90150), DMSO (Sigma, D2650), Ethanol (Decon labs, 2701), and Chloroform sterile filtered (Sigma, C2432).Compounds were formulated according to the manufacturer's instructions.

Light and Fluorescent Microscopy

Still transmitted light images were captured on an Olympus CKX41. Time lapse images and fluorescent microscopy still images were captured on a Nikon A1RMP. For time lapse videos, one image was captured every minute for up to 24 hours post treatment initiation. Cells were plated in a 6-well plate format, (PANC-1: 250,000 cells per well). For fluorescent ROS detection, cells were stained with C-11 BODIPY (Invitrogen, C10445) at a concentration of 2μM for 30 minutes prior to time lapse imaging. Cells were washed with PBS three times and incubated in Live-Cell Imaging Solution (Life Technologies, A14291DJ) during the duration of live-cell imaging. To detect lipid ROS at static time points by fluorescence microscopy, cells were plated in 1u-Slide 8 well ibiTreat dishes (ibidi, 80827). PANC-1 cells were plated at 30,000 cells per chamber. Cells were seeded overnight and subsequently subjected to indicated treatments for indicated times. Upon experiment completion, cells were visualized on a Nikon A1RMP in the red, green, and transmitted light channels. Images from all three channels were then overlaid to produce final images.

Flow Cytometric Detection of ROS

Cell lines were plated in quadruplicate at the cell numbers indicated previously for the 96-well plate format. Cells were allowed to seed overnight and were subjected to

various compound treatments for indicated times. Cells were then incubated for 30 minutes in live-cell imaging solution containing the pertinent ROS dye at the following concentrations: C-11 BODIPY, 2 μM; and H2DCFDA, 10 μM (Invitrogen, C6827). Cells were then washed with PBS, trypsinized with .25% trypsin (Life Technologies, 25200-056), and neutralized with 10% FBS in PBS at a 1:1 volume. Cells were strained through a 40μM strainer (BD Falcon, 08-771-1), and analyzed on a MACSQuant Analyzer 10, BD LSRII, or a BD Fortessa with high throughput attachment, depending on the application. A minimum of 4,000 cells were analyzed per condition. For both C-11 BODIPY and H2DCFDA, signal was analyzed in the FITC channel. Software analysis and histogram generation was carried out using FlowJo v10.

For flow cytometric detection of ROS upon cyst(e)inase treatment, cells were seeded in triplicates on 6-well plate format at the following density: 100,000 cells per well of PANC-1 and S2-013 cells; 250,000 cells per well of BxPC3 and AsPC-1. Cell were allowed to grow overnight before being treated with 90 nM cyst(e)inase treatment in the presence of the same rescuing agents and concentrations as described above for the cell viability assay. PANC-1, AsPC-1 cells were incubated in the presence of cyst(e)inase and agents for 24 hours; BxPC-3 and S2-013 for 48 hrs. 5μM IKE was added 6-8 hours before the end of the incubation time for each cell lines. After that cells were incubated for 30 minutes in live-cell imaging solution containing 2 μM C-11 BODIPY (Invitrogen). Cells were then washed with PBS, trypsinized with phenol red free 0.25% trypsin (Life Technologies, 25200-056), and neutralized with 10% FBS in PBS at a 1:1 volume. Cells were strained through a 40μM strainer (BD Falcon, 08-771-1), and analyzed a BD Fortessa. A minimum of 10,000 cells were analyzed per condition using FITC channel. Software analysis was carried out using FlowJo v10.

Cell-based Thermal Shift Assay

SKBR3 cells were seeded in 3 T-175 flasks, 10 million cells per flask, overnight, then treated with DMSO (vehicle), 20 μM PANKi, or 20 μM SGC-GAK-1 (Sigma, SML2202) for two hours, trypsinized, and washed with PBS. Cell pellets were resuspended with 230 μL of PBS + protease inhibitors (Roche) and split into ten 20 μL PCR tubes. Cells were heated to indicated temperatures for 3 minutes in two batches in a preheated thermocycler, then placed at room temperature for three minutes, then

snap frozen in liquid nitrogen. Samples were placed into the PCR machine only when it reached the desired temp, and heated for three minutes, followed by three minutes at room temperature. Cells were lysed via two freeze-thaw cycles of liquid nitrogen/25°C, vortexed, and then spun at 20,000 rpm for 20 min at 4°C. Supernatant was removed, sample buffer added, and samples boiled heated to 70°C for 10 min, and then loaded for gel electrophoresis at 200V for 45min. Western blotting for PANK1 was performed according to standard protocols.

Mass Spectrometry-Based Metabolomics

Unlabeled targeted metabolomics (For IKE and PANK inhibitor PD markers) Cells were plated at 0.5 million cells per well in 6-well plates and treated with the indicated conditions. Following treatment, the medium was aspirated and cells were lysed using dry-ice cold 80% methanol and extracts were incubated in -80ºC for 10 min and centrifuged at 14,000 rpm for 10 min at 4°C. Protein concentration was determined by processing a parallel 6-well plate at equivalent cell density and used to normalize metabolite fractions across samples. Aliquots of the supernatants were then transferred to a fresh microcentrifuge tube and dried. Metabolite extracts were then re-suspended in 35 µl 50:50 MeOH: H2O mixture for LC–MS analysis. LC-MS analysis was performed using an Agilent Technologies Triple Quad 6470 system ran in negative ion acquisition modes. dMRM transitions and other parameters for each compound were determined empirically utilizing analytical standards. Separations were conducted utilizing an Agilent ZORBAX RRHD Extend-C18 column, 2.1 × 150 mm, 1.8 µm and ZORBAX Extend Fast Guards. LC gradient profile is: at 0.25 ml/min, 0- 2.5 min, 100% A; 7.5 min, 80% A and 20% C; 13 min 55% A and 45% C; 20 min, 1% A and 99% C; 24 min, 1% A and 99% C; 24.05 min, 1% A and 99% D; 27 min, 1% A and 99% D; at 0.8 ml/min, 27.5-31.35 min, 1% A and 99% D; at 0.6 ml/min, 31.50 min, 1% A and 99% D; at 0.4 ml/min, 32.25-39.9 min, 100% A; at 0.25 ml/min, 40 min, 100% A. Column temp is kept at 35℃, samples are at 4℃, and injection volume is 2 µL.Mobile phase (A) consists of 97% water and 3% methanol 15 mM acetic acid and 10 mM tributylamine at pH of 5. (C) consists of 15 mM acetic acid and 10 mM tributylamine in methanol. Washing Solvent (D) is acetonitrile. LC system seal washing solvent 90% water and 10% isopropanol, needle wash solvent 75% methanol, 25% water.Key mass

spectrometry parameters utilized were: Gas temp 150 ℃, Gas flow 10 l/min, Nebulizer 45 psi, Sheath gas temp 325 ℃, Sheath gas flow 12 L/min, Capillary -2000 V, Delta EMV -200 V. Dynamic MRM scan type is used with 0.07 min peak width, acquisition time is 24 min. Delta retention time of plus and minus 1 min, fragmentor of 40 eV and cell accelerator of 5 eV are incorporated in the method.

Metabolomics Data Analysis (For IKE and PANK inhibitor pharmacodynamic markers)

Raw data were pre-processed with Agilent MassHunter Workstation Software Quantitative QqQ Analysis Software (B.07.00). Metabolite counts were then normalized by the total intensity of all metabolites to reflect equal sample loading. Finally, each metabolite abundance in each sample was divided by the median of all abundance levels across all samples for proper comparisons, statistical analyses, and visualizations among metabolites.

Remaining Metabolomics Data Acquisition and AnalysisFor steady state, an Agilent 1290 UHPLC-6490 Triple Quandruple MS system as above was used. For negative ion acquisition, a Waters Acquity UPLC BEH amide column (2.1 x 100mm, 1.7μm) column with the mobile phase (A) consisted of 20 mM ammonium acetate, pH 9.6 in water, and mobile phase (B) was used. Gradient program: mobile phase (B) was held at 85% for 1 min, increased to 65% in 12 min, then to 40% in 15 min and held for 5 min before going to initial condition and held for 10 min. For positive ion acquisition, a Waters Acquity UPLC BEH TSS C18 column (2.1 x 100mm, 1.7μm) column was used with mobile phase A) consisting of 0.5 mM NH4F and 0.1% formic acid in water; mobile phase (B) consisting of 0.1% formic acid in acetonitrile. Gradient program: mobile phase (B) was held at 1% for 1.5 min, increased to 80% in 15 min, then to 99% in 17 min and held for 2 min before going to initial condition and held for 10 min. The column was kept at 40 ℃ and 3 μl of sample was injected into the LC-MS/MS with a flow rate of 0.2 ml/min. Tuning and calibration of QqQ MS was achieved through Agilent ESI-Low Concentration Tuning Mix.Optimization was performed on the 6490 QqQ in negative or positive mode individually for each of 220 standard compounds to get the best fragment ion and other MS parameters for each standard. Retention time for each standard of the 220 standards was measured from pure standard solution or a mix standard solution. The LC-MS/MS method was created with dynamic dMRMs with RTs,

RT windows and MRMs of all the 220 standard compounds. In both acquisition modes, key parameters of AJS ESI were: Gas temp 275 ℃, Gas Flow 14 l/min, Nebulizer at 20 psi, Sheath Gas Heater 250℃, Sheath Gas Flow 11 L/min, Capillary 3000 V. For negative mode MS: Delta EMV was 350 V, Cycle Time 500 ms and Cell accelerator voltage was 4 V, whereas for positive acquisition mode MS: Delta EMV was set at 200 V with no change in cycle time and cell accelerator voltage.The QqQ data pre-processed with Agilent MassHunter Workstation Software Quantitative QqQ Analysis Software (B0700). Additional analyses were post-processed for further quality control in the programming language R. We calculated coefficient of variation (CV) across replicate samples for each metabolite given a cut-off value of peak areas in both the positive and the negative modes. We then compared distributions of CVs for the whole dataset for a set of peak area cut-off values of 0, 1000, 5000, 10000, 15000, 20000, 25000 and 30000 in each mode. A noise cut-off value of peak areas in each mode was chosen by manual inspection of the CV distributions. Each sample is then normalized by the total intensity of all metabolites to reflect the same protein content as a normalization factor. We then retained only those metabolites with at least 2 replicate measurements. The remaining missing value in each condition for each metabolite was filled with the mean value of the other replicate measurements. Finally, each metabolite abundance level in each sample was divided by the median of all abundance levels across all samples for proper comparisons, statistical analyses, and visualizations among metabolites. The statistical significance test was done by a two-tailed t- test with a significance threshold level of 0.05. The p-values were not adjusted in favor of more flexible biological interpretation. For the 13C–cystine/methionine label incorporation studies, an Agilent 1260 UHPLC combined with a 6520 Accurate-Mass Q-TOF LC/MS was utilized. Agilent Mass Hunter Workstation Software LC/MS Data Acquisition for 6200 series TOF/6500 series QTOF (B.06.01) was used for calibration and data acquisition. A Waters Acquity UPLC BEH amide column (2.1 x 100mm, 1.7µm) column was used with mobile phase (A) consisting of 20 mM NH4OAc in water pH 9.6, and mobile phase (B) consisting of ACN. Gradient program: mobile phase (B) was held at 85% for 1 min, increased to 65% in 12 min, then to 40% in 15 min and held for 5 min before going to initial condition and held for 10 min. The column was at 40℃ and 3 µl of

sample was injected into the LC-MS with a flow rate of 0.2 ml/min. Calibration of TOF MS was achieved through Agilent ESI-Low Concentration Tuning Mix. Key parameters for both acquisition modes were: mass range 100-1200 da, Gas temp 5

350 ℃ , Fragmentor 150 V, Skimmer 65 v, Drying Gas 10 L/min, Nebulizer at 20 psi and Vcap 3500 V, Ref Nebulizer at 20 psi. For negative mode the reference ions were at 119.0363 and 980.01637 m/z whereas for positive acquisition mode, reference ions at 121.050873 and 959.9657 m/zFor 13C- labeling data analysis, we used Agilent MassHunter Workstation Software Profinder B.08.00 with Batch Targeted Feature Extraction and Batch Isotopologue Extraction and Qualitative Analysis B.07.00. Various parameter combinations, e.g. mass and RT tolerance, were used to find best peaks and signals by manual inspection. Key parameters were: mass tolerance = 20 or 10 ppm and RT tolerance = 1 or 0.5 min. Isotopologue ion thresholds, the anchor ion height threshold was set to 250 counts and the threshold of the sum of ion heights to 500 counts. Coelution correlation threshold was set to 0.3.All other bioinformatics analyses including graphs and plots were done using R/Bioconductor.

Laser Capture Microdissection and RNA Sequencing

Cryosections of OCT–embedded tissue blocks from KPFSR mice treated with corn oil and tamoxifen, respectively, were transferred to PEN membrane glass slides and stained with cresyl violet acetate. Adjacent sections were H&E stained for pathology review. Laser capture microdissection was performed on a PALM MicroBeam microscope (Zeiss), collecting at least 10000 cells per sample. Total RNA was extracted using the RNeasy Micro Kit (Qiagen) and amplified using the Clontech SMART-seq v4 Ultra Low Input RNA Kit to create cDNA. Next, the Illumina Nextera XT kit was used to prepare libraries which were then sequenced to a depth of 30 million, 100bp, single-end reads on the Illumina HiSeq4000 platform. Reads were mapped to the UCSC mm10 reference genome and quantified per gene, respectively, using the STAR (v 2.5.2b) and feature Counts (v 1.5.0-p3) software.

Ferroptosis Signature Bioinformatics Analyses

First, gene expression data were retrieved from the supplement of Dixon et al. (3) as FPKM per gene. Differential gene expression (DEG) analysis was carried out between samples treated with DMSO and erastin, respectively, after log2 transformation

using the limma R package. Genes significantly upregulated upon erastin treatment at an FDR <= 0.05 (n = 45) represented the in vitro ferroptosis signature. Next, DEG analysis was carried out between LCM-RNA-Seq samples retrieved from epithelia of KPFSR tumors whose animals had been treated with corn oil and tamoxifen, respectively, using the DESeq2 R(20) with raw counts as input. Genes significantly upregulated upon tamoxifen treatment at an FDR <= 0.005 (n = 44) represented the in vivo ferroptosis signature. Gene set enrichment of the aforementioned signatures on the entire in vitro and in vivo differential gene expression signature, respectively, was carried out as described previously.

Microarray Data

Gene expression data from studies comparing pancreatic ductal adenocarcinoma specimen with normal pancreas parenchyma were downloaded from the Gene Expression Omnibus (GEO) using the GEOquery R package and the following accession numbers: GSE32676, GSE19650, GSE16515, GSE62452 and GSE71729. U133A-CEL files from were obtained from Array Express under accession number E-MEXP-950 and normalized using GCRMA. The following samples were excluded because of outlier behavior during exploratory data analysis: NPD15, T55, TPK9, NPK13. For all studies, probes were collapsed at the gene level using their mean normalized expression.

TCGA Data

RNA-Seq V2 expression, clinical and mutation data were downloaded for all available TCGA tumor types using the RTCGAToolbox R package. The run date was set to “2016-601-28”.

ICGC PDA expression data

RNA-Seq expression data and clinical annotation for 96 cases were retrieved from the supplementary data of Bailey et al. Illumina HumanHT-12 v4.0 microarray expression data were downloaded from the ICGC data portal for 269 cases. Only those cases were retained for further analyses that were annotated in Bailey et al. and did not have an RNA-Seq expression profile, leaving 142 unique cases. Differential gene expression analysis Genome-wide differential gene expression analysis normal tissue of origin and tumor tissue were calculated using the limma R package using (gc)rma-

normalized expression data for microarray studies and log2-transformed normalized count data for the TCGA cohorts. If normal and tumor samples were matched, i.e. from the same patient, a paired design was specified in the design formula.

Differential Gene Expression Analysis

Genome-wide differential gene expression analysis normal tissue of origin and tumor tissue were calculated using the limma R package using (gc)rma-normalized expression data for microarray studies and log2-transformed normalized count data for the TCGA cohorts. If normal and tumor samples were matched, i.e. from the same patient, a paired design was specified in the design formula.

Gene Set Enrichment Analysis

In order to examine the relationship of pathway activity and SLC7A11expression, we used the R implementation of single sample Gene Set Enrichment analysis: GSVA (gene set variation analysis) with default parameters after pre-filtering each expression matrix for genes with an interquartile range > 0.5. PDA tumors from the following cohorts were examined: TCGA, ICGC RNA-Seq, ICGC microarray, NIH, UNC and Collisson their enrichment score per sample was calculated for the following gene sets from the MSigDB (v.6.0): HALLMARK_REACTIVE_OXIGEN_SPECIES, SINGH_NFELE2_TARGETS and GO_CELL_REDOX_HOMEOSTASIS.

Effect Size Meta-Analysis for SLC7a11 Expression Data

Log2 fold change

The effect size (i.e. log2 fold change) and its standard error for SLC7A11were extracted from the respective genome-wide differential expression analysis of 6 studies where global expression in normal pancreatic tissue was compared to PDA.

Pearson Correlation

Pearson correlation and its standard error were calculated for each study and gene set, respectively, between the gene set enrichment scores per sample and the median-centered SLC7A11expression per sample using the cor.test function from the stats R package. Meta-analysis for each metric was carried out using the metafor R package. Both random and fixed effect models were fit using the rma function (method = “REML” and method = “FE”, respectively). Survival analysisThe association of SLC7A11 expression status with disease outcome was evaluated using a log-rank test

as implemented in the survdiff function from the survival R package. Patients were grouped into tertiles according to normalized SLC7A11expression and differences in outcome were assessed between the upper and lower tertile.

Animal Breeding and Genotyping

All studies were carried out in accordance with the relevant institutional guidelines of Columbia University. All procedures were approved by the Columbia University Institutional Animal Care and Use Committee (IACUC) and were conducted in keeping with the NIH “Guide for the Care and Use of Laboratory Animals.”

Generation of Pdx1-FlpO Mice

The proximal 6kb promoter of the Pdx1-Cre transgene (38) was fused to the start codon of mammalian codon-optimized, thermostable Flp recombinase (FlpO), with subsequent fusion of the 5’ end of the FlpO open reading frame to the hGH polyadenylation signal sequence using the In-Fusion cloning system (Clontech) according to the manufacturer’s instructions. The Pdx1-FlpO cassette was excised from a large-scale plasmid preparation, gel-purified, and microinjected into the pronuclei of fertilized FVB oocytes at the Gladstone Transgenic Mouse Core. Following implantation, birth, and weaning, transgene-bearing founder mice were identified via PCR and maintained on an FVB background.Pdx1-FlpO founders were crossed to homozygous FVB alkaline phosphatase Flp reporter mice (gift, Dr. Susan Dymecki, Harvard University), Pdx1-FlpO-harboring progeny sacrificed at 2 months of age, and skin, brain, liver, pancreas, kidney, lung, stomach, duodenum, small intestine, colon collected and flash frozen in liquid nitrogen. Frozen sections of each were cut, alkaline phosphatase histochemistry performed (Vector Laboratories), and sections examined microscopically. Founder lines exhibiting prominent alkaline phosphatase activity in the pancreas were backcrossed an additional five generations and this process was repeated to identify founder lines exhibiting stable transgene expression.

Generation of Slc7a11 Conditional Knockout Mice

Mice bearing an Slc7a11 conditional null allele (EMMA ID: 10001, strain designation Slc7a11tm1a(EUCOMM)Wtsi, referred to here as Slc7a11Fl) were imported from the IMPC repository. These mice were crossed to homozygous ACTB: FLPe mice (Jackson Laboratory, Stock no. 003800) to create Slc7a11conditional mice in which

loxP sites surround exon three of the Slc7a11gene. Using a combination of the Pdx1-Flpo, KRASFSFG12D (Jackson Laboratory, Stock no. 008653), p53R172H (Jackson Laboratory, Stock no. 008652, modified by crossing to Cre-deleter strain), Rosa26CreERT2 (Jackson Laboratory, Stock no. 008463), and our newly made Slc7a11Fl/Fl mice, we were able to generate a new strain of genetically engineered mouse model akin to the KRASLSL-G12D/+;p53LSL-R172H;Pdx1-Cre (KPC) mouse, but in which we have temporal control of the deletion of Slc7a11 using tamoxifen. We term these mice KRASFSF-G12D/+; p53R172H; Pdx1-Flpotg/+; Slc7a11Fl/Fl; Rosa26CreERT2/+, KPFSR mice.

Genotyping

Genotyping was carried out using protocols provided by Jackson Laboratory for all strains obtained from this vendor. Slc7a11Fl/Fl genotyping was carried out as follows:Forward primer: 5'-tgggttggtctctggtgatc-3'; Reverse primer: 5'-cctgtgaagatccgcctact-3' Cycling conditions: 1. 94ºC 3 minutes; 2. 94ºC 1 minute; 3. 60ºC 2 minutes; 4. 72ºC 1 minute; Cycle to step 2, 29 times.; 5. 72ºC 5 minutes; 6. 4ºC forever. Expected amplicons: Slc7a11Fl/Flmice: 386 bp; WT mice: no amplicon. RecombinatorialSlc7a11genotyping was custom designed as follows: Forward primer: 5'-tgg gtt ggt ctc tgg tga tc-3'; Reverse primer: 5'-ctt aac ccc agc acc att cg-3' Cycling conditions: 1. 95ºC 2 min; 2. 95ºC 1 min; 3. 56ºC 30 seconds; 4. 72ºC 1 min; Cycle to step 2, 34 times; 5. 72ºC 5 min; 6. 4ºC forever. Expected amplicons: Slc7a11Fl/Fl unrecombined = 1285 bp; Slc7a11Fl/Fl recombined = 450 bp; WT mouse = 1240 bp.

Western Blot

Western blot for Slc7a11 was carried out using standard protocols. Tumor samples were ground and lysed in Flag lysis buffer, and proteins were quantified with Bradford assay. Proteins were run on an SDS PAGE gel under denaturing conditions, transferred to a membrane, and probed with primary antibody (Cell Signaling, s12691) overnight at 4ºC. Blot was probed with an appropriate secondary and developed using a standard ECL kit.

KPFSR Survival Study

At approximately 42 days of age, KPSFR mice were treated with cerulein (Sigma, C9026) at 250 µg/kg by intraperitoneal injection for 5 consecutive days to induce

chronic pancreatitis and accelerate tumor formation, as per previous reports. Tumor formation was monitored initially by once weekly palpation and upon positive palpation, by twice-weekly ultrasound. Once the average diameter of tumors of the pancreas was 4-7 mm in size, mice were randomly enrolled into the survival study. Mice were treated with either corn oil (Sigma, C8267) or tamoxifen (Sigma, T5648) at 200 mg/kg by oral gavage for 6 consecutive days. Afterward the initial survival study, a small cohort of mice was enrolled on a tamoxifen and NAC combination treatment. These mice were administered tamoxifen in the aforementioned fashion and administered NAC in their drinking water at 1 g/L. Subsequently, small cohorts of KPC mice were enrolled on a NAC only treatment arm, as controls. For the vehicle arm data, we used historical controls from the same colony of mice that were treated with saline. Mice were euthanized once they reached endpoint criteria consisting of a combined physical and behavioral metric designed in consultation with Columbia IACUC. Tumor samples were either fixed in formalin overnight at 4ºC, fixed in PFA at 4ºC overnight followed by sucrose-mediated water displacement for 24 hours at 4ºC, frozen in OCT, or flash frozen in liquid nitrogen.

***In vivo* Cyst(e)inase Studies**

The short-term histology study involved treatment with vehicle or a high dose (100 mg/kg, every two days by intraperitoneal injection) or a low dose (50 mg/kg, every three days by intraperitoneal injection) of cyst(e)inase for 10 days (n = 2 animals per group, one low dose animal presented with two independent tumors). Animals were then euthanized and tumors were acquired for histological analyses (necrosis quantification, other IHC, and TEM). Thetumor growth study was carried out in n = 4 KPC mice treated with high dose cyst(e)inase (see above). Tumors were allowed to reach enrollment criteria (4-7mm diameter) and then treated with drug. Tumor volumes were monitored by 3d ultrasound until animals reached endpoint criteria (morbidity).

Ultrasound

Tumor ultrasonography and volume quantification was carried out as previously described.

Pathology and Immunohistochemistry

Samples that had been fixed in formalin were washed in 70% ethanol and subjected to standard dehydration processing to prepare them for mounting in paraffin wax blocks. Paraffin blocks were sectioned on a Leica RM 2235 at 5 µM thickness. The sections were mounted on charged slides and heated to 60ºC to melt wax and ensure tissue adherence to the slide. Slides were then subjected to standard rehydration and antigen retrieval was carried out for five minutes in boiling 10 mM sodium citrate buffer pH 6, .05% Tween-20 using a pressure cooker. Slides were brought to room temperature in an ice-cold water bath. Slides were then incubated in 3% hydrogen peroxide for 20 minutes at room temperature to block endogenous peroxidases. Slides were blocked in 1.5% horse serum and 2% animal free blocker (Vector Laboratories, SP-5030) for 1 hour at room temperature. Slides were then stained with the appropriate antibody: Cleaved caspase-3 (Cell Signaling, 9664S), 1:1000 dilution; Ki67 (Cell Signaling, 12202S), 1:100 dilution; phosphohistone-H3 (Cell Signaling, 9701S), 1:200 dilution; 4-hydroxynonenal (Abcam, 46545), 1:200. Primary antibody incubation was carried out overnight at 4ºC. Slides were then washed 3x with PBS-T and incubated with the appropriate secondary antibody for 30 minutes at room temperature. Staining was developed using the DAB reagent (Vector Labs, VV-93951085). Quantification for CC3, Ki67, and pHH3 was done in a blinded fashion, counting 9 positive cells per 40x field for 10 fields per sample. Quantification for 4HN staining was done by first deconvolving hematoxylin and DAB staining using Fiji. The DAB image component was then adjusted for a threshold of 175 to identify positive staining. Finally, Fiji was used to analyze particle number using a circularity of 0-1 and a size above 200 pixels, yielding a total particle count per low powered (1.25X) field per sample.Histological staining on paraffin sections (hematoxylin and eosin, Oil Red O) were carried out using standard protocols. Following digital capture on Olympus BX51, histology images were processed using Affinity Photo software, using three filters/adjustments applied evenly across the entire image: unsharp mask, white balance, and levels adjustment.

Transmission Electron Microscopy

Tissues were fixed in a solution of 2% paraformaldehyde, 2.5% glutaraldehyde, and 2mM CaCl2 in 0.15 M sodium cacodylate buffer (pH 7.4) for 2 hours at room

temperature. They were then post-fixed in 1% osmium tetroxide for 40 minutes and 1.5% potassium ferricyanide in sodium cacodylate buffer for 1 hour at room temperature in the dark. Tissues were stained en bloc in 1% aqueous uranyl acetate (4℃ in the dark) for 1 hour, dehydrated in a series of graded acetones, and embedded in Eponate12 resin (Ted Pella). Ultra-thin sections (70 nm) were obtained using a diamond knife (Diatome) in an ultramicrotome (Leica EM UC7) and placed on copper grids (300 mesh). Sections were imaged on a Zeiss Libra 120 TEM operated at 120 kV using Zeemasacquisition system with 2K of resolution.

Statistical Analyses

All statistical analyses, unless otherwise indicated, were performed using GraphPad Prism. Tukey's test was performed as a post-hoc test after one-way ANOVA, comparing all pairwise permutations, with alpha = 0.05. Only relevant pairwise comparisons are highlighted in the figures. Student's t-test was performed when indicated in the manuscript, for comparing two experimental conditions. The paired t-test was used when data was in the form of matched pairs. All t-tests were two tailed and set with a significance threshold of $p < 0.05$.10

3.6 Chapter 3 References

1. DeNicola, G. M. et al. Oncogene-induced Nrf2 transcription promotes ROS detoxification and tumorigenesis. Nature 475, 106–109 (2011).

2. Sato, H. et al. Redox Imbalance in Cystine/Glutamate Transporter-deficient Mice. J. Biol. Chem. 280, 37423–37429 (2005).

3. Yang, W. S. et al. Regulation of ferroptotic cancer cell death by GPX4. Cell 156, 317–331 (2014).

4. Dixon, S. J. et al. Ferroptosis: An Iron-Dependent Form of Nonapoptotic Cell Death. Cell 149, 1060–1072 (2012).

5. Gao, M. et al. Ferroptosis is an autophagic cell death process. Cell Res. 26, 1021–1032 (2016).
6. Friedmann Angeli, J. P. et al. Inactivation of the ferroptosis regulator Gpx4 triggers acute renal failure in mice. Nature Cell Biology 16, 1180–1191 (2014).

7. Hingorani, S. R. et al. Trp53R172H and KrasG12D cooperate to promote chromosomal instability and widely metastatic pancreatic ductal adenocarcinoma in mice. Cancer Cell 7, 469–483 (2005).

8. Sastra, S. A. & Olive, K. P. Quantification of murine pancreatic tumors by high-resolution ultrasound. Methods Mol. Biol. 980, 249–266 (2013).

9. Gao, M. et al. Role of Mitochondria in Ferroptosis. Mol. Cell 73, 354-363.e3 (2019).

10. Dixon, S. J. et al. Pharmacological inhibition of cystine-glutamate exchange induces endoplasmic reticulum stress and ferroptosis. Elife 3, e02523 (2014).

11. Harris, I. S. et al. Deubiquitinases Maintain Protein Homeostasis and Survival of Cancer Cells upon Glutathione Depletion. Cell Metabolism 29, 1166-1181.e6 (2019).

12. Shimada, K. et al. Global survey of cell death mechanisms reveals metabolic regulation of ferroptosis. Nat. Chem. Biol. 12, 497–503 (2016).

13. Leu, J. I.-J., Murphy, M. E. & George, D. L. Mechanistic basis for impaired ferroptosis in cells expressing the African-centric S47 variant of p53. PNAS 116, 8390–8396 (2019).

14. Srinivasan, B. et al. Extracellular 4’-phosphopantetheine is a source for intracellular coenzyme A synthesis. Nat. Chem. Biol. 11, 784–792 (2015).

15. Zhang, Y. et al. Imidazole Ketone Erastin Induces Ferroptosis and Slows Tumor Growth in a Mouse Lymphoma Model. Cell Chem Biol 26, 623-633.e9 (2019).

16. Olive, K. P. et al. Inhibition of Hedgehog Signaling Enhances Delivery of Chemotherapy in a Mouse Model of Pancreatic Cancer. Science 324, 1457–1461 (2009).

17. Cramer, S. L. et al. Systemic depletion of L-cyst(e)ine with cyst(e)inase increases reactive oxygen species and suppresses tumor growth. Nat. Med. 23, 120–127 (2017).

18. Daher, B. et al. Genetic Ablation of the Cystine Transporter xCT in PDAC Cells Inhibits mTORC1, Growth, Survival, and Tumor Formation via Nutrient and Oxidative Stresses. Cancer Res 79, 3877–3890 (2019).

Chapter 4. GOT1 Inhibition Primes Pancreatic Cancer Cells for Ferroptosis through Labile Iron Release[3]

4.1 Abstract

Cancers have unique metabolic adaptations in response to cell-intrinsic and environmental stressors, where identifying new strategies to target these adaptions is an area of active research. We previously described a dependency on a cytosolic aspartate aminotransaminase (GOT1)-dependent pathway for NADPH generation in pancreatic cancer. Here, we sought to identify metabolic dependencies following GOT1 inhibition to provide insight into the regulation of redox metabolism. Using pharmacological methods, we identified cysteine, glutathione, and lipid antioxidant function as metabolic vulnerabilities following GOT1 withdrawal. Targeting any of these pathways triggered ferroptosis, an oxidative, non-apoptotic, iron-dependent form of cell death in GOT1 knockdown cells. Mechanistically, GOT1 inhibition promoted a catabolic state and enhanced the availability of labile iron through autophagy and iron uptake. Overall, our study identifies a novel biochemical connection between GOT1, iron regulation, and ferroptosis.

[3] The Contents of this chapter were adapted and reproduced from a first authored article in revision for consideration at *Nature Chemical Biology*: **Kremer, D. M.** et al. bioRxiv 2020.02.28.970228 (2020) doi:10.1101/2020.02.28.970228.

4.2 Introduction

Pancreatic ductal adenocarcinoma (PDA) cells exhibit extensive metabolic reprogramming to support survival and growth under metabolically harsh conditions[1,2] Our previous work demonstrated that PDA rewire the malate-aspartate shuttle to generate reduced nicotinamide adenine dinucleotide phosphate (NADPH), a major currency for biosynthesis and redox balance **(Figure 27a)**[3]. The canonical function of the malate-aspartate shuttle is to transfer reducing equivalents in the form of NADH from the cytosol into the mitochondria to facilitate oxidative phosphorylation (OxPHOS).

In PDA, we found the mitochondrial aspartate aminotransaminase (GOT2) is the primary anaplerotic source for alpha-ketoglutarate (αKG) and generates aspartate. Aspartate is then transferred to the cytosol and transaminated to produce oxaloacetate (OAA) by the cytosolic aspartate aminotransaminase (GOT1). OAA is reduced to malate by cytosolic Malate Dehydrogenase (MDH1) and is then oxidized by Malic Enzyme 1 (ME1) to generate NADPH, which is utilized to support redox balance and proliferation in PDA[3]. Furthermore, we demonstrated that this non-canonical pathway was orchestrated by mutant KRAS, the signature oncogenic driver of PDA. Thus, in an effort to target this rewired metabolic pathway and to understand its biological role with greater depth, we have placed our focus on GOT1. We and others recently identified scaffolds that may serve as leads in the development more potent GOT1 inhibitors[4–7].

Here, we analyzed GOT1 dependence across a large panel of PDA cell lines and specimens. We show that GOT1 sensitivity varies among the cultures in this panel, is dispensable in non-transformed human lines, and that GOT1 inhibition stunted growth in tumor models. GOT1 inhibition blocked progression through the cell cycle, leading to cytostasis, in GOT1-dependent cells. Thus, we then sought to characterize metabolic dependencies following GOT1 withdrawal that could be exploited to selectively kill PDA[8]. Examination of a targeted metabolic inhibitor library in GOT1 knockdown cells led to the discovery that exogenous cystine was essential for viability following chronic GOT1 suppression. Cystine is used for reduced glutathione (GSH) biosynthesis, which mediates protection against lipid oxidation. GOT1 knockdown in combination with inhibitors of glutathione synthesis or lipid antioxidant machinery led to cell death.

We characterized this as ferroptosis: an oxidative, non-apoptotic, and iron-dependent form of cell death[9,10]. We then determined that GOT1 withdrawal promoted a catabolic cell state resulting in labile iron release through autophagy, ferritinophagy, and iron uptake[11–13]. Overall, our study demonstrates that GOT1 inhibition promotes ferroptosis sensitivity by promoting labile iron and illustrates how GOT1 and labile iron influences ferroptosis susceptibility.

4.3 Results

PDAs Require GOT1 for Growth and Proliferation

To examine GOT1 dependence in a large panel of PDA cell lines and primary specimens with temporal control, we developed doxycycline (dox)-inducible short hairpin (sh)RNA reagents (iDox-sh) that target the coding and 3'UTR regions of GOT1 (sh1 and sh3), or scramble (shNT). shRNA activity was examined phenotypically by assessing colony formation and protein levels following dox treatment **(Figures 27b-c and 28a-b)**. We also measured aspartate levels as a biochemical readout for GOT1 inhibition **(Figure 28c)**. We then used these iDox-shRNA constructs to examine GOT1 sensitivity across a large panel of PDA lines and primary specimens (indicated with the UM# designation)[14] **(Figure 27d)**. GOT1 knockdown significantly impaired colony formation in 12 of 18 cell lines in the panel **(Figure 27d)**. The response to GOT1 knockdown did not depend on the expression status of malate-aspartate shuttle enzymes **(Figure 28d)**, and could arise from differences in glutamine flux. Indeed, in PL45, Capan-1, and Pa-Tu-8902 colony formation was severely diminished following GOT1 knockdown with both hairpins, and this was independent of dox-effects **(Figure 27d and 28a-b)**. Thus, a majority of PDA cell lines respond to GOT1 inhibition.

To test the specificity of GOT1 against PDA, we extended our cell panel to non-transformed human lines. We found human pancreatic stellate cells (hPSC), human lung fibroblasts (IMR-90), and human non-transformed pancreatic exocrine cells (hPNE) were minimally affected upon GOT1 knockdown, in agreement with previous results, suggesting that this pathway may be dispensable in non-transformed cells **(Figures 28e-f)**[3,6]. Together, these data demonstrate many PDA cell lines require GOT1 for

growth while non-transformed cell lines do not, highlighting a potential therapeutic window.

We then examined the effect of GOT1 inhibition on established PDA tumors. PDA cells were implanted subcutaneously into the flanks or orthotopically into the pancreas of immunocompromised mice and allowed to establish for 7 days prior to GOT1 inhibition. GOT1 sensitive cell lines exhibited profound growth inhibition upon induction of GOT1 knockdown with dox **(Figures 27e-f)**, results that were consistent with previous studies[3,15]. Parallel studies with shNT tumors indicated that the effect was independent of dox exposure **(Figure 29a)**. GOT1 knockdown was demonstrated by immunoblot analysis on homogenized tumor tissue **(Figures 27g and 29b)** and biochemically via the induction of aspartate **(Figure 29c)**. Immunohistochemistry for GOT1 indicate potent knockdown in the PDA cell compartment **(Figure 29d)**. Tumor growth suppression was confirmed at the molecular level by a decrease in Ki-67, a marker for proliferation **(Figure 29d)**. GOT1 knockdown tumors exhibited minimal staining for cleaved caspase 3 (CC3), a marker for apoptosis. Thus, these proliferative defects were independent of apoptosis, indicating GOT1 inhibits tumor proliferation, rather than, inducing cell death **(Figure 29d)**.

To test the hypothesis that GOT1 inhibition is cytostatic, we examined the effect of GOT1 knockdown on cell cycle progression. Knockdown led to a higher distribution of cells in G1 phase versus the S and G2 phases, indicating that the majority of cells are in G1 cell cycle arrest following five days of dox treatment **(Figures 27h and 29e)**. Moreover, the effect of GOT1 knockdown was reversible, as cells regained proliferative capacity upon removal of genetic inhibition **(Figures 27i and 29f)**. Overall, PDA display a spectrum of sensitivity to GOT1 where GOT1 inhibition arrests proliferation.

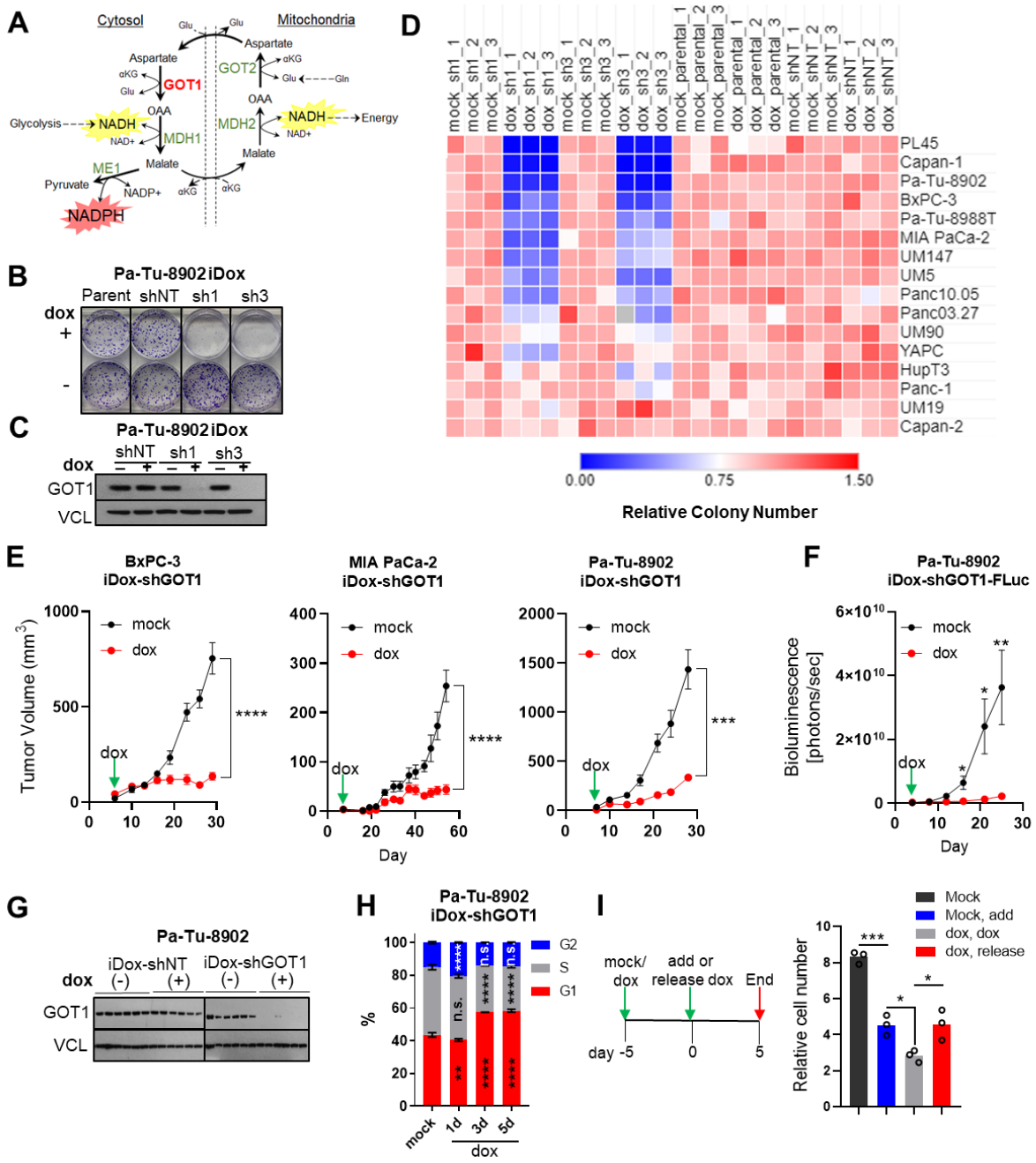

Figure 27. PDA requires GOT1 for growth and cell cycle progression.
A) Malate-aspartate shuttle model. **B-C)** Colony formation and immunoblot analysis of Pa-Tu-8902 cells stably expressing iDox-shRNA constructs following 10 days GOT1 knockdown. shRNAs target the coding region of GOT1 (sh1), or the 3'UTR region of GOT1 (sh3). Parental (parent) and scramble (shNT) conditions are also displayed (n=3). Vinculin (VCL) was used as a loading control. **D)** Relative colony number across a panel of PDA cell lines (n=3). **E)** Subcutaneous xenograft tumors from 3 PDA cell lines. Treatment with dox (red) or vehicle (black) (BxPC-3 n= 8, MIA PaCa-2 n=6, Pa-Tu-8902 n=6 per arm). **F)** Orthotopic xenograft tumor growth from Pa-Tu-8902 iDox-shGOT1 stable cell lines co-expressing firefly luciferase (FLuc) n=5 and n=6 mice were used for vehicle and dox cohorts respectively. **G)** Immunoblot analysis on tumors from **(E)**. **H)** Cell cycle distribution of Pa-Tu-8902 iDox-GOT1 sh1 upon 1,3, or 5 days of dox treatment. Significance values are in relation to iDox-shGOT1 mock (n=3). **I)** Proliferation kinetics following GOT1 knockdown. Cells were untreated (black), dox was added to untreated cells (blue), pre-treated with dox and chronically exposed to dox (grey), or released from dox pretreated cells (red). Relative cell number at day 5 normalized to day 1 is displayed, (n=3).Error bars represent mean ± SD. Two-tailed unpaired T-testor 1-way ANOVA: Non-significant P > 0.05 (n.s. or # as noted), P≤ 0.05 (*), ≤ 0.01 (**), ≤ 0.001 (***), ≤ 0.0001 (****).

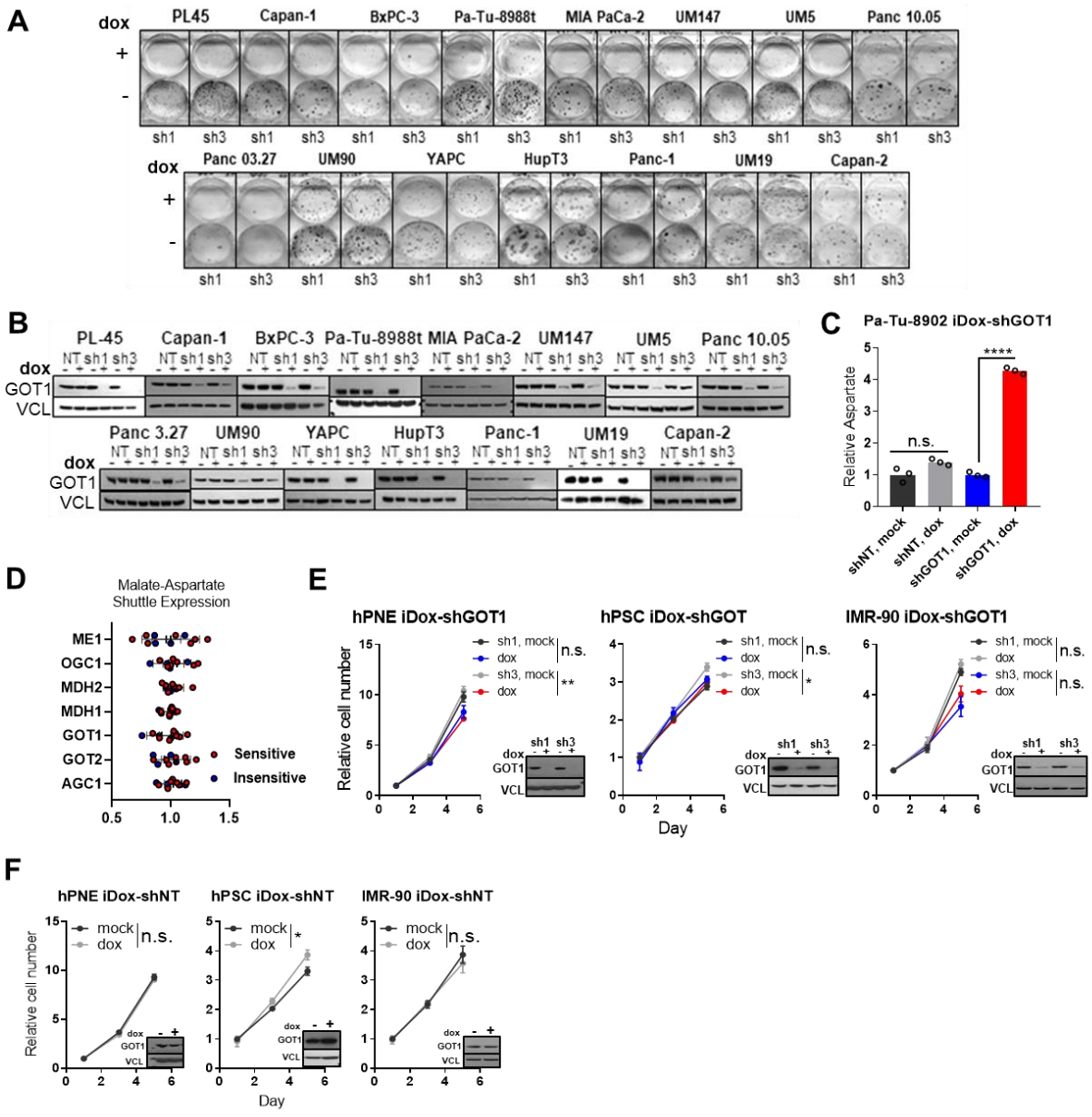

Figure 28. GOT1 is dispensable in non-transformed cell lines.
A-B) Colony formation assays and GOT1 immunoblots **(B)** from 1d. **C)** LC-MS/MS measurements of aspartate following five days of knockdown, n=3. **D)** mRNA expression of malate-aspartate shuttle components in PDA cell lines from the Cancer Cell Line Encyclopedia. **E-F)** Proliferation of immortalized non-transformed human cell lines normalized to day 1, n=3. Error bars represent mean ± SD. Two-tailed unpaired T-testor 1-way ANOVA: Non-significant P > 0.05 (n.s. or # as noted), P≤ 0.05 (*), ≤ 0.01 (**), ≤ 0.001 (***), ≤ 0.0001 (****).

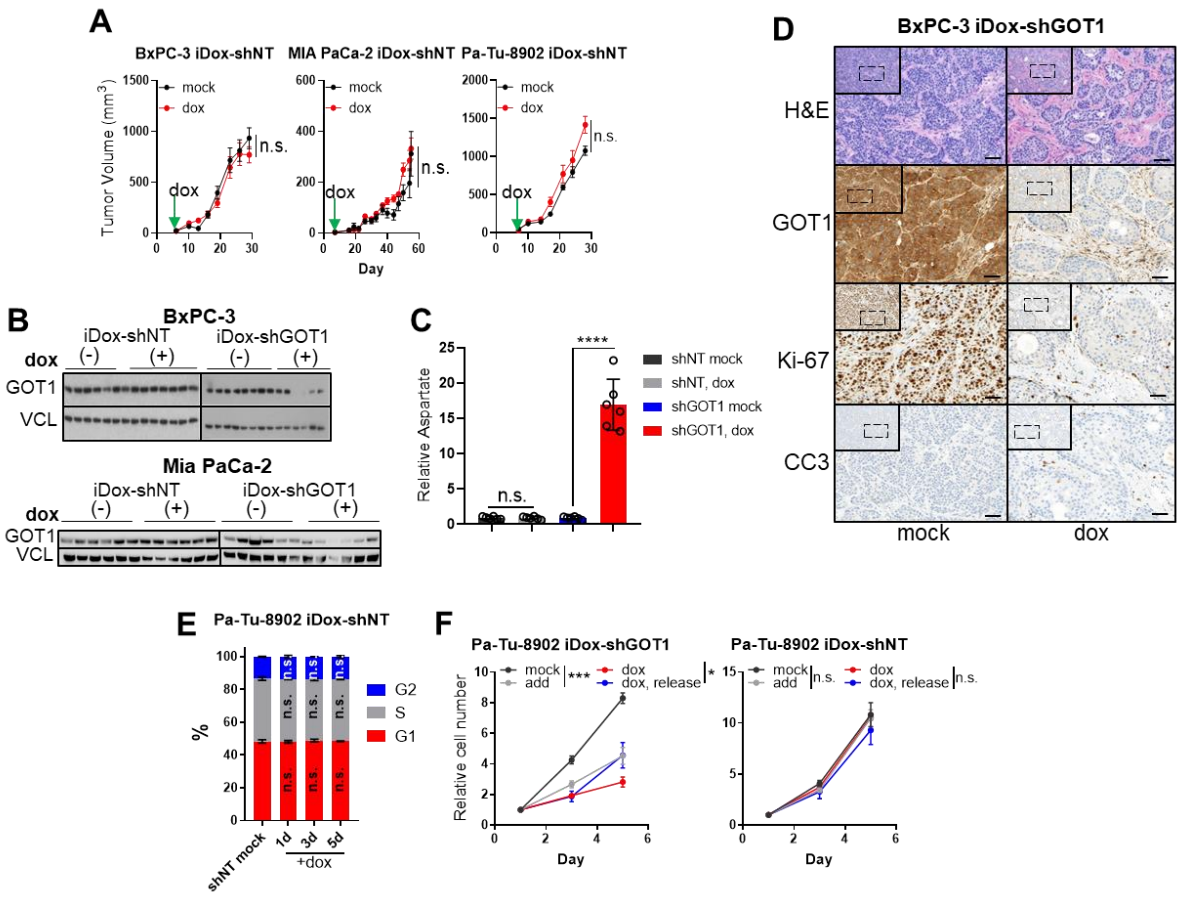

Figure 29. GOT1 inhibition is cytostatic.
A) Growth of subcutaneous xenograft tumors containing non-targeting 862(NT) vectors treated with dox (red) or vehicle (black) (n= 6), corresponding to Figure 1F. **B)** Immunoblots for GOT1 from tumors in 1F. **C)** LC-MS/MS measurements of aspartates taken from homogenized Pa-Tu-8902 iDox-shGOT1 tumors, n=6. **D)** Histology of BxPC-3 iDox-shGOT1 subcutaneous xenograft tumors from vehicle-or dox-treated mice. H&E, Hematoxylin and Eosin, CC3, cleaved caspase 3. Scale bars represent 50µm. **E)** Cell cycle upon 1,3, or 5 days of dox treatment. Significance values are in relation to iDox-shGOT1 mock (n=3). **F)** Proliferation kinetics following GOT1 knockdown. Cells were untreated (black), dox was added to untreated cells (blue), pre-treated with dox and chronically exposed to dox (grey), or released from dox pretreated cells (red). Relative cell number at day 5 normalized to day 1 is displayed, (n=3).Error bars represent mean ± SD. Two-tailed unpaired T-testor 1-way ANOVA: Non-significant P > 0.05 (n.s. or # as noted), P≤ 0.05 (*), ≤ 0.01 (**), ≤ 0.001 (***), ≤ 0.0001 (****).

Limiting Exogenous Cystine Potentiates GOT1 Inhibition

Because GOT1 inhibition is cytostatic, we sought to identify metabolic dependencies induced by knockdown that could be targeted to selectively kill PDA[8]. To test this, we examined the sensitivity of PDA cells in response to panel of metabolism-targeted small molecules. Cells were subjected to five days of dox treatment to ensure GOT1 knockdown followed by three days of drug treatment **(Figure 30a)**.

GOT1 inhibition was protective when combined with some inhibitors demonstrated by increased area under the curve values (AUC), a measure of drug sensitivity **(Figures 30b and 31a)**. Three of the five top desensitizing agents were chemotherapies, in agreement with previous observations[15]. Since these chemotherapies work through disrupting DNA replication of rapidly dividing cells, we speculate that the decreased sensitivity may occur due to the GOT1 growth-suppressive phenotype. By contrast, GOT1 knockdown sensitized PDA cells to erastin **(Figure 30b-c)**. Erastin is an inhibitor of the system x_c^- cystine/glutamate antiporter which transports cystine into cells in exchange for glutamate[9]. Cystine, the oxidized dimer of cysteine, is reduced to cysteine upon entering the cell where it can contribute to the synthesis of GSH and proteins, among numerous other biochemical fates.

GOT1 knockdown promoted a similar sensitization effect across additional PDA cell lines **(Figure 30d and 31b)** and was independent of dox interference **(Figure 31c)**. This sensitization effect was photocopied by imidazole ketone erastin (IKE) **(Figure 31d)** and promoted cell death **(Figure 31e)**. Furthermore, treating GOT1 knockdown cells with nano-molar doses of erastin or IKE drastically reduced cell numbers compared with single treatment arms **(Figures 30e and 31f)**. Supplementation with the exogenous cysteine or GSH sources, N-acetyl cysteine (NAC), β-mercapto ethanol (BME), or cell permeable GSH ethyl-ester (GSH-EE), prevented the combinatorial effect on cell viability **(Figures 30f and 31g)**, consistent with the concept that cystine import through system x_c^- is essential to maintain GSH levels[16].

Previous studies have found cystine levels were limiting in PDA tumors[17,18]. Based on these observations, we sought to test the effect of GOT1 knockdown under physiological concentrations of cystine. Culturing cells in tumor-relevant cystine potentiated GOT1 knockdown in a time- and dose-dependent manner **(Figures 30g**

and S32a-b), in agreement with our pharmacological studies. These results indicate PDA require exogenous cystine for growth and cell viability following GOT1 inhibition to aid cells in coping with redox stress[3,15]. In line with this observation, GOT1 inhibition lead to increased intracellular cysteine **(Figure S32c)** in both cell lines, where xCT protein levels were unchanged **(Figure S32d)**, suggesting higher cystine uptake.

To test this concept *in vivo*, we engrafted Pa-Tu-8902 iDox-shGOT1 cells engineered to express firefly luciferase (FLuc) into the pancreas, as in **Figure 27f**. Tumors were allowed to establish for 7 days, and treatment arms were initiated by providing dox-containing food formulated with or without the non-essential amino acid cysteine. While tumors in the animals fed a cysteine-free diet grew at comparable rates to tumors in animals fed a control diet, dox treated tumors grew substantially slower **(Figures 30h-i and 32e)**. Mice fed with a cysteine-free diet had lower cysteine in tumors compared to the control diet **(Figure 32f)**, indicating dietary inputs can influence tumor metabolism, but had no influence on tumor growth or burden. By contrast, cysteine was not significantly altered in tumors comparing dox-single or double treatment arms **(Figure 32f)**. The differences in tumor growth or tumor burden for animals on the dox or combination diet trended smaller, but did not reach statistical significance **(Figures 30h and 32e)**. We speculate that PDA tumors may acquire cysteine through alternative mechanisms when challenged by chronic cysteine deprivation. Overall, these data indicate that PDA cultures require exogenous cystine following GOT1 inhibition.

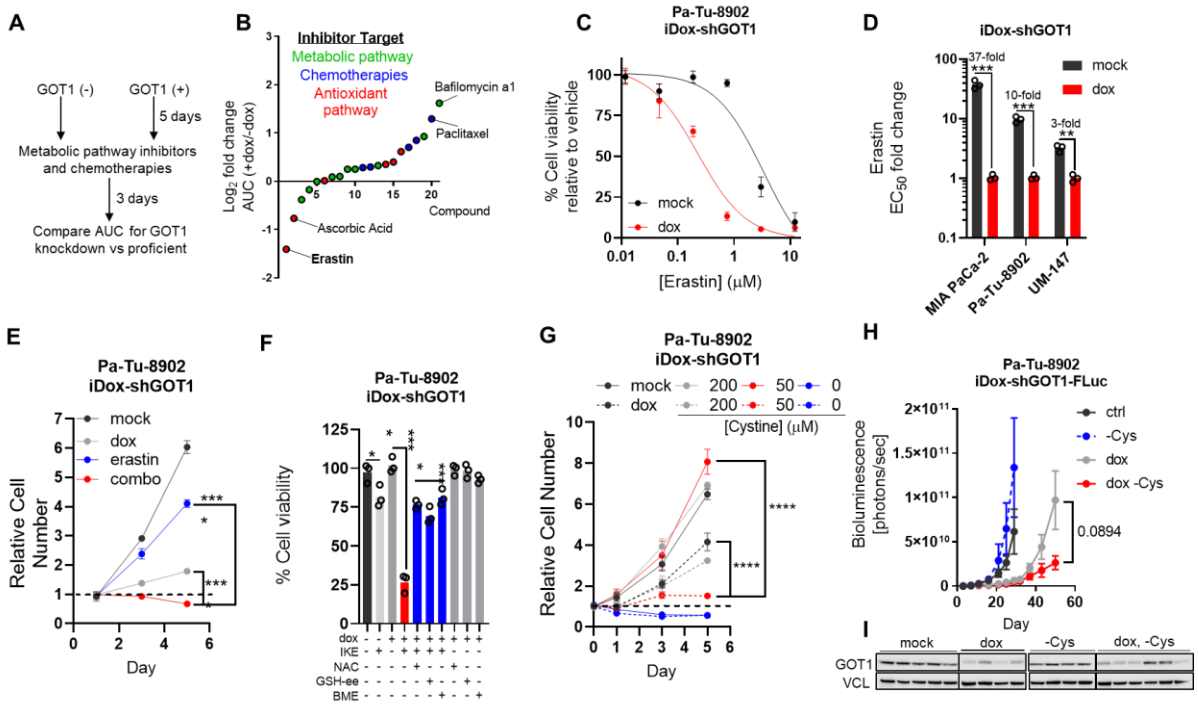

Figure 30. PDA requires cystine for viability and growth following GOT1 inhibition.
A) Screening strategy to identify metabolic dependencies following GOT1 suppression. **B)** Log_2 fold change in area under the curve (AUC) from cell viability dose response curves corresponding to each point, n=3. **C)** Cell viability dose response to erastin comparing mock (black) and GOT1 knockdown (red). **D)** GOT1 sensitization represented as the fold change in the erastin EC_{50}, n=3. **E)** Proliferation in response to the listed conditions, n=3. 5 days of GOT1 knockdown with the indicated media conditions for 24 hours. 750nM of Erastin was administered on day 1 and conditions are normalized to day 1 (n=3). **F)** Cell viability of Pa-Tu-8902 iDox-shGOT1 after 5 days of GOT1 knockdown then 24 hours of 750nM IKE combined with the indicated conditions. 250μM of N-acetyl-cysteine (NAC), 250μM GSH-ethyl ester (GSH-EE), and 50μM of beta-mercaptoethanol (BME) were used (n=3). **G)** Proliferation following GOT1 knockdown and the indicated media conditions (n=3). **H-I)** Orthotopic xenograft tumor growth from Pa-Tu-8902 iDox-shGOT1 stable cell lines co-expressing firefly luciferase (FLuc) treated with vehicle (black, n=6), dox containing food (red, n=6), cysteine-free diet (grey, n=5), or dox containing, cysteine-free food (blue, n=6). GOT1 immunoblot (I) taken from endpoint tumors. Error bars represent mean ±SD in B-G or mean ±SEM in H. Two-tailed unpaired T-test or 1-way ANOVA: Non-significant P> 0.05 (n.s. or # as noted), P≤ 0.05 (*), ≤ 0.01 (**), ≤ 0.001 (***), ≤ 0.0001 (****). See also supplemental figures 3 and 4.

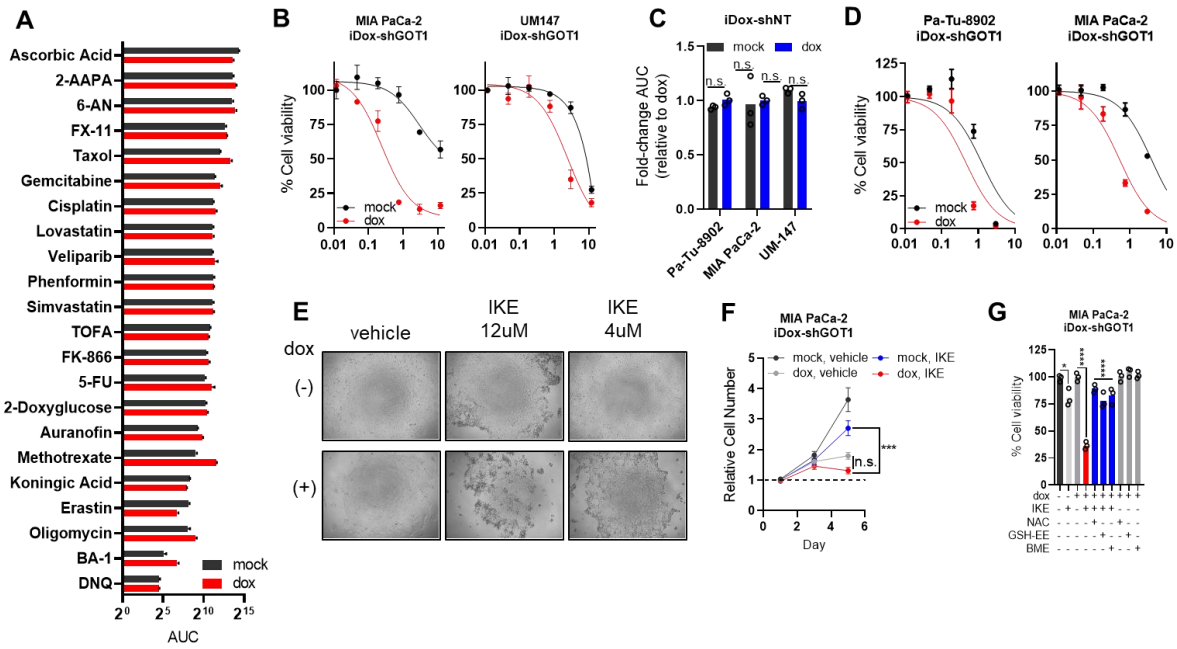

Figure 31. GOT1 Inhibition sensitizes PDA to x_c- inhibitors.
A) Area under the curve (AUC) in cell viability for each compound treated for 72 hours, (n=3). B) Cell viability dose response curves for erastin after 24 hours in iDox-shGOT1 expressing cell lines. **C)** AUC fold-change for shNT expressing cell lines, n=3. **D)** Imidazole ketone erastin (IKE) cell viability dose curves, n=3. **E)** Bright field images of Pa-Tu08982 iDox-shGOT1 cells treated with IKE. **F)** Proliferation after 5 days of dox treatment with the indicated conditions. 750nM of IKE was administered on day 1 and each condition is normalized to day 1 (n=3). G) Cell viability of Mia PaCa-2 iDox-883shGOT1 after 5 days of dox culture then 750nM IKE co-cultured with the indicated conditions (n=3). Error bars represent mean ± SD. Two-tailed unpaired T-test or 1-way ANOVA: Non-significant P> 0.05 (n.s. or # as 892noted), P≤ 0.05 (*), ≤ 0.01 (**), ≤ 0.001 (***), ≤0.0001 (****).

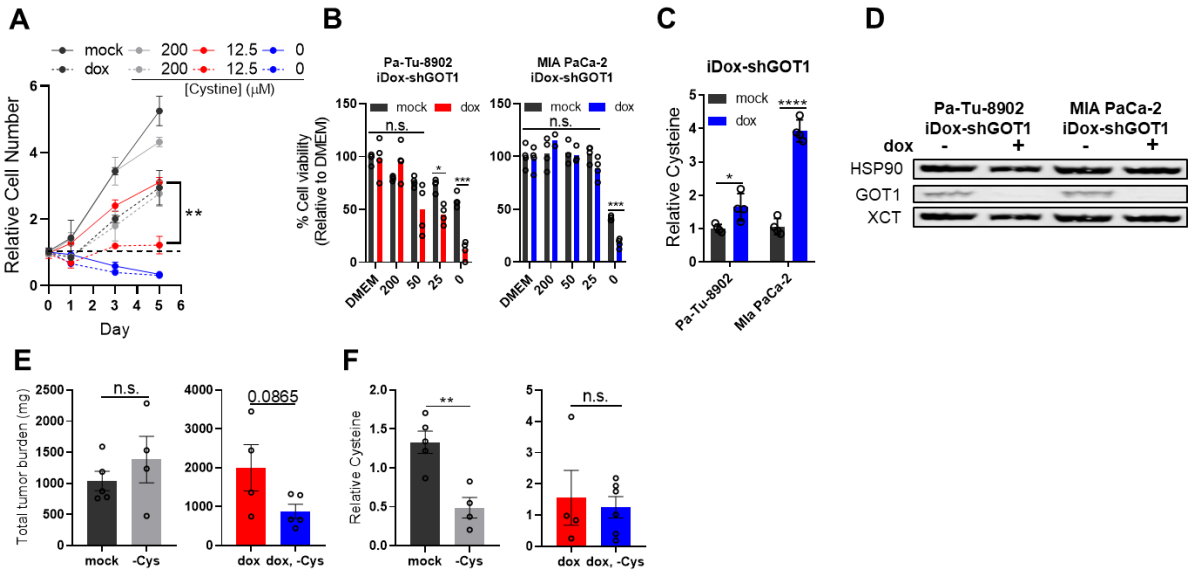

Figure 32. PDA cultures require exogenous cystine for proliferation and viability.
A) Mia PaCa-2 iDox-shGOT1 proliferation following 5 days of GOT1 knockdown and the indicated media conditions (n=3). I) Cell viability of Pa-Tu-8902 iDox-shGOT1 (red) and Mia PaCa-2 iDox-shGOT1 (blue) following 5 days of dox pre-treatment and 24 hours of the indicated cystine concentrations (n=4). **C)** LC-MS/MS measures of intracellular cysteine upon GOT1 knockdown, n=4. **D)** xCT levels are unchanged with GOT1 knockdown. **E)** Total post-treatment tumor burden (mock, n=5), (-Cys, 4), (dox, n=4), and (dox, -Cys, n=5). **F)** Cysteine levels in tumors at endpoint (mock, n=5), (-Cys, 4), (dox, n=4), and (dox, -Cys, n=6). Error bars represent mean ± SD (Figures A-C) or mean ± S.E.M (Figures E-F). Two-tailed unpaired T-test or 1-way ANOVA: Non-significant P> 0.05 (n.s. or # as noted), P≤ 0.05 (*), ≤ 0.01 (**), ≤ 0.001 (***), ≤0.0001 (****).

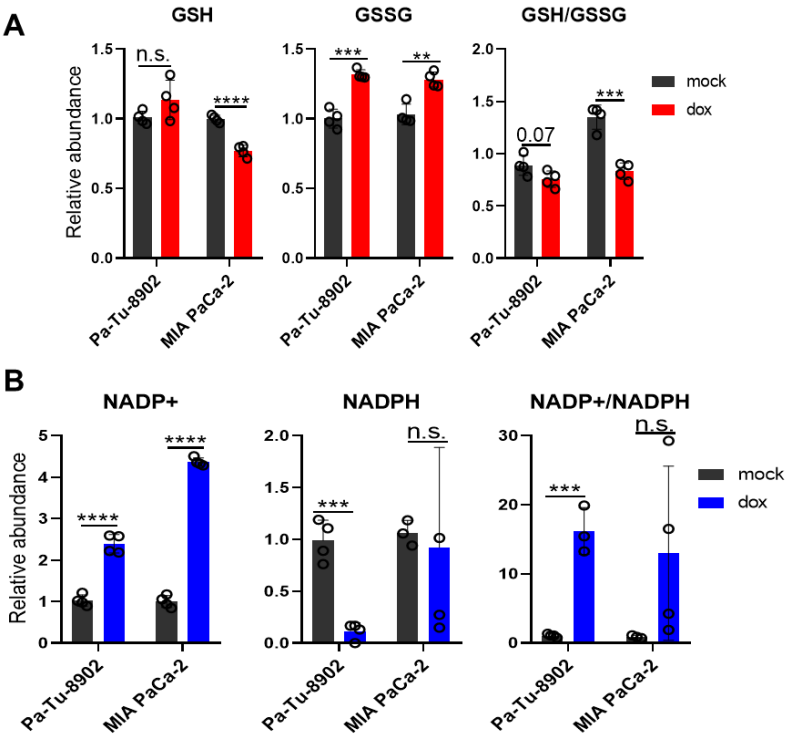

Figure 33. GOT1 inhibition promotes redox stress.
A-B) LC-MS/MS measures of redox co-factors, n=4. Two-tailed unpaired T-test: Non-significant P> 0.05 (n.s. or # as noted), P≤ 0.05 (*), ≤ 0.01 (**), ≤ 0.001 (***), ≤0.0001 (****).

Inhibiting GSH Biosynthesis Potentiates the Growth Inhibitory Effects of GOT1 Knockdown

Our data show that PDA cultures are heavily reliant on exogenous cystine following GOT1 inhibition and that PDA upregulate cysteine acquisition **(Figure 32c)** responding to GOT1 knockdown. Along these lines, GOT1 inhibition led to increased GSSG and $NADP^+$ while the changes in GSH and NADPH varied **(Figure 33a-b)**, suggesting cystine import could be required for cells to cope under redox stress. Because a major fate of cysteine is GSH, and since GSH-EE supplementation was blocked the GOT1-IKE combinatorial effect **(Figure 30f and 31g)**, we hypothesized GOT1 knockdown would, likewise, sensitize PDA to inhibition of *de novo* GSH synthesis **(Figure 34a)**.

The rate-limiting step in GSH synthesis is catalyzed by glutamate-cysteine ligase (GCL), which forms gamma glutamyl-cysteine through the condensation of glutamate and cysteine[19]. GCL is a holoenzyme which consists of a catalytic subunit (GCLC) and a modifier subunit (GCLM), and the GCLC subunit is targeted by the inhibitor buthionine sulfoximine (BSO), resulting in decreased GSH production **(Figure 34a)**. We observed that GOT1 knockdown enhanced sensitivity to BSO after 24 hours of drug treatment, contrasting an absent single agent response **(Figure 35a)**. Exposure to BSO for 72 hours further augmented the sensitizing effect **(Figures 34b and 35b-c)**. In some cases, the change in EC_{50} was nearly 100-fold **(Figure 34c and 35d),** indicating potent sensitization.

Recent studies have suggested that a majority of cancer cell lines survive upon 72 hours of BSO treatment despite potent inhibition of GSH levels at this time point[20]. Moreover, these studies have demonstrated that chronic BSO treatment, up to 9 days, is required in induce effects on proliferation or cell death [20]. In our models, 6 hours of BSO treatment was sufficient to diminish GSH levels **(Figure 35e)**, in line with previous kinetic data[20]. By contrast, co-treatment of GOT1 knockdown with BSO substantially reduced cell proliferation at 72 hours, while the effect of BSO alone was modest **(Figure 34d and 35f)**. 120 hours of treatment potentiated the effect in the GOT1 knockdown condition, whereas cells regained proliferative capacity under the BSO single treatment condition **(Figure 34d and 35f)**. The combinatorial effects on cell viability were rescued

by supplementing exogenous GSH-EE or NAC **(Figures 34e and 35g)**, in line with the model that GOT1 perturbs redox balance.

We then sought to determine whether this combination shows efficacy *in vivo* by examining the effect of GOT1 and BSO in established xenograft tumors. Mice were engrafted with Pa-Tu-8902 iDox-shGOT1 cells and given dox via chow after 7 days. BSO was administered via drinking water on day 14. While no tumor regressions were observed, the combination of GOT1 and BSO significantly slowed tumor progression compared with single treatment arms **(Figure 34f)** and led to complete stasis in one instance **(Figure 35h)**. Knockdown was confirmed immunoblot analysis **(Figure 35i)** and immunohistochemistry **(Figure 35j)**.

We then measured glutathione species in tumor metabolite fractions to demonstrate the pharmacodynamics of BSO. We found BSO to significantly reduce levels of gamma glutamyl-cysteine, a product of GCL, which is directly inhibited by BSO[19] **(Figure 34g)**. Concomitantly, we observed a significant reduction in GSH, GSSG, and the GSH/GSSG ratio upon BSO treatment **(Figure 34g)**, demonstrating BSO has on-target activity in established tumors, and the tumors are under redox stress. Together, our data reveal that PDA require glutathione synthesis under GOT1 deficient conditions.

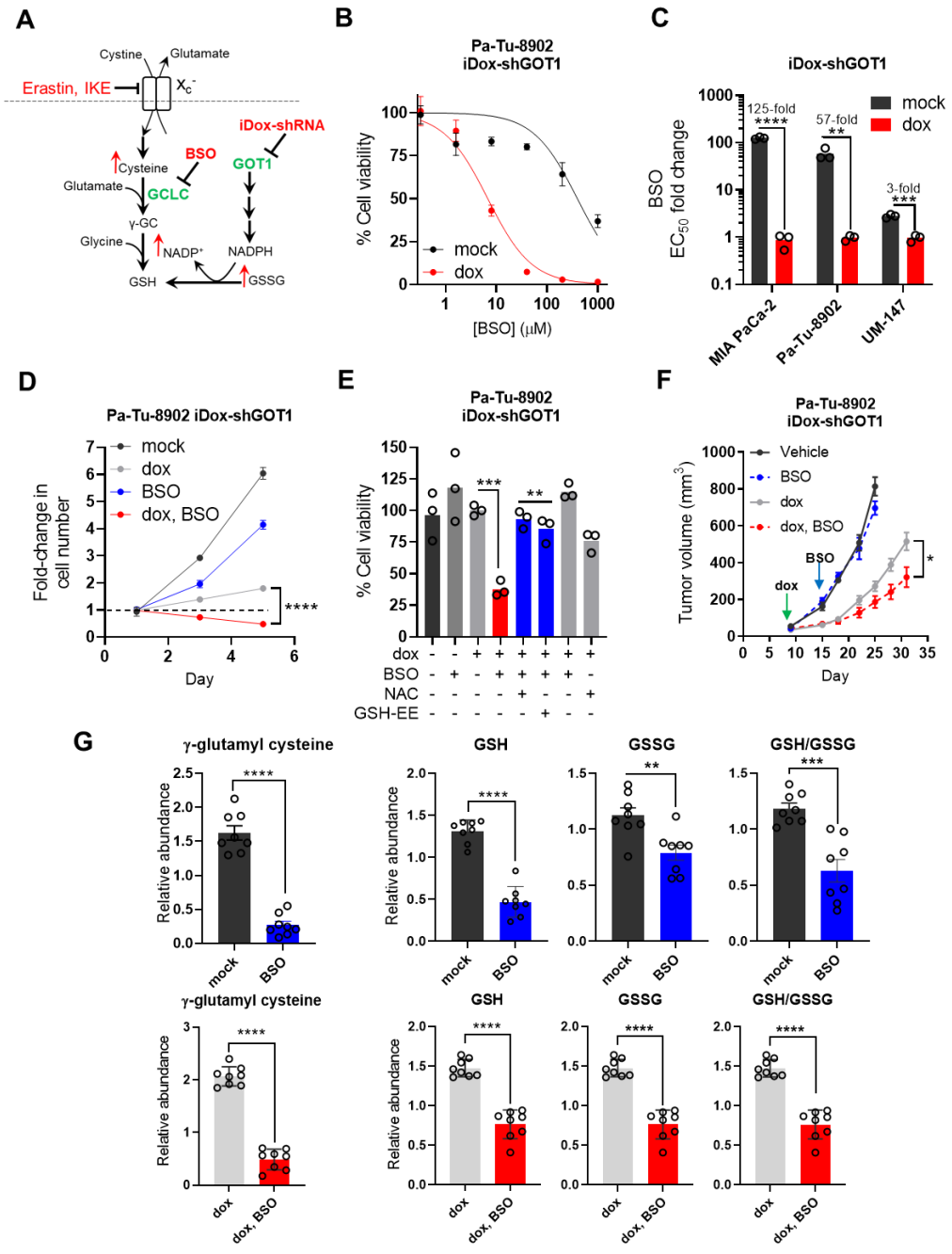

Figure 34. PDA require GSH synthesis for growth upon GOT1 suppression.
A) Scheme depicting GSH synthesis and metabolic changes following GOT1 inhibition. **B-D)** Cell viability dose response (B), EC_{50} fold change across multiple PDA cell lines, and proliferation (D), following 5 days of GOT1 knockdown and BSO treatment, n=3. **E)** ell viability following 72 hours of 40uM BSO or co-treatment with 0.5mM N-acetyl cysteine (NAC) or 0.5mM GSH-Ethyl Ester (GSH-EE) following 5 days of GOT1 knockdown (n=3). F) Subcutaneous xenograft growth of Pa-Tu-8902 iDox-shGOT1 cells treated with vehicle (black), 20 mg/kg BSO via drinking water (grey), doxycycline administered in the food (red), or the combination (blue). **G)** Relative abundance of gamma-glutamyl cysteine (γGC), GSH, GSSG, and the GSH/GSSG ratio from tumors in (F) (n=8). Error bars represent mean ± SD. Two-tailed unpaired T-test or 1-way ANOVA: Non-significant P> 0.05 (n.s. or # as noted), P≤ 0.05 (*), ≤ 0.01 (**), ≤ 0.001 (***), ≤0.0001 (****). See also supplemental figure 6.

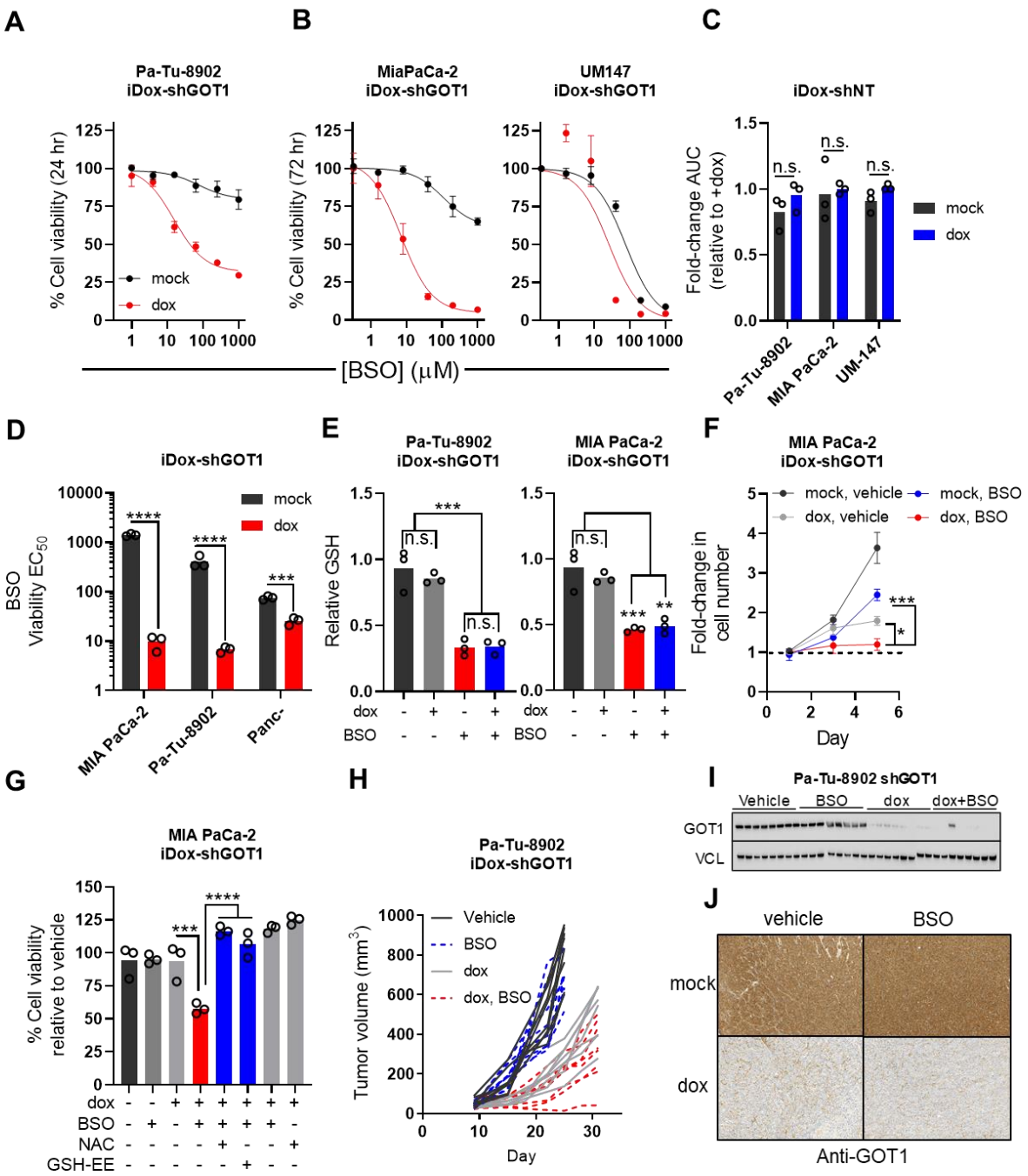

Figure 35. PDA require GSH synthesis under GOT1 deficient conditions.
A-B) Cell viability dose response at 24 (A) and 72 hours (B), n=3. **C)** AUC fold change in shNT matched cell lines, n=3. **D)** Raw EC_{50} measures from (B). **E)** GSH-glo measures, **n=3. F)** Proliferation after 5 days of GOT1 knockdown. BSO 40μM treatment was initiated on day 1 and curves are normalized to day 1, n=3. **G)** Relative viability after 5 days of GOT1 knockdown and treatment with 40μM BSO or co-treatment with 0.5mM N-acetyl cysteine (NAC) 0.5mM GSH-ethyl ester (GSH-EE, n=3). **H)** Individual tumor volume measurements corresponding to Figure 3F (n=8).I) Immunoblot analysis of GOT1 from tumors in Figure 3F (n=8). **J)** Immunohistochemical staining of GOT1, n=8. Error bars represent mean ± SD. Two-tailed unpaired T-test or 1-way ANOVA: Non-significant P> 0.05 (n.s. or # as noted), P≤ 0.05 (*), ≤ 0.01 (**), ≤ 0.001 (***), ≤0.0001 (****).

GOT1 Suppression Augments Ferroptosis Sensitivity

Previous work has demonstrated that some cell types are sensitive to erastin and BSO as single agents, and that these drugs can kill cells by depleting GSH. The proximal effects of GSH depletion are mediated through loss of GPX4 activity, which utilizes GSH as a co-factor to detoxify lipid peroxides **(Figure 36a)**. This can lead to the lethal accumulation of lipid peroxides, and ferroptosis[21]. Ferroptosis is a form of oxidative, non-apoptotic, iron-dependent, cell death that is triggered by excessive lipid peroxide levels **(Figure 36a)**[9,10]. While GOT1 inhibition does not induce ferroptosis, our data suggest it may predispose PDA cells to ferroptosis.

To investigate whether GOT1 can sensitize PDA to ferroptosis, we first examined the combinatorial effect of GOT1 knockdown together with RSL3, a covalent inhibitor of GPX4 and direct inducer of ferroptosis[21]. RSL3 in combination with GOT1 knockdown was substantially more potent than as a single agent **(Figure 36b)**, and this effect was evident across a panel of PDA lines **(Figures 36c and 37a)** where the effect was cytotoxic **(Figure 37b)** and independent of dox effects **(Figure 37c)**. Moreover, the combination reduced proliferation **(Figures 36d and 37d)**.

We then employed the C11-BODIPY lipid peroxidation sensor to investigate how inhibition of GPX4 and GOT1 affected lipid peroxidation. While the effect of GOT1 inhibition on lipid ROS induction was modest **(Figures 36e and 37e)**, GOT1 inhibition substantially upregulated lipid ROS combined with RSL3 or erastin **(Figures 36e and 37e-f)**. The effect could be reversed through co-treatment with the lipophilic antioxidant ferrostatin-1 (Fer-1) **(Figure 37e)**. Next, we examined whether cell death could be prevented by co-treatment with agents that relieve lipid peroxidation or chelate iron[9,10]. Co-treatments with Fer-1 prevented the GOT1 sensitization effect uniformly across multiple ferroptosis inducers **(Figure 36f)** and over a time course **(Figure 37g)**. Moreover, treatment with the lipophilic antioxidant, Trolox, or iron chelator deferoxamine (DFO), provided substantial protection **(Figure 36f)**. To rule out the possibility that GOT1 was sensitizing PDA to alternative mechanisms of cell death, namely apoptotic, necrotic, or autophagic cell death, we co-treated GOT1 knockdown with well-characterized inhibitors of these cell death pathways. Co-treatment with the pan-caspase inhibitor (Z-VAD-FMK), RIPK-1 inhibitor (Necrostatin-1), or lysosomal

acidification inhibitor (Bafilomycin A1) offered limited protection compared with lipophilic antioxidants or iron chelation **(Figures 36g and 37h)**, suggesting ferroptosis is the predominant mechanism of cell death. Finally, we explored triggering ferroptosis by $FINO_2$ which causes iron oxidation and indirectly inhibits GPX4 activity[22]. GOT1 suppression also sensitized PDA to ferroptosis **(Figures 37i-j)**. Overall, our data demonstrate GOT1 inhibition primes PDA for ferroptosis in cell culture.

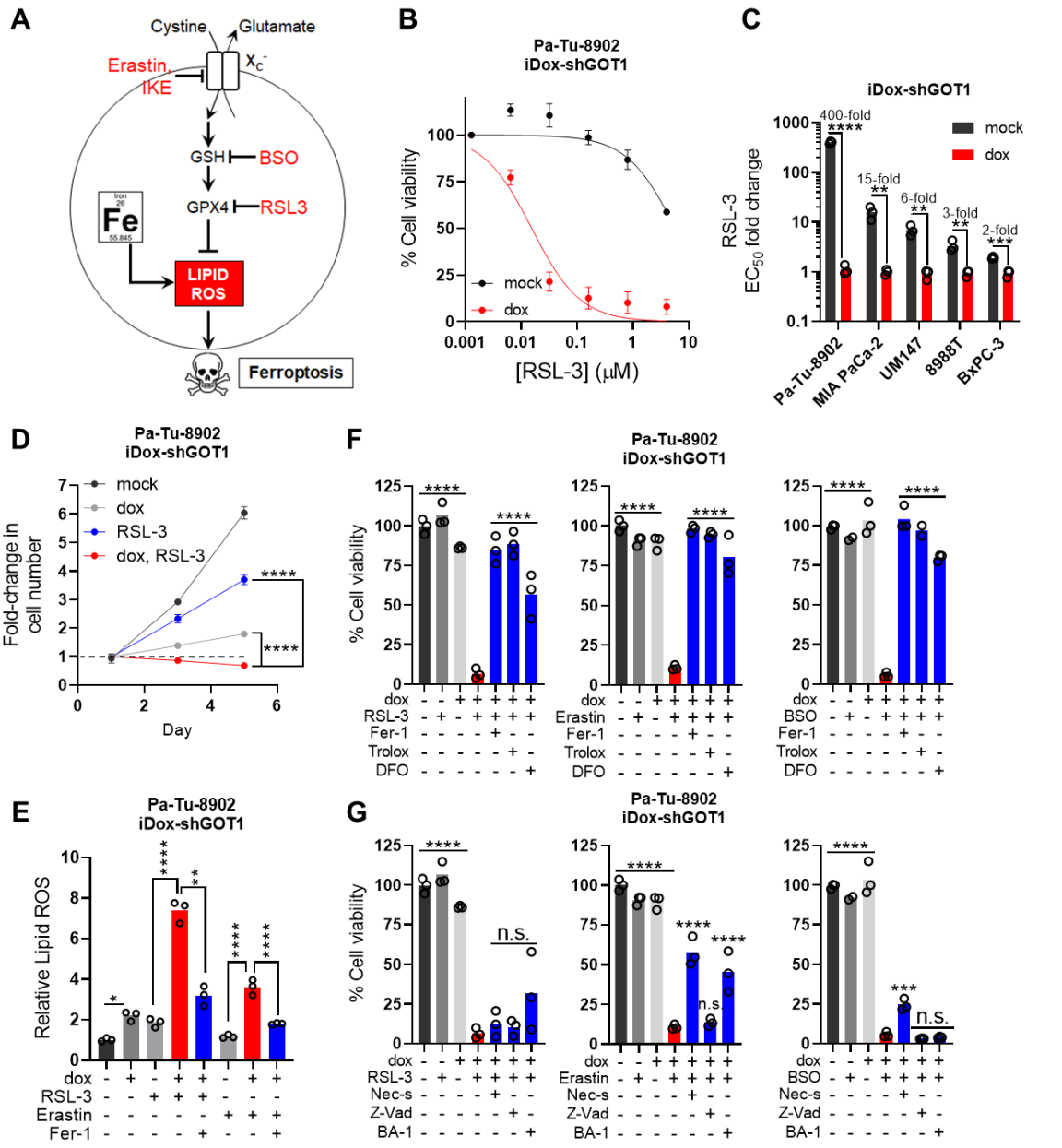

Figure 36. GOT1 inhibition sensitizes PDA to ferroptosis.
A) Scheme of the GPX4 arm of ferroptosis. **B-D)** Cell viability dose response curve at 24 hours (A), EC_{50} fold changes in dose response (C), and proliferation (D). **E)** Relative lipid ROS in Pa-Tu-8902 iDox-shGOT1 treated with 32nM RSL3 or750nM Erastin -/+ 1μM Ferrostatin-1(Fer-1) for 6hours (n=3). **F)** Cell viability Cell viability of Pa-Tu-8902 iDox-shGOT1 cultured in vehicle (0.1% DMSO) -/+ dox (black and light grey), drug (32nM RSL-3, 750nM Erastin, 40μM BSO) -/+ dox (grey and red), or drug and dox (blue) in the presence of lipophilic antioxidants 1μM Fer-1 and 100μM Trolox, or an iron chelator 10μM DFO (deferoxamine). Viability was assessed after 24 hours of treatment for RSL-3 and Erastin conditions and 72 hours for BSO treatment conditions. GOT1 was knocked down for 5 days prior to treatment. Data are normalized to the –dox and vehicle treated control (n=3). **G)** Cell viability flowing the procedure in (F) but in the presence of 10μM Necrostatin-1 (Nec-s, apoptosis inhibitor), 50 μM ZVAD-FMK (Z-Vad, apoptosis inhibitor), or 1 nM bafilomycin A1 (BA-1, lysosomal acidification inhibitor), n=3.

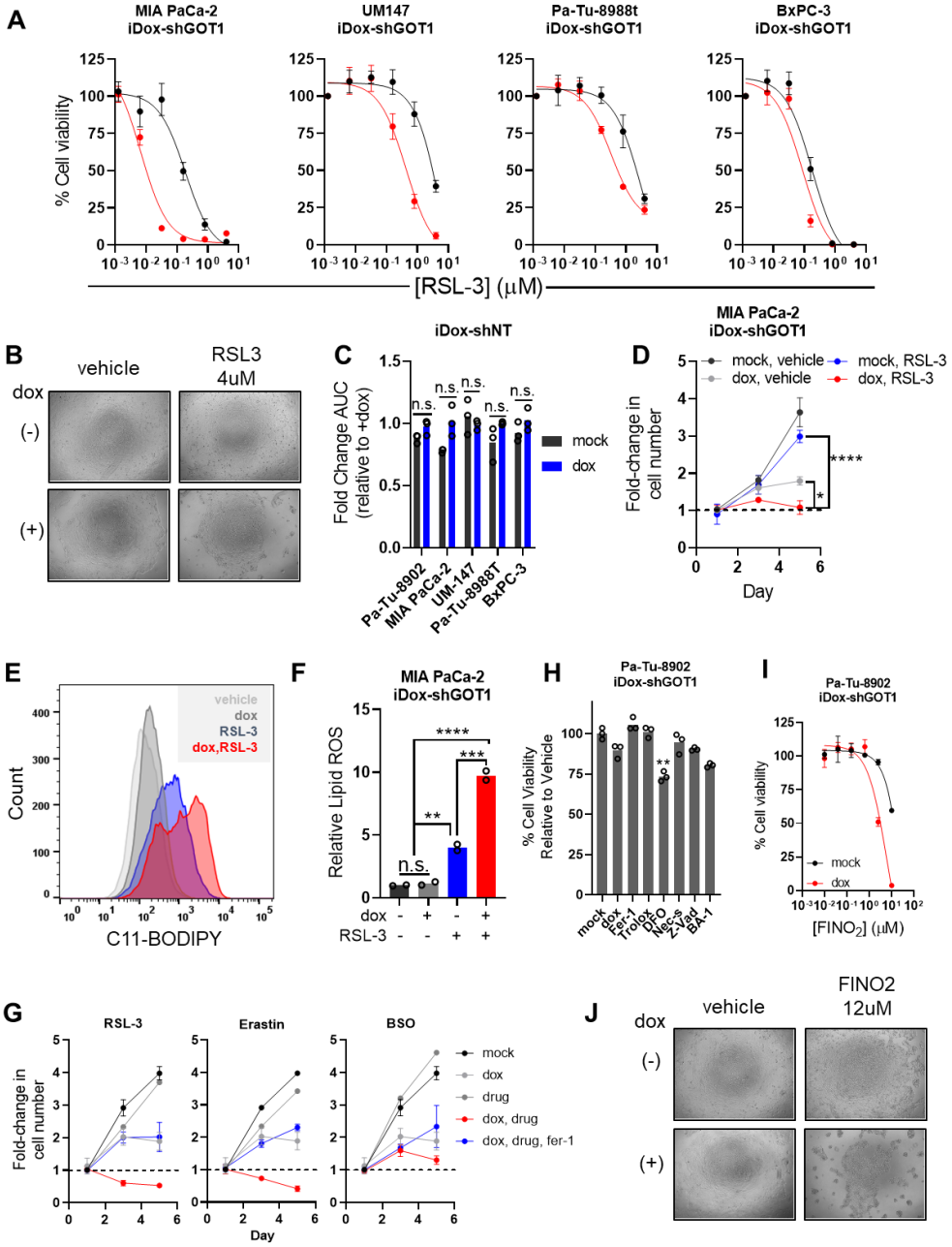

Figure 37. GOT1 inhibition augments ferroptosis in PDA.
A) Cell viability dose response curves at 24 hours, n=3. **B)** Bright field images of Pa-Tu-8902 iDox-shGOT1 cells treated with RSL3. **C)** Fold change in cell viability AUC in shNT cells. **D)** Proliferation following 5 days of knockdown and treatment with the indicated conditions. 32nM of RSL-3 was administered on day 1. Cell numbers are normalized to day 1 for each condition (n=3). E) Distribution of Pa-Tu-8902 iDox-shGOT1 cells positive for C11-BODIPY corresponding to (4E). **F)** Fold change in viable MIA PaCa-2 iDox-shGOT1 cells positive for C-11 BODIPY, following 5 days of GOT1 knockdown. Cells were treated with the indicated conditions for 6 hours prior to measurements: vehicle (0.1% DMSO) -/+ dox (black and grey), 1μM RSL3.Data are normalized to the –dox and vehicle-treated condition (n=2). **G)** Proliferation of Pa-Tu-8902 iDox-shGOT1 following 5 days of knockdown and treatment with the indicated conditions (n=3). 32nM RSL-3, 750nM Erastin, or 40μM BSO -/+ 1μM Ferrostatin-1 (Fer-1) were used. Cell numbers are normalized to day 1 for each condition (n=3). **H)** Single agent viability controls for 4F-G, n=3. **I-J)** Cell viability dose-response curves and bright field image **(J)** upon 24 hours of $FINO_2$ treatment following 5 days of GOT1 knockdown (n=3). Error bars represent mean ± SD. Two-tailed unpaired T-test or 1-way ANOVA: Non-significant P> 0.05 (n.s. or # as noted), P≤ 0.05 (*), ≤ 0.01 (**), ≤ 0.001 (***), ≤0.0001 (****).

GOT1 Inhibition Primes PDA for Ferroptosis by Promoting Labile Iron

Ferroptosis is coupled to the cell's metabolic state where increasing intracellular free iron levels can augment ferroptosis[12,13]. We tested the possibility that GOT1 inhibition was leading to labile iron release first by measuring Calcein-AM fluorescence via flow cytometry. Calcein-AM is a fluorescein-derived probe that is quenched when bound to ferrous iron (Fe^{2+})[23]. Calcein-AM staining of GOT1 proficient cells defined basal fluorescence. GOT1 knockdown cells shifted fluorescence distribution to lower intensity, indicating labile iron pools were increased following GOT1 knockdown **(Figures 38a-b and 39a)**. This observation was corroborated by orthogonal measurements employing the RhoNox-1[24] iron probe **(Figure 38c-d).** The effect of labile iron was evident phenotypically where higher DFO concentrations were required to rescue cell viability upon ferroptosis inhibitor treatment **(Figures 38e and and 39e)**.

Iron levels can be altered by downregulating iron efflux, upregulating iron uptake, or promoting the degradation of intracellular iron carriers—ferritin or heme[25] **(Figure 39b)**. GOT1 knockdown did not upregulate expression of iron transport proteins (*SLC40A1* and *TFRC*) **(Figures 39c-d)**. Moreover, expression of heme oxygenase 1 (*HMOX1*), which releases labile iron through the degradation of heme was unaltered in Pa-Tu-8902. It was however modestly upregulated in Mia PaCa-2 **(Figure 39d)**. Moreover, GOT1 inhibition reduced ferritin protein levels **(Figure 38f)**, while additional iron regulating proteins were unchanged, suggesting iron could be liberated through released via NCOA4-dependent autophagy, in a process termed ferritinophagy[11]. NCOA4 is autophagosome cargo receptor that binds to the ferritin heavy chain sequestering ferritin for degradation by the autolysosome to release labile iron. By contrast Mia PaCA-2 downregulated NCOA4 and IRP2 and upregulated TFR1 **(Figure 38f)**, in line with the iron starvation response[12]. Both mechanisms of labile iron release employ vacuolar (V-)ATPases to drive the acidification of the lysosome and endosome to degrade iron carriers[11,26,27]. Indeed, blocking V-ATPases prevented GOT1-mediated ferroptosis **(Figures 38g and 39f)**. More broadly, ferric ammonium citrate supplementation enhanced sensitivity to ferroptosis inducing compounds **(Figure 39f)**.

In parallel we conducted whole-transcriptome profiling and found the catabolic pathways "Lysosome" **(Figure 40a)** and "Autophagy-Lysosome" **(Figure 38h)**

signatures were enriched in Pa-Tu-8902 by gene set enrichment analysis[28]. Autophagy is a catabolic process that protects cells from metabolic stress induced by nutrient deprivation[29]. Indeed, GOT1 knockdown upregulated autophagic flux in Pa-Tu-8902, indicated by the difference in LC3-B in vehicle and inhibitors of autophagic flux hydroxychloroquine (HCQ) and BafA1 (**Figures 38i and 40b)**. Moreover, GOT1 inhibition led to decreased p62, which is selectively degraded during autophagy **(Figure 38i)**. Importantly, blocking autophagic flux restored ferritin protein levels **(Figure 38i) and** NCOA4 knockdown prevented GOT1-mediated ferroptosis in Pa-Tu-8902 **(Figures 38J and 40c-e)**, supporting the model that GOT1 promotes labile iron through ferritinophagy. Together our data suggest GOT1 inhibition primes PDA for ferroptosis by promoting labile iron.

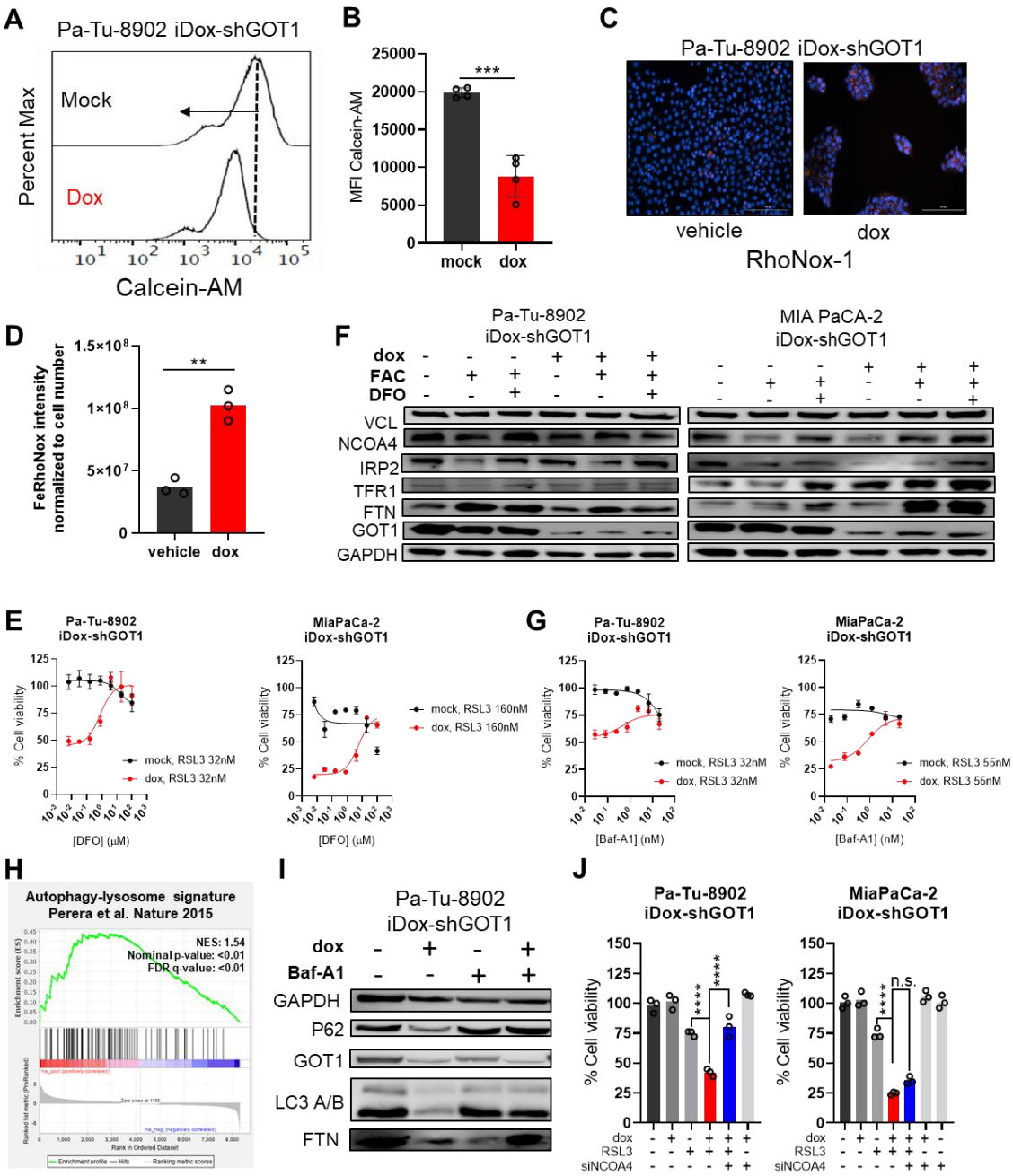

Figure 38. GOT1 inhibition promotes labile iron release.
A-B) Calcein-AM histogram (A) and mean fluorescence intensity (MFI) upon five days of GOT1 knockdown (B), n=3. **C-D)** Visualization (C) and quantification (D) of GOT1 knockdown cells treated with the iron probe RhoNox-1, n=3. **F)** Immunoblots of iron regulatory proteins. **E-G)** Cell viability dose response rescues of cells co-treated with the indicated concentration of RSL3 and increasing doses of DFO (E) or Baf-A1 (G), n=2. **H)** Enrichment of autophagy-lysosome transcripts in Pa-Tu-8902 iDox-shGOT1 cells following GOT1 knockdown. **I)** Western of autophagy markers and ferritin following GOT1 knockdown. **J)** Cell viability in cells co-treated with RSL3 and siNCOA4 following GOT1 knockdown, n=3. Error bars represent mean ± SD. Two-tailed unpaired T-test or 1-way ANOVA: Non-significant P> 0.05 (n.s. or # as noted), P≤ 0.05 (*), ≤ 0.01 (**), ≤ 0.001 (***), ≤0.0001 (****).

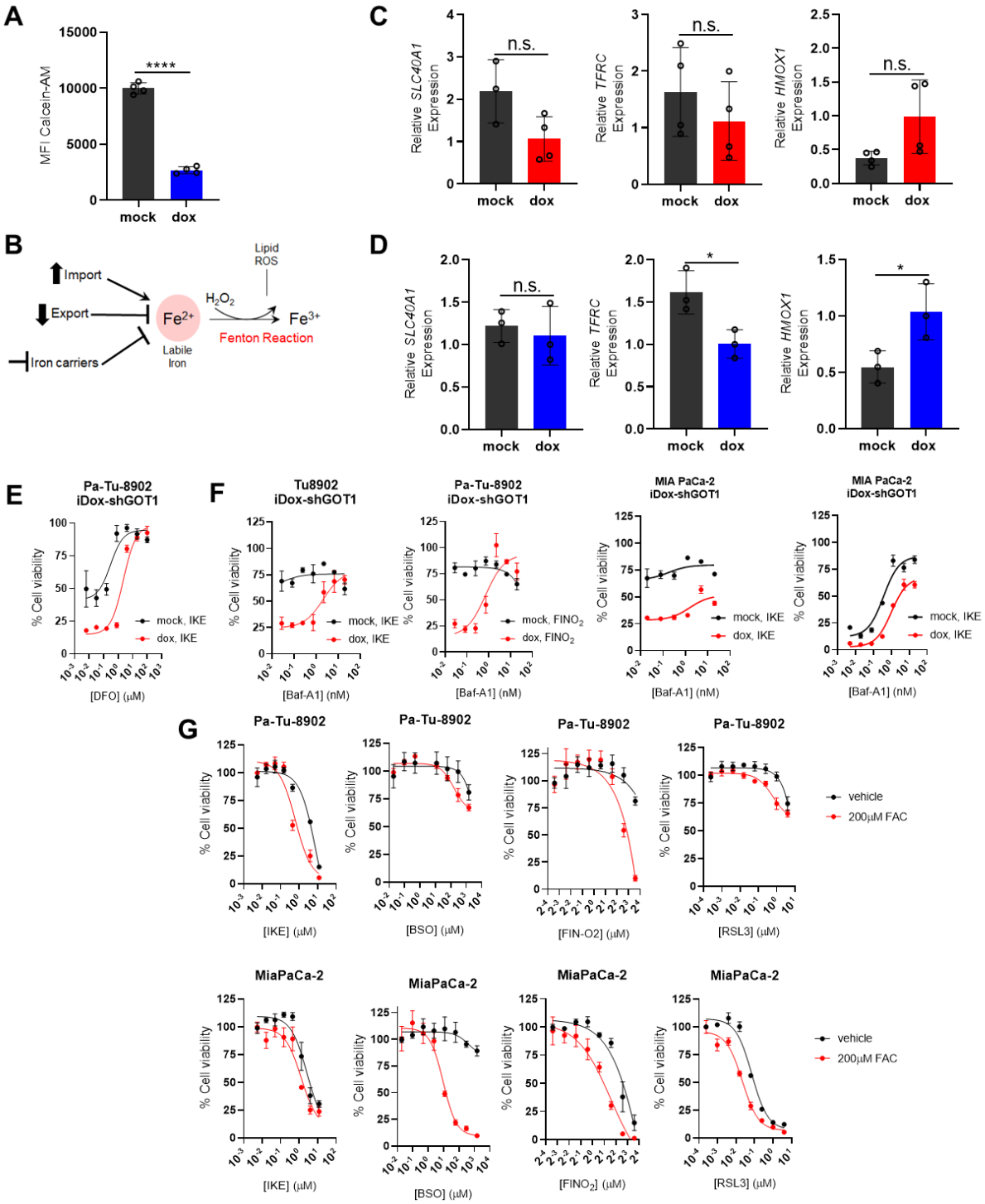

Figure 39. Labile iron sensitizes PDA to ferroptosis inducers.
A) Calcein-AM MFI in Mia PaCa-2 iDox-shGOT1 following GOT1 knockdown, n=3. **B)** Scheme of iron release mechanisms. **C-D)** Expression of SLC40A1, TFRC, and HMOX1 in Pa-Tu08902 (red) or Mia PaCa-2 iDox-shGOT1 cells (blue). **E-G)** Cell viability dose response curves of various ferroptosis inducers treated with DFO (n=3), Baf-A1 (n=2), or 200μM of ferric ammonium citrate (FAC). All assays were readout after 24 hours. Error bars represent mean ± SD. Two-tailed unpaired T-test or 1-way ANOVA: Non-significant P> 0.05 (n.s. or # as noted), P≤ 0.05 (*), ≤ 0.01 (**), ≤ 0.001 (***), ≤0.0001 (****).

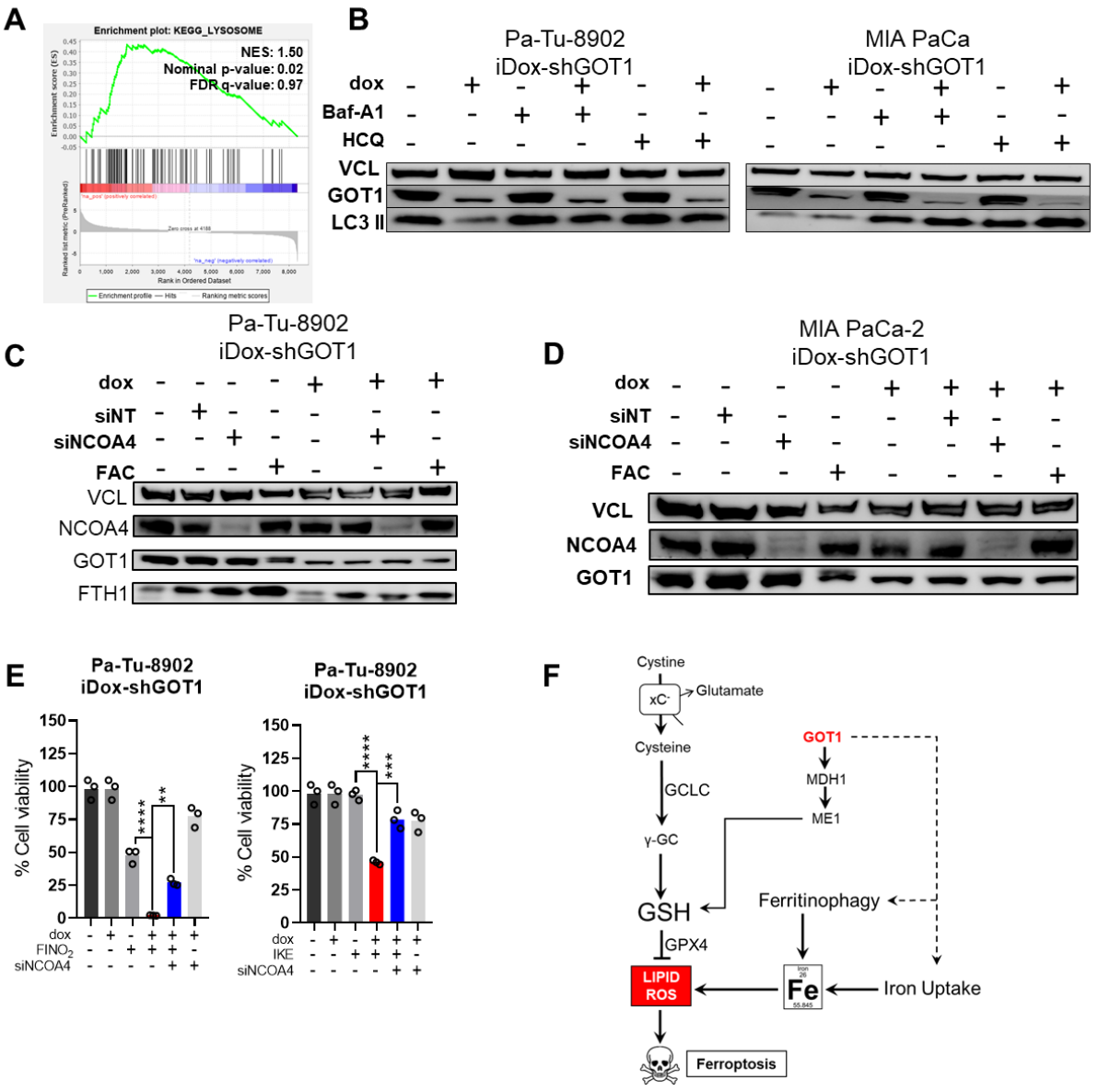

Figure 40. GOT1 silencing induces ferritinophagy.
A) Enrichment of lysosomal transcripts following GOT1 silencing in Pa-Tu-8902 iDox-shGOT1, n=3. **B-C)** Western blot analysis of autophagic flux (B) and autophagy markers in response to GOT1 over expression (C). **D)** Knockdown of NCOA4 rescues GOT1-mediated ferroptosis, n=3. **E)** Western blot for NCOA4. **F)** GOT1 inhibition primes PDA for ferroptosis by promoting labile iron release. Error bars represent mean ± SD. Two-tailed unpaired T-test or 1-way ANOVA: Non-significant P> 0.05 (n.s. or # as noted), P≤ 0.05 (*), ≤ 0.01 (**), ≤ 0.001 (***), ≤0.0001 (****).

4.4 Discussion

Here, we report that inhibition of GOT1 suppresses the growth of numerous PDA cell lines, primary culture models, and xenograft tumors, while rendering cells susceptible to ferroptosis. Ferroptosis could be triggered by inhibiting cystine import, glutathione synthesis, or GPX4 in synergy with GOT1, which we ascribe to the

promotion of intracellular iron levels through upregulating iron import and the autophagic degradation of ferritin.

The role of GOT1 in ferroptosis has been the subject of previous study in several other tumor types. Our data lie in contrast to some previous work, which have suggested that GOT1 inhibition protects cells from ferroptosis by blocking mitochondrial metabolism[36–39]. Our data reveal the downstream effects of GOT1 inhibition are iron release this metabolic adaption can sensitize PDA cells to ferroptosis, in line with previous studies suggesting labile iron can sensitize cells to ferroptosis[12,13]. The differences emerging from these studies likely reflect the incomplete understanding of regarding GOT1, iron regulation, and ferroptosis in cancer cells arising from different tissues.

Labile iron through the iron starvation response or NCOA4-dependent autophagy have been implicated in supporting mitochondrial metabolism by supplying iron. These mechanisms are believed to support iron sulfur cluster synthesis, among other fates[12,32,40]. Several groups have shown in mammalian cells and yeast that lysosomal acidification supports mitochondrial metabolism by serving as an iron source[41–43]. Based on the data presented here, and that of other groups, we posit that the labile iron is released following GOT1 inhibition could be an adaptive response to support mitochondrial metabolism.

More broadly, ferrous iron is required for ferroptosis where it contribute to the oxidation of membrane PUFAs, either as free iron or as a co-factor for lipoxygenase enzymes[10,23,24]. We show that iron alone can influence sensitivity to ferroptosis inducing small molecules. Along these lines, several groups are engaged in developing iron-activated pro-drugs to selectively exploit the oxidative environment promoted by labile iron[44–46]. Iron metabolism is altered in several cancers[31], whether these cell types are sensitive to ferroptosis triggering agents, or how labile iron pools are altered in these contexts are open questions. Overall, data reveal GOT1 inhibition and subsequent labile iron release augment ferroptosis sensitivity in PDA cell lines and suggest labile iron could be a targetable vulnerability in PDA.

4.5 Materials and Methods

Cell Culture

PL45, Capan-1, BxPC-3, MIA PaCa-2, Panc10.05, Panc03.27, PANC-1, Capan-2, HPNE (V), IMR-90 were obtained from ATCC. Pa-Tu-8902, Pa-Tu-8988T, YAPC, and Hup T3 were obtained from DSMZ. Human pancreatic pancreatic stellate cells (hPSC) were a generous gift form Rosa Hwang (Hwang et al., 2008). The UM PDA primary cell cultures (UM147, UM5, UM90, and UM19) were obtained from surgically-resected samples and established through murine xenograft (Li et al., 2007). KPC-MT3 murine PDA cell lines were a generous gift from Dr. David Tuveson. All commercial cell lines and UM PDA primary cultures were validated by STR profiling and tested negative for mycoplasma infection (Lonza, LT07-701). Cells were maintained under standard conditions at 37ºC and 5% CO2. Cells were grown either in regular DMEM (GIBCO, #11965) or RPMI (GIBCO, #11875), or in DMEM without cystine (GIBCO, #21013024) or RPMI (GIBCO, A1049101) supplemented with 10% FBS (Corning, 35-010-CV) unless otherwise indicated. Cultures involving inducible short-hairpin mediated knockdown were supplemented with doxycycline-hyclate (Dox) at 1µM/mL (Sigma, D9891) for 5 days prior to experiments.

Lentiviral-mediated shRNA Transduction

Parental PDA cell lines were transduced with lentivirus containing short hairpin RNA plasmids at optimized viral titers. Stable cell lines were established post-puromycin or blasticidin or selection.

Clonogenic Assays

Cells were plated in a 6-well plate in biological triplicates at 300-600 cells per well in 2mL of media. Dox-media were changed every 2 days. Assays were concluded after 10-15 days by fixing in -20ºC cold 100% methanol 10 min and staining with 0.5% crystal violet 20% methanol solution for 15 min. Colonies were quantified using ImageJ or manually counted.

Cell Proliferation Assays

Cells were seeded in a 96-well plate at 1,000 cells per well in 0.1mL of media. Indicated treatments were applied the subsequent day. Media was changed every 2 days. At the indicated time points, media was aspirated and frozen. 100 µL of CyQUANT (Invitrogen,

C7026) to each well for measurements. 10µL of WST-1 reagent directly to the culture media (Sigma, #11644807001). Relative proliferation was determined by the fluorescence intensity at 530nm for CyQuant or 450nm for WST-1 using a SpectraMax M3 plate reader.

Cell Viability Assays

Cells were plated in a 96- or 384-well plate format at 1,000 cells per well Cells were allowed to seed overnight, then treated with compounds at indicated concentrations and for indicated lengths of time. All viability assays utilized the Cell-Titer-Glo 2.0 reagent (Promega, G9243) according to the manufacturer's instructions. Media was aspirated followed by the addition of 100 µL of Cell-Titer-Glo 2.0 reagent to each experimental well. Plates were gently agitated for 10 minutes to promote adequate mixing. Luminescence was subsequently measured using a SpectraMax M3 plate reader.

RNAi

On-TARGET siRNAs smart pools targeting NCOA4 were ordered from Dharmacon. siRNAswere transfected into Pa-Tu-8902 or Mia PaCa-2 iDox-shGOT1 cells previously seeded in 96-well plates using Lipofectamine RNAiMAX (ThermoFisher) per the manufacturer's instructions. MEM-media (ThermoFisher) was used as a mock treatment.

Quantitative RT-PCR

Total RNA was extracted using the RNeasy Mini Kit (Qiagen, 74104) and reverse transcription was performed from 2 µg of total RNA using the iScript cDNA synthesis kit (BioRad,1708890) according to the manufacturer's instructions. Quantitative RT–PCR was performed with Power SYBR Green dye (Thermo, 4367659) using a QuantStudio 3 System (Thermo). PCR reactions were performed in triplicate and the relative amount of cDNA was calculated by the comparative C_T method using an *RPS21* as an endogenous control. RT-PCR was performed in a least 3 biological replicates.

Detection of Reactive Oxygen and Labile Iron by Flow cytometry

Cells were plated in 6-well plates two days before incubation with indicated treatments. Cells were then washed twice with 1x PBS, and stained for 20-30 (Invitrogen, C1430) minutes with 2µM C11-BODIPY (Invitrogen, D3861) or for 10 minutes with 0.2µM

Calcein-AM (Invitrogen, C1430) in phenol red-free DMEM. Cells were co-stained with Sytox-blue (Invitrogen, S34857) to account for cell viability. Following staining, cells were washed twice with PBS, trypsinized (0.25%, Life Technologies, 25200-056), and naturalized with pure FBS at a 1:1 volume. Cells were then collected in 500uL PBS, and moved to round bottom 96-well plates, on ice, for measurements. A minimum of 8000 cells were analyzed per condition. C11-BODIPY and Calcein-AM signals were analyzed in the FITC channel, while Sytox-blue was analyzed in the DAPI channel on a ZE5 Cell analyzer (Bio-Rad). Analysis of data was performed using FlowJo v.10 software. Relative labile iron levels were calculated based on the ratio of Calcein-AM mean fluorescence intensity (MFI) of control vs. dox-treated samples.

Image-Based Detection of Labile Iron

GOT1 was knocked down for 5 days in Pa-Tu-8902 iDox-shGOT1 and seeded at 10,000 cells per well. Cells were treated the following day with Hoechst (1 μg/ml final concentration) and RhoNox-1 (Goryo, GC901) at 500nM for 6 hours then imaged using a Cytation5 Cell Imaging Multi-Mode Reader (BioTek, VT, USA). Hoechst was imaged using a 365 nm LED in combination with an EX 377/50 EM 447/60 filter cube. RhoNox-1 was imaged using a 523 nm LED in combination with an EX 531/40 EM 593/40 filter cube. Image analysis was completed using Gen5 software (BioTek).

Xenograft Studies

Animal experiments were conducted in accordance with the Office of Laboratory Animal Welfare and approved by the Institutional Animal Care and Use Committees of the University of Michigan. NOD scid gamma (NSG) mice (Jackson Laboratory, 005557), 6-8 or 8-10 weeks old of both sexes, were maintained in the facilities of the Unit for Laboratory Animal Medicine (ULAM) under specific pathogen-free conditions. Stable PDA cell lines containing a dox- inducible shRNA against GOT1 were trypsinzied and suspended at 1:1 ratio of DMEM (Gibco, 11965-092) cell suspension to Matrigel (Corning, 354234). 150-200 μL were used per injection. For subcutaneous xenograft studies, $0.5x10^6$ cells were implanted into the lower flanks. Doxycylin (dox) chow (BioServ, F3949) was fed to the +dox groups. Orthotopic tumors were established by injecting $5x10^4$ Pa-Tu-8902 iDox-shGOT1 #1 pFUGW-Firefly Luciferase into 8-10 week old NSG mice. Cysteine-free chow (LabDiet) was customized from Baker Amino Acid

(LabDiet, 5CC7) to remove cysteine and balance protein levels with increased valine and aspartic acid. BSO was delivered in the drinking water at 20 mM. All treatments began on day 7 after implantation.

Subcutaneous tumor size was measured with digital calipers at the indicated endpoints. Tumor volume (V) was calculated as $V = 1/2(\text{length} \times \text{width}^2)$. Bioluminescence (BLI) of orthotopic tumors were measured via IVIS SpectrumCT (PerkinElmer) following an intraperitoneal injection of 100 µL beetle luciferine (40 mg/mL in PBS stock) (Promega, E1605). BLI was analyzed with Living Image software (PerkinElmer). At endpoint, final tumor volume and mass were measured prior to processing. Tissue was either fixed in zinc formalin fixative (Z-fix, Anatech LTD, #174) for >24 hours for histological and/or histochemical analysis, or snap-frozen in liquid nitrogen then stored at -80°C until metabolite or protein analysis.

Western blot analysis

Stable shNT and shGOT1 cells were cultured with or without dox media and protein lysates were collected after five days using RIPA buffer (Sigma, R0278) containing protease inhibitor cocktail (Sigma/Roche, 04 693 132 001). Samples were quantified with Pierce BCA Protein Assay Kit (ThermoFisher, 23225). 10 to 40 µg of protein per sample were resolved on NuPAGE Bis-Tris Gels (Invitrogen, NP0336) and transferred to a Immobilon-FL PVDF membrane (Millipore, IPVH00010). Membranes were blocked in 5% non-fat dry milk in distilled H_2O prior to incubation with the primary antibody. The membranes were washed with TBS-Tween followed by a 1h exposure to the appropriate horseradish peroxidase-conjugated secondary antibody. The membranes were washed in de-ionized water for 15-30 minutes then visualized using a Bio-Rad ChemiDox MP Imaging System (Bio-Rad, 17001402). The following antibodies were used: anti-aspartate aminotransferase (anti-GOT1) at a 1:1,000 dilution (Abcam, ab171939), 1:1,000 dilution Anti-Rabbit LC3 A/B (CST, 12741), 1:1,000 dilution Anti-Rabbit NCOA4 (Bethyl Laboratories, A302-272A), 1:1,000 dilution Anti-Rabbit IRP-2 (Cell Signaling, D6E6W), and loading control vinculin at a 1:1,000 dilution (Cell Signaling, 13901), HSP-90 (Cell Signaling, 4877S), Anti-Rabbit β-Actin (Cell Signaling, 4970L) or GAPDH (Cell Signaling, 2118). Anti-rabbit IgG, HRP-linked (Cell Signaling Technology, 7074) secondary antibody was used at a 1:10,000 dilution.

Histology

Mice were sacrificed by CO_2 asphyxiation followed by tissue harvesting and fixation overnight at room temperature with Z-fix solution (Z-fix, Anatech LTD, #174). Tissues were the processed by using a Leica ASP300S Tissue Processor, paraffin embedded, and cut into 5-µm sections. Immunohistochemistry was performed on Discovery Ultra XT autostainer (Ventana Medical Systems Inc.) and counterstained with hematoxylin. IHC slides were scanned on a Panoramic SCANslide scanner (Perkin Elmer), and then annotation regions encompassing greater than 1mm of tissue were processed using Halo software (Indica Labs).The following antibodies were used for IHC: GOT1 (AbCam, ab171939), Ki-67 (Cell Signaling, 9027), Cleaved Caspase-3 (Cell Signaling, 9664).

Metabolomics

Targeted metabolomics: Cells were plated at 500,000 cells per well in 6-well plates or ~1.5 million cells per 10 cm dish. At the endpoint, cells were lysed with dry-ice cold 80% methanol and extracts were then centrifuged at 10,000 g for 10 min at 4°C and the supernatant was stored at -80°C until further analyses. Protein concentration was determined by processing a parallel well/dish for each sample and used to normalize metabolite fractions across samples. Based on protein concentrations, aliquots of the supernatants were transferred to a fresh micro centrifuge tube and lyophilized using a SpeedVac concentrator. Dried metabolite pellets were re-suspended in 45 µL 50:50 methanol:water mixture for LC–MS analysis. Data was collected using previously published parameters (Yuan et al. 2012) (Lee et al. 2019).

The QqQ data were pre-processed with Agilent MassHunter Workstation Quantitative Analysis Software (B0700). Additional analyses were post-processed for further quality control in the programming language R. Each sample was normalized by the total intensity of all metabolites to scale for loading. Finally, each metabolite abundance level in each sample was divided by the median of all abundance levels across all samples for proper comparisons, statistical analyses, and visualizations among metabolites. The statistical significance test was done by a two-tailed t-test with a significance threshold level of 0.05.

Seahorse Mito Stress Test

MiaPaCa-2 cells were seeded at $2x10^4$ cells/well in 80 µl/well of normal growth media (DMEM with 25 mM Glucose and 2 mM Glutamine) in an Agilent XF96 V3 PS Cell Culture Microplate (#101085-004). To achieve an even distribution of cells within wells, plates were incubated on the bench top at room temperature for 1 hour before incubating at 37ºC, 5% CO2 overnight. To hydrate the XF96 FluxPak (#102416-100), 200 µL/well of sterile water was added and the entire cartridge was incubated at 37'C, no CO2 overnight. The following day, one hour prior to running the assay, 60 µL/well of growth media was removed from the cell culture plate and cells were washed twice with 200 µL/well of assay medium (XF DMEM Base Medium, pH 7.4 (#103575-100) containing 25 mM Glucose (#103577-100) and 2 mM Glutamine (#103579-100)). After washing, 160 µL/well of assay medium was added to the cell culture plate for a final volume of 180 µL/well. Cells were then incubated at 37'C, no CO2 until analysis. Also one hour prior to the assay, water from the FluxPak hydration was exchanged for 200 µL/well of XF Calibrant (#100840-000) and the cartridge was returned to 37'C, no CO2 until analysis. Oligomycin (100 µM), FCCP (100 µM), and Rotenone/Antimycin (50 µM) from the XF Cell Mito Stress Test Kit (#103015-100) were re-constituted in assay medium to make the indicated stock concentrations. 20 µL of Oligomycin was loaded into Port A for each well of the FluxPak, 22 µL of FCCP into Port B, and 25 µL of Rotenone/Antimycin into Port C. Port D was left empty. The final FCCP concentration was optimized to achieve maximal respiration in each condition.

The Mito Stress Test was conducted on an XF96 Extracellular Flux Analyzer and OCR was analyzed using Wave 2.6 software. Following the assay, OCR was normalized to cell number with the CyQUANT NF Cell Proliferation Assay (C35006) from Thermo Fisher according to manufacturer's instructions.

RNA-seq

Pa-Tu-8902 and Mia PaCa-2 iDox-shGOT1 cells were collected in lysis buffer following 5 days of GOT1 knockdown. RNA was isolated using the (QIAGEN) AllPrep DNA/RNA/miRNA Universal Kit according to the manufacturer's instructions. PolyA+, non-strand-specific libraries were prepared by the University of Michigan Sequencing Core, and all samples were sequenced on an Illumina HiSeq 4000.

Statistical Analysis

Statistics were performed using GraphPad Prism 7 (Graph Pad Software Inc). Groups of 2 were analyzed using the unpaired two-tailed Student's t test and comparisons across more than 2 groups were conducted using one-way ANOVA Tukey post-hoc test. All error bars represent mean with standard deviation, unless noted otherwise. A P value of less than 0.05 was considered statistically significant. All group numbers and explanation of significant values are presented within the figure legends.

4.6 Chapter 4 References

1. Halbrook, C. J. & Lyssiotis, C. A. Employing Metabolism to Improve the Diagnosis and Treatment of Pancreatic Cancer. *Cancer Cell* 31, 5–19 (2017).

2. Perera, R. M. & Bardeesy, N. Pancreatic Cancer Metabolism: Breaking It Down to Build It Back Up. *Cancer Discov* 5, 1247–1261 (2015).

3. Son, J. *et al.* Glutamine supports pancreatic cancer growth through a KRAS-regulated metabolic pathway. *Nature* 496, 101–105 (2013).

4. Anglin, J. *et al.* Discovery and optimization of aspartate aminotransferase 1 inhibitors to target redox balance in pancreatic ductal adenocarcinoma. *Bioorganic & Medicinal Chemistry Letters* 28, 2675–2678 (2018).

5. Holt, M. C. *et al.* Biochemical Characterization and Structure-Based Mutational Analysis Provide Insight into the Binding and Mechanism of Action of Novel Aspartate Aminotransferase Inhibitors. *Biochemistry* 57, 6604–6614 (2018).

6. Sun, W. *et al.* Aspulvinone O, a natural inhibitor of GOT1 suppresses pancreatic ductal adenocarcinoma cells growth by interfering glutamine metabolism. *Cell Commun. Signal* 17, 111 (2019).

7. Yoshida, T. *et al.* A covalent small molecule inhibitor of glutamate-oxaloacetate transaminase 1 impairs pancreatic cancer growth. *Biochemical and Biophysical Research Communications* 522, 633–638 (2020).

8. Zecchini, V. & Frezza, C. Metabolic synthetic lethality in cancer therapy. *Biochimica et Biophysica Acta (BBA) - Bioenergetics* 1858, 723–731 (2017).
9. Dixon, S. J. *et al.* Ferroptosis: An Iron-Dependent Form of Nonapoptotic Cell Death. *Cell* 149, 1060–1072 (2012).

10. Stockwell, B. R. *et al.* Ferroptosis: A Regulated Cell Death Nexus Linking Metabolism, Redox Biology, and Disease. *Cell* 171, 273–285 (2017).

11. Mancias, J. D., Wang, X., Gygi, S. P., Harper, J. W. & Kimmelman, A. C. Quantitative proteomics identifies NCOA4 as the cargo receptor mediating ferritinophagy. *Nature* 509, 105–109 (2014).

12. Alvarez, S. W. *et al.* NFS1 undergoes positive selection in lung tumours and protects cells from ferroptosis. *Nature* 551, 639–643 (2017).

13. Gao, M. *et al.* Ferroptosis is an autophagic cell death process. *Cell Res.* 26, 1021–1032 (2016).

14. Li, C. *et al.* Identification of pancreatic cancer stem cells. *Cancer Res.* 67, 1030–1037 (2007).

15. Nelson, B. S. *et al.* Tissue of origin dictates GOT1 dependence and confers synthetic lethality to radiotherapy. *Cancer Metab* 8, 1 (2020).

16. Gorrini, C., Harris, I. S. & Mak, T. W. Modulation of oxidative stress as an anticancer strategy. *Nature Reviews Drug Discovery* 12, 931–947 (2013).

17. Kamphorst, J. J. *et al.* Human Pancreatic Cancer Tumors Are Nutrient Poor and Tumor Cells Actively Scavenge Extracellular Protein. *Cancer Res* 75, 544–553 (2015).

18. Sullivan, M. R. *et al.* Quantification of microenvironmental metabolites in murine cancers reveals determinants of tumor nutrient availability. *eLife* 8, e44235 (2019).

19. Griffith, O. W. Mechanism of action, metabolism, and toxicity of buthionine sulfoximine and its higher homologs, potent inhibitors of glutathione synthesis. *J. Biol. Chem.* 257, 13704–13712 (1982).

20. Harris, I. S. *et al.* Deubiquitinases Maintain Protein Homeostasis and Survival of Cancer Cells upon Glutathione Depletion. *Cell Metabolism* 29, 1166-1181.e6 (2019).

21. Yang, W. S. *et al.* Regulation of ferroptotic cancer cell death by GPX4. *Cell* 156, 317–331 (2014).

22. Gaschler, M. M. *et al.* FINO2 Initiates Ferroptosis Through GPX4 Inactivation and Iron Oxidation. *Nat Chem Biol* 14, 507–515 (2018).

23. Thomas, F. *et al.* Calcein as a fluorescent probe for ferric iron. Application to iron nutrition in plant cells. *J. Biol. Chem.* 274, 13375–13383 (1999).

24. Hirayama, T., Okuda, K. & Nagasawa, H. A highly selective turn-on fluorescent probe for iron(II) to visualize labile iron in living cells. *Chem. Sci.* 4, 1250–1256 (2013).

25. Torti, S. V. & Torti, F. M. Iron and cancer: more ore to be mined. *Nat. Rev. Cancer* 13, 342–355 (2013).

26. Muckenthaler, M. U., Rivella, S., Hentze, M. W. & Galy, B. A Red Carpet for Iron Metabolism. *Cell* 168, 344–361 (2017).

27. Forgac, M. Vacuolar ATPases: rotary proton pumps in physiology and pathophysiology. *Nature Reviews Molecular Cell Biology* 8, 917–929 (2007).

28. Perera, R. M. *et al.* Transcriptional control of autophagy-lysosome function drives pancreatic cancer metabolism. *Nature* 524, 361–365 (2015).

29. Kimmelman, A. C. & White, E. Autophagy and Tumor Metabolism. *Cell Metab* 25, 1037–1043 (2017).

30. Dixon, S. J. *et al.* Ferroptosis: an iron-dependent form of nonapoptotic cell death. *Cell* 149, 1060–1072 (2012).

31. Gao, M. *et al.* Role of Mitochondria in Ferroptosis. *Mol. Cell* 73, 354-363.e3 (2019).

32. Gao, M., Monian, P., Quadri, N., Ramasamy, R. & Jiang, X. Glutaminolysis and Transferrin Regulate Ferroptosis. *Molecular Cell* 59, 298–308 (2015).

33. Zhang, K. *et al.* miR-9 regulates ferroptosis by targeting glutamic-oxaloacetic transaminase GOT1 in melanoma. *Molecular Carcinogenesis* 57, 1566–1576 (2018).

34. Fujimaki, M. *et al.* Iron Supply via NCOA4-Mediated Ferritin Degradation Maintains Mitochondrial Functions. *Mol. Cell. Biol.* 39, (2019).

35. Yambire, K. F. *et al.* Impaired lysosomal acidification triggers iron deficiency and inflammation in vivo. *eLife* 8, e51031 (2019).

36. Weber, R. A. *et al.* Maintaining Iron Homeostasis Is the Key Role of Lysosomal Acidity for Cell Proliferation. *Molecular Cell* 77, 645-655.e7 (2020).

37. Hughes, C. E. *et al.* Cysteine Toxicity Drives Age-Related Mitochondrial Decline by Altering Iron Homeostasis. *Cell* 180, 296-310.e18 (2020).

38. Doll, S. *et al.* ACSL4 dictates ferroptosis sensitivity by shaping cellular lipid composition. *Nature Chemical Biology* 13, 91–98 (2017).

39. Kagan, V. E. *et al.* Oxidized arachidonic and adrenic PEs navigate cells to ferroptosis. *Nature Chemical Biology* 13, 81–90 (2017).

40. Spangler, B. *et al.* A Novel Tumor-Activated Prodrug Strategy Targeting Ferrous Iron Is Effective in Multiple Preclinical Cancer Models. *J. Med. Chem.* 59, 11161–11170 (2016).

41. Schoenfeld, J. D. *et al.* O2·− and H2O2-Mediated Disruption of Fe Metabolism Causes the Differential Susceptibility of NSCLC and GBM Cancer Cells to Pharmacological Ascorbate. *Cancer Cell* 31, 487-500.e8 (2017).

42. Deu, E. *et al.* Ferrous iron-dependent drug delivery enables controlled and selective release of therapeutic agents in vivo. *PNAS* 110, 18244–18249 (2013).

Chapter 5. Conclusions and Future Directions

5.1 Conclusions and Future Directions

The work presented here contributes to the growing fields of mass spectrometry metabolomics, ferroptosis, and pancreatic cancer metabolism. Our meta-analysis provides insight into metabolite stability and metabolite dynamics. These results are a valuable reference for ongoing metabolomics method development efforts.

We identified several metabolic dependencies in pancreatic cancer by applying metabolomics and chemical biology methods. Our work revealed pancreatic cancers are vulnerable to ferroptosis- a non-apoptotic, oxidative, iron-dependent form of cell death. Our work provides new mechanistic insights into the metabolic regulation of ferroptosis and establishes new methods to characterize ferroptosis *in vivo*. These findings answer several long-standing questions within the field of ferroptosis, and provide new tools to study ferroptosis in animal development and physiology.

Traditional apoptosis-inducing drugs have been ineffective in pancreatic cancer. By contrast, our work suggests triggering ferroptosis could be an effective alternative therapeutic strategy. Our work reveals several therapeutic strategies harnessing ferroptosis for therapeutic benefit.

Identification of Stable and Dynamic Metabolites

In chapter 2, we conducted a meta-analysis using 42 data sets originating from diverse experimental conditions. Our systematic analysis revealed insights into reproducibility and metabolite dynamics, while nominating methionine, phenylalanine, and taurine as high confidence metabolites. These metabolites should be used as quality control references for future metabolomics experiments.

Our abundance and variability analysis revealed several highly dynamic metabolites. Metabolomics campaigns have traditionally sought to identify biochemical changes in response to experimental perturbations or identifying disease biomarkers.

Researchers are now beginning to study the roles that individual metabolites play beyond intermediary metabolism. A new field of “activity metabolomics” aims to characterize the interplay between metabolism, gene expression, and disease[1]. In line with this idea, our studies found that highly dynamic metabolites serve signaling roles in addition to biosynthesis and bioenergetics.

We characterized amino acids, nucleotides, and glycolytic intermediates as highly dynamic. These metabolite pools are considered dynamic, reflecting their universal role in the biosynthesis cellular building blocks[2]. These metabolites participate in signaling through post-translational modification (PTM) or allosteric regulation[1]. For example, we found that hexosamine biosynthesis (HBP) metabolites were highly dynamic. The HBP is a branch of glycolysis that produces uridine diphosphate N-acetyl glucosamine (UDP-GlcNAc), which is used for glycosylation, a post-translational modification. UDP-GlcNAc is considered a marker of cellular nutrient status, by integrating carbon from nucleotide, glucose, and acetyl-CoA and glutamine nitrogen[3]. The O-GlcNAcylation (PTM) regulates several transcription factors, thus serving as one mechanism by which cells integrate nutrient status with gene expression[3].

TCA cycle metabolites were highly dynamic in our analysis. Over the last decade, published reports have implicated TCA cycle metabolites in modulating signaling, cell fate, and cancer phenotypes, in addition to biosynthetic and bioenergetic contrabutions[4,5]. For example, Somatic mutations in metabolic enzymes such as IDH1or IDH2 promote the accumulation (D)-2-hydroxyglutarate (2HG) that inhibits α-ketoglutarate-dependent enzymes to regulate gene expression[5]. High levels of fumarate and succinate can inhibit the activity of histone lysine demethylases and dramatically reprogram gene expression[4]. Loss-of-function mutations affecting succinate dehydrogenase (SDH) complex subunits and fumarate hydratase (FH) have been identified in cancers. Thus, highly dynamic metabolites engage in post-translational modification, signaling, and regulate gene expression.

Our systematic identification of dynamic metabolites raises three considerations for future metabolomics studies. First, metabolomics experiments should consider how metabolite dynamics could impact the experimental readout, as the dynamic metabolites we describe here will be highly variable. Caution should be taken when

interpreting the metabolite levels within the dynamic metabolite class, and orthogonal methods of detection should be used as secondary confirmation. Second, future metabolomics experiments should control for the signaling effects of dynamic metabolites. One way to achieve this is to integrate metabolite signaling and gene-modulatory activities to future data analysis pipelines. Incorporating these suggestions could lead to a more robust interpretation of metabolomics data and reveal novel metabolic signaling paradigms. Overall, future metabolomics methods should include our growing understanding of metabolite signaling.

Insights into the Metabolic Regulation of Ferroptosis

Metabolism and ferroptosis are intertwined. Seminal work by Dixon *et al.* established the relationship between cystine, iron, and lipid peroxidation[6]. Building upon this finding, Yang *et al.* proposed the ultimate fate of exogenous cystine was reduced glutathione (GSH), which serves as an essential co-factor for the lipid ROS detoxifying enzyme GPX4 **(Figure 41)**[7]. Building off of these observations, we hypothesized that the fate exogenous cystine in PDA was also GSH[8]. To our surprise, we found that inhibiting GSH synthesis was insufficient to induce ferroptosis, agreeing with previous data[9].

Employing [U-13C]-cystine to study its fate, we found that it rapidly labeled Coenzyme-A (CoA). Inhibiting CoA synthesis sensitized PDA to BSO-mediated ferroptosis. Previous studies have demonstrated that GSH synthesis inhibition can prevent tumor initiation in multiple genetically engineered mouse models[10], but has little effect on established cancer cells and tumors[9,10]. It should be noted that the thioredoxin (Trx) pathway has been shown to support the survival of cells upon GSH depletion. Combined inhibition of these pathways also induces cell death[10,11]. Recent reports suggest that thioredoxin inhibition induces ferroptosis in breast cancer cells[12]. Thus glutathione, thioredoxin, and CoA are three redox nodes that protect cancer cells against ferroptosis **(Figure 41)**.

While our data suggest mono-unsaturated fatty acids are potential fates of CoA, future work is needed to identify the metabolic contribution of CoA to ferroptosis sensitivity. Metabolites derived from CoA such as Coenzyme Q10 (CoQ_{10})[13–15], mono-unsaturated fatty acids (MUFAs)[16], and poly-unsaturated fatty acids (PUFAs)[17,18],

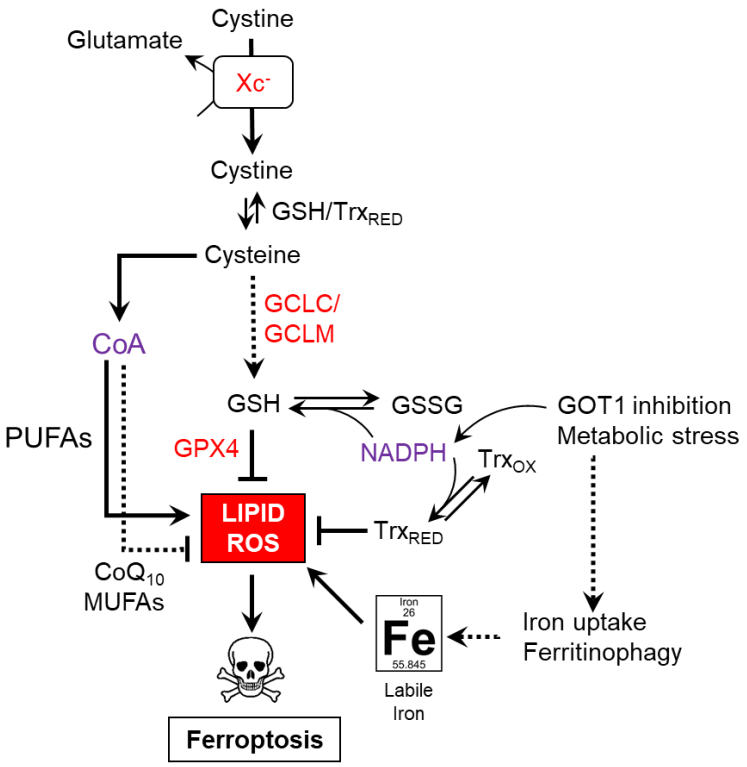

Figure 41. Metabolic regulation of ferroptosis in pancreatic cancer. Key regulatory enzymes are depicted in red, while key metabolic co-factors are labeled in purple.

dictate sensitivity to ferroptosis **(Figure 41)**.The fate of CoA in PDA cells could be tested by radioactive isotope tracing methods. Employing a [U]-^{14}C-pantothenate analog, we would expect to see radiolabeling of CoA and acetyl-CoA. CoA is required for the activation and incorporation of dietary-derived fatty acids into cell membranes. Acetyl-CoA is a significant intermediate for the mevalonate pathway and fatty acid synthesis. Acyl-coenzyme synthetase long-chain 3 (ACSL3) converts dietary MUFAs to fatty acyl-CoAs. Fatty acyl-CoAs are incorporated into glycerophospholipids, which are significant components in the cell membrane. Dietary MUFAs have been shown to incorporate into cell membranes and prevent ferroptosis[16]. ^{14}C-labeling of MUFAs would demonstrate that this is a direct fate of CoA. By contrast, the enzyme ACSL4 preferentially activates scavenged PUFAs for incorporation into cell membrane phospholipids **(Figure 41)**. Deletion of ACSL4 can prevent ferroptosis[17]. ^{14}C-label incorporated into PUFAS and MUFAs would argue against the preferential activation of MUFAs by CoA. Instead, this potential observation would suggest that CoA could

contribute to alternative ferroptosis suppressing pathways. The availability of MUFAs versus PUFAs would dictate sensitivity to ferroptosis.

Previous data indicate that oncogenic KRAS regulates the transcription of steroids and glycerolipids **(Figure 42)**[19]. Steroids are downstream products of the mevalonate pathway. The mevalonate pathway also contributes to CoQ_{10} synthesis, which suppresses ferroptosis. Previous data have shown cerivastatin, which inhibits the rate-limiting enzyme of the mevalonate pathway, augments ferroptosis sensitivity[15]. Conversely, supplementing cells with mevalonate pathway intermediates blunts ferroptosis sensitivity, suggesting a relationship between the mevalonate pathway and ferroptosis[15]. KRAS also regulates the transcription of glycerolipids[19]. Two forms of glycerolipids include glycerophospholipids and triacylglycerols. Glycerophospholipids are building blocks for cell membranes, while triacylglycerols are used for fatty acid storage and lipid droplets **(Figure 42)**. Hypoxic and RAS transformed cells bypass *de novo* lipid synthesis and actively scavenge serum lysophospholipids[20], suggesting PDA may engage in phospholipid scavenging. KRAS may regulate two pathways that influence ferroptosis susceptibility.

Overall, we show that CoA coordinates with GSH, and potentially, Trx to prevent ferroptosis. The fate of CoA could be directly addressed via radioactivity labeling. Based on our previous data, we expect the incorporation of the radiolabel into intermediates of the mevalonate pathway, mono-unsaturated fatty acids, and glycerophospholipids. The mevalonate pathway and glycerolipid metabolism are transcriptionally regulated by KRAS, suggesting ferroptosis could be a KRAS vulnerability.

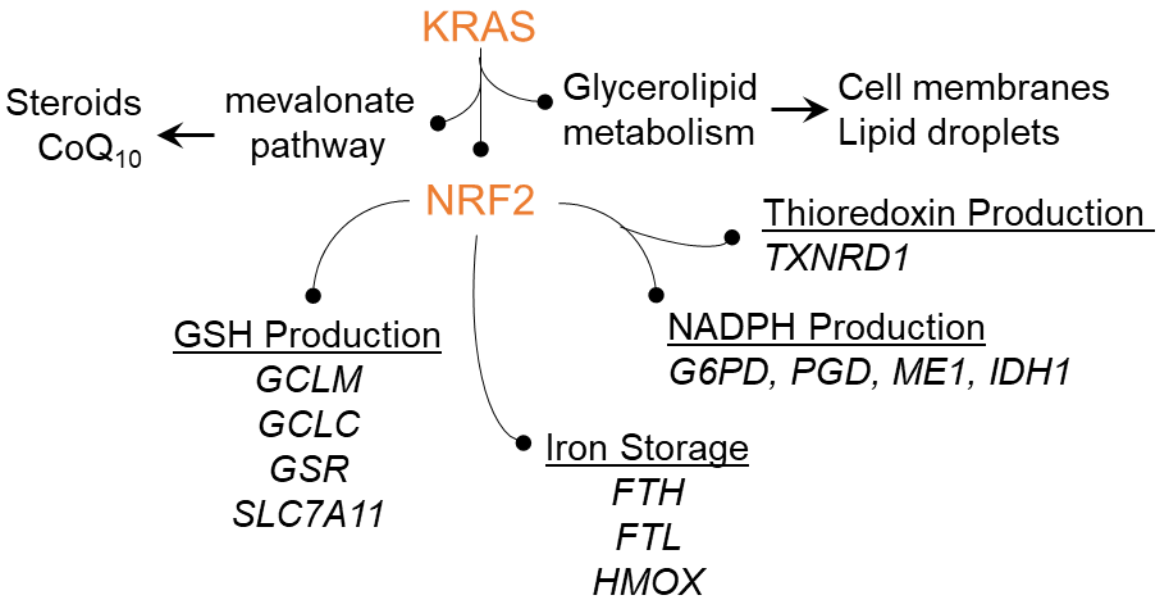

Figure 42. Regulation of ferroptosis sensitivity by KRAS and NRF2.

A Potential Role for Sulfur Metabolism in PDA Redox and Energetics

Alternative methods of cysteine production exist in addition to system x_c^- and may contribute to ferroptosis, redox balance, and energetics. Cells can synthesize cysteine *de novo* from serine and methionine using the transsulfuration pathway **(Figure 43)**. The transsulfuration pathway is active in several tissues, including the liver, brain, and pancreas[21]. Zhu et al. recently showed that some cancer cells require this pathway for viability under cysteine-limited conditions, where transsulfuration activity was dependent on homocysteine[22]. Using ^{13}C-labeled methionine and LC-MS, we traced the fate of methionine into the transsulfuration pathway intermediates in two PDA cell lines **(Figure 43)**. The cysteine is formed from cystathionine through the enzyme γ-cystathionase (CSE), where alpha-ketobutyrate is a byproduct. We would expect to see an [M+4] alpha-ketobutyrate if this pathway was active. We observed no [M+4] alpha-ketobutyrate labeling, contrasting labeled homocysteine and cystathionine. Moreover, the co-inhibition of Xc^- and the transsulfuration inhibitor propargylglycine (PPD) was not synergistic **(Figure 44)**. An orthogonal approach to measuring transsulfuration activity is to measure the incorporation of ^{14}C-labeled carbon from methionine into GSH.

Radiolabeling would be a more sensitive method to detect transsulfuration activity than our previous LC-MS based approach.

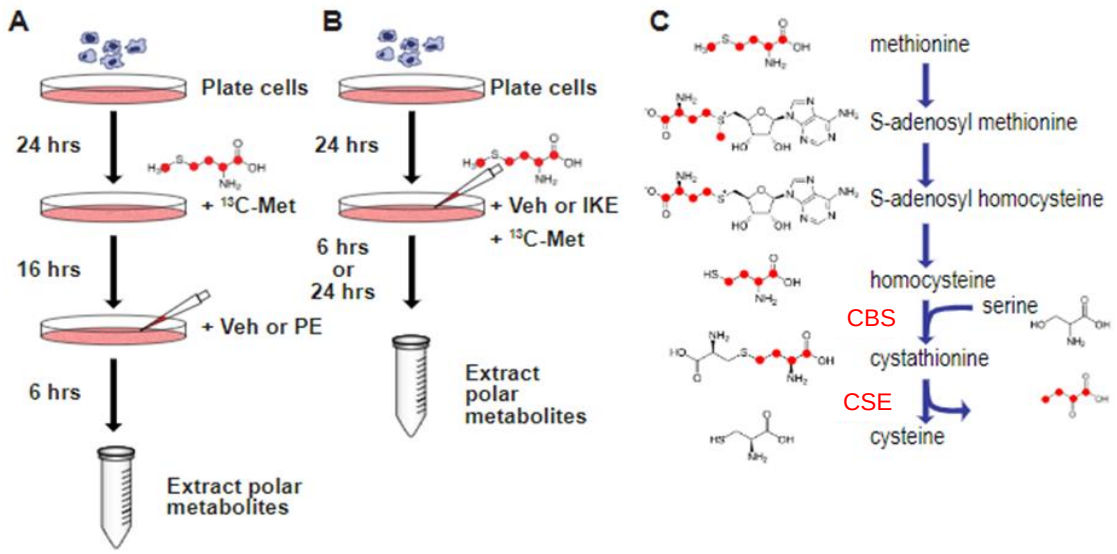

Figure 43. Methionine tracing through the transsulfuration pathway.
Figure adapted from Dr. Mike Badgley.

Select tissues and certain cancer cell lines can utilize the transsulfuration pathway, but our preliminary data suggests PDA cell cultures do not. Still, this analysis was conducted using a single PDA cell line, MIA PaCa-2. Future work would need to examine transsulfuration activity using isotope tracing methods across a broader panel of cell lines and primary patient specimens. These studies are of interest since the transsulfuration pathway can support cancer growth[22].

Cysteine and methionine participate in diverse biochemical reactions to produce metabolites and enzymatic co-factors. Cysteine metabolism produces Fe-S clusters, taurine, and hydrogen sulfide (H_2S), in addition to CoA and GSH. Fe-S clusters are essential redox metabolic co-factors, while H_2S is a gas with signaling and redox properties. Methionine metabolism yields S-adenosylmethionine (SAM), which is used in methylation reactions and polyamine synthesis. One could employ ^{35}S-labeled methionine/cysteine to map the contribution of these metabolites to sulfur metabolism in PDA. A time-course experiment could also be taken to measure the metabolic flux of sulfur labeling. Differences in flux would indicate metabolic utilization and identify metabolic enzymes for further interrogation. This analysis would be limited to: taurine,

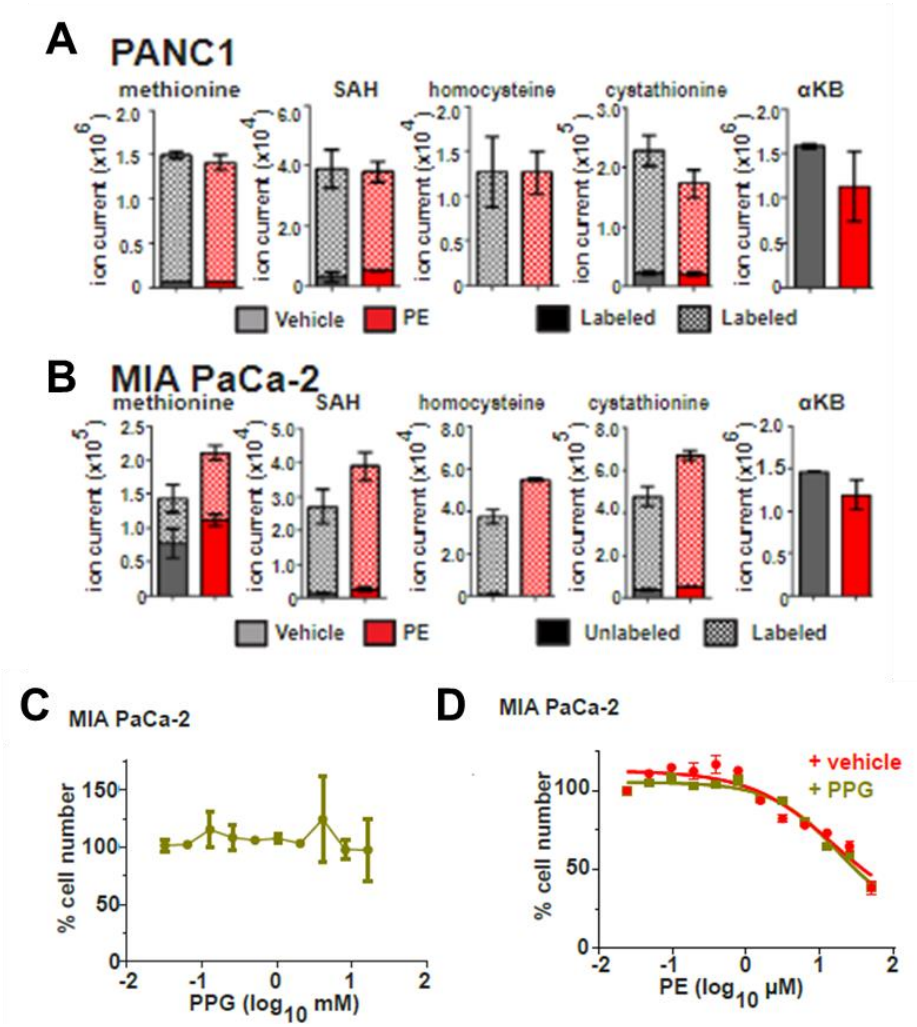

Figure 44. Utilization of the transsulfuration pathway in PDA cells.
Data collected in collaboration with Dr. Li Zhang, Zach Tolstyka, and Mike Badgley. Figure adapted from Dr. Mike Badgley.

CoA, GSH, SAM, polyamines, and N-formyl methionine since these metabolites could be isolated and quantified by liquid chromatography. This analysis could reveal new metabolic dependencies in PDA since sulfur-containing compounds facilitate diverse biochemical functions.

Commonly used sulfur-containing antioxidants can have broad effects. For example, n-acetyl cysteine (NAC) is typically used as a cytoprotective agent to blunt ROS. The current mechanism of action posits that NAC is converted to GSH, where it is then used as an antioxidant. We show that NAC or GSH supplementation prevents ferroptosis following Xc^- inhibition and rescues proliferation and colony formation in PDA cell lines[23]. We also show that NAC, GSH, and the reducing agent β-mercapto

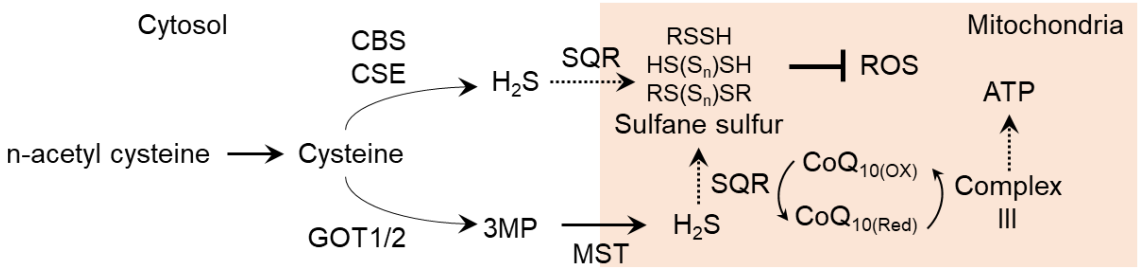

Figure 45. Production and fate of H_2S derived from cysteine.

ethanol prevent GOT1-mediated ferroptosis. A recent study proposed an alternative mechanism where NAC is converted to H_2S through cysteine catabolism **(Figure 45)**. Subsequent mitochondrial oxidation of H_2S leads to sulfane sulfur, which has antioxidant activity[24].

GOT1 and GOT2 contribute to H_2S generation through transamination of cysteine to form 3-mercapto pyruvate (3MP) **(Figure 45)**. The enzyme 3-mercapto pyruvate sulfurtransferase (MST) produces H_2S from 3MP. This mechanism seems operative in humans, as a genetic deficiency in MST leads to β-mercaptolactate cysteine disulfiduria (OMIM: 249650), a rare metabolic disorder. The mitochondrial enzyme sulfide: quinone reductase (SQR) can then react with GSH and H_2S to produce GSSH and, ultimately, sulfane sulfur[24,25]. SQR reduces mitochondrial CoQ_{10}, which can support mitochondrial metabolism and ferroptosis protection. Moreover, it has been shown that reducing agents, such β-mercapto ethanol, can release from sulfane sulfur[25]. Thus, there are several non-canonical effects of commonly used antioxidants, and these areas of study represent new avenues of redox biology.

According to this model, Cysteine, NAC, GSH, and reducing agents can contribute to the production of sulfane sulfur and support mitochondrial metabolism. Future studies can determine if H_2S generation essential for PDA growth and viability by depriving cells of cystine and testing if 3MP or Na_2S, an H_2S source, can prevent ferroptosis. If H_2S derived from GOT1 or GOT2 contribute to PDA proliferation and growth, then 3MP or Na_2S should rescue the anti-proliferative effects of GOT1 or GOT2 knockdown. To determine the extent to which this mechanism contributes to mitochondrial metabolism, 3MP or Na_2S can be supplemented to GOT1 knockdown cells. Because GOT1 knockdown decreases basal oxygen consumption rate (OCR), restoring OCR using 3MP or Na_2S would indicate that the conversion of cysteine to H_2S

by the GOT enzymes are additional factors regulating mitochondrial metabolism. Cysteine and the GOT1 could play roles in PDA sulfur metabolism.

The Role of GOT1 in PDA and Ferroptosis

Our data reveal one of the downstream effects of GOT1 inhibition is iron release and mitochondrial inhibition, where these metabolic adaptions can sensitize PDA cells to ferroptosis. MDH1 or ME1 inhibition failed to phenocopy the GOT1 effect **(Figure 46)**. General anti-proliferative conditions did not uniformly impact ferroptosis sensitivity **(Figure 47)**. By contrast, iron and, to a lesser extent, mitochondrial inhibitors

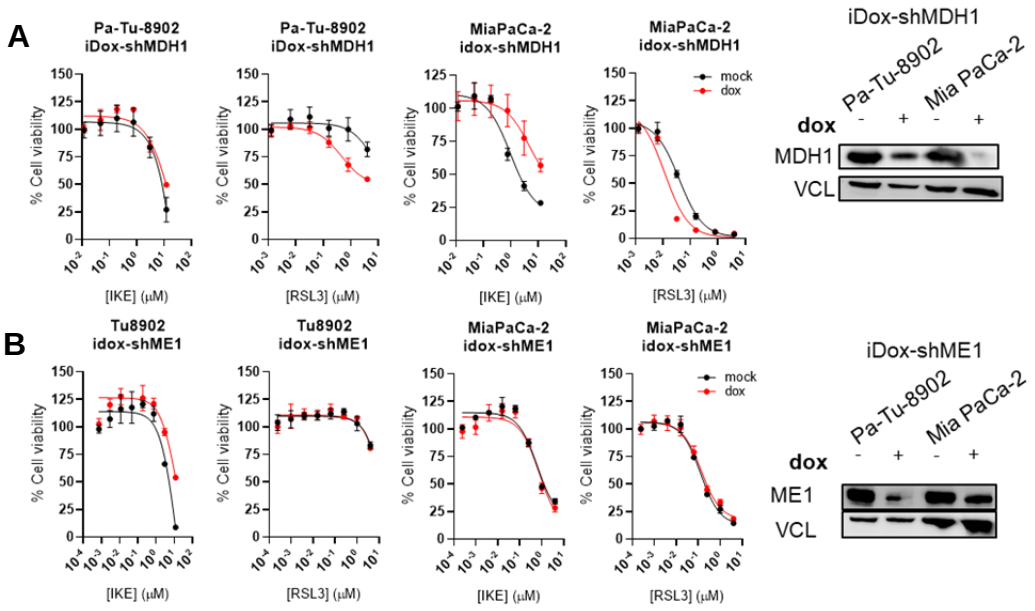

Figure 46. Inhibiting enzymes downstream of GOT1 do not augment ferroptosis.
A-B) Effect of MDH1 (A) or ME1 (B) knockdown on ferroptosis sensitivity.

augmented ferroptosis sensitivity **(Figure 48)**. GOT1 inhibition modulates ferroptosis sensitivity in PDA by promoting labile iron release and inhibiting the mitochondria.

Labile iron release could occur following mitochondrial inhibition. While future work is needed to show this is the case in PDA, several groups have shown iron released by lysosomes and endosomes support mitochondrial function[53–56]. Loss of these activities is implicated in age-related disorders and neurodegenerative disease[57]. Organelle proximity and communication might be a critical mediator of this process, where Hamdi *et al*. demonstrated direct contact between the endosome and mitochondria of eythroid cells[58]. While we and others suggest labile iron can be

harnessed therapeutically[59–61], the mechanisms of iron release and physiological roles of labile iron in cancer remain open questions.

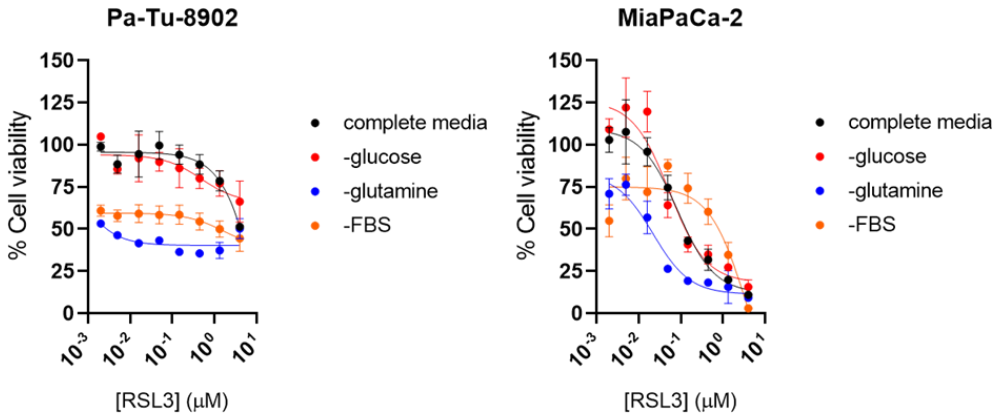

Figure 48. Growth suppressing conditions do not uniformly augment ferroptosis.

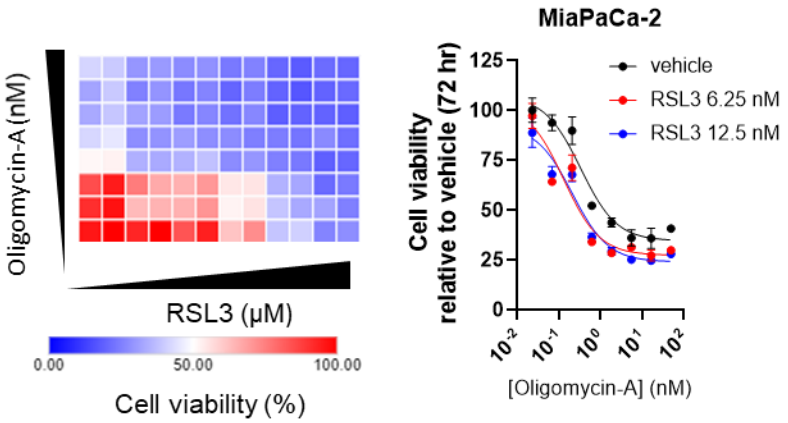

Figure 48. Mitochondrial inhibition augments ferroptosis in an additive manner.

The links between mitochondria and ferroptosis remain open questions[26,27]. Patients with mitochondrial disease have elevated levels of toxic byproducts of lipid ROS, such as malondialdehyde and 4-hydroxynonenal, which potentiate ferroptosis[49]. Moreover, GPX4 is induced during the PGC-1α transcriptional program for mitochondrial biogenesis[50], suggesting a potential relationship where OXPHOS activity is met with an increased need for GPX4[27,51]. GPX4 deletion or pharmacological inhibition is synthetic lethal with oligomycin. Mitochondrial GPX4 expression rescues this effect, suggesting that the mitochondria are a vital lipid peroxidation site[51]. This relationship seems operative in humans, as patients harboring mitochondrial defects

showed higher GPX4 protein levels[52]. Our data show GOT1 inhibition suppresses mitochondrial metabolism and that inhibiting mitochondrial complex I and V augments RSL3 sensitivity. Mitochondrial inhibition is an additional factor by which GOT1 loss promotes ferroptosis sensitivity in PDA.

The role of GOT1 in ferroptosis has been the subject of previous studies. Our data lie in contrast to some previous work, which have suggested that GOT1 inhibition protects cells from ferroptosis by blocking mitochondrial metabolism[26–28]. The differences in these studies likely reflect how tissue of origin influences metabolism and ferroptosis sensitivity. Our studies utilized pancreatic cancer cell lines, were conflicting studies used sarcoma cell lines. Thus, tissue of origin effects could explain these differences. Moreover, these conflicting studies rely on the cell line HT-1080, known to harbor IDH1 mutations[26–28]. As previously discussed, IDH mutations can alter gene expression by inhibiting demethylase enzymes. It is unclear how these mutations influence gene expression, the metabolic utility of GOT1, or labile iron release.

GOT1 Pathway Dependence

Not all KRAS mutant cell lines are dependent on GOT1. We found that colorectal cancer and some PDA cell lines are highly resistant to GOT1 inhibition and seemingly bypass GOT1 for redox balance[29]. Resistant CRC and PDA cell lines could bypass GOT1 through the Citrate Shuttle and reductive carboxylation **(Figure 49)**. Reductive carboxylation has been shown to support cancer cell growth in cells with defective mitochondria[30,31] and support redox homeostasis in lung cancer cells[32].

Here, citrate is released from the mitochondria to the cytosol and converted to oxaloacetate and acetyl-CoA via ATP-Citrate Lyase (ACL). Oxaloacetate is then oxidized to malate by malate dehydrogenase (MDH1), and malate is oxidized by malic enzyme 1 (ME1) to form pyruvate and NADPH. This hypothesis could be tested pharmacologically using the ACL inhibitor, NDI-091143. If this pathway is compensating for GOT1, we would expect GOT1 and ACL inhibition to synergize. The relative contribution of reductive carboxylation in GOT1-resistant cell lines can be measured via [U]-^{13}C glutamine stable isotope tracing **(Figure 49)**. Our previous data show GOT1-resistant CRC cell lines have higher glutamine-derived M+3 citrate and malate, suggesting more reductive carboxylation under basal conditions[29]. Moreover, GOT1

knockdown led to lower M+3 malate suggesting a compensatory response. Additional controls should incorporate the same [U]-^{13}C glutamine tracing strategy following ME1 knockdown. Here we would expect higher glutamine-derived M+3 malate following ME1 inhibition. Reductive carboxylation may bypass GOT1 dependence.

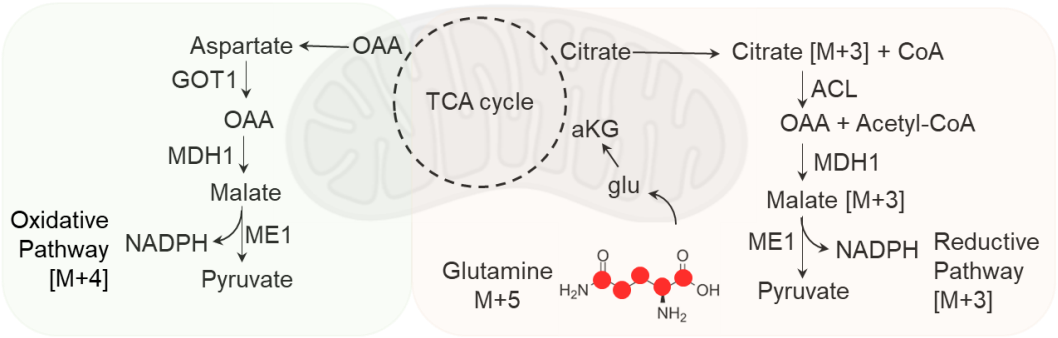

Figure 49. Reductive and oxidative fates of glutamine metabolism.

Role of GOT1 in PDA Progression and Normal Physiology

The role of GOT1 in cancer cells is to contribute to redox balance[20,29], mitochondrial metabolism, and aspartate synthesis[31,33]. Which of these metabolic products is required for cancer progression or growth is unknown. Our lab has generated an adult conditional knockout mouse model (UBC-CreERT2+; GOT1f/f). To study the role of GOT1 in PDA progression, GOT1 conditional mice can be crossed with conditional KRAS gain of function mice with a pancreas-specific promoter (FSF-Ptf1aFlp/+; LSL-KRAS^{G12D}). Acinar cells in the pancreas expressing mutant KRAS form tumors after 12-15 months unless challenged with pancreatitis. Thus, this long latency period offers a window to identify if GOT1 accelerates PDA progression. Conversely, GOT1 inhibition in the context of pancreatitis would test if GOT1 blunts PDA progression. Thus, crossing the GOT1 adult conditional mouse with a pancreas-specific KRAS adult conditional mouse would allow one to study the contribution of GOT1 to PDA progression.

The activation of immune cells following antigen recognition is characterized by the rapid proliferation of helper and effector T cells, where metabolism supports these processes[34]. GOT1 is an essential aspartate generating enzyme where aspartate contributes to numerous metabolic pathways in addition to protein synthesis. Aspartate is vital for rapidly proliferating cancer cells[33,33], and rapidly proliferating T cells could

require aspartate. The carbon backbone of aspartate is needed for nucleotide synthesis, asparagine synthesis, and the malate-aspartate shuttle **(Figure 49)**. The malate-aspartate shuttle is required for CD4 T cell activation and differentiation, where the deletion of any of these enzymes suppresses IFNγ cytokine production in activated Th1 cells[35]. Targeting either mitochondrial or the cytosolic isoform of MDH1 in CD4 T cells inhibited mitochondrial respiration, similar to what we had observed in cultured PDA cells. Likewise, CD8 T cells could require GOT1 for activation and differentiation. To test this hypothesis we could cross our GOT1f/f mice with CD8-Cre mice. The resulting mouse model would allow us to knockout GOT1 in CD8 T cells. Based on previous studies, we expect GOT1 to blunt a CD8 T cell response to proliferative stimuli, e.g., anti-CD3 coated beads. How metabolism regulates the function of effector T cells is a major focus of the growing immunometabolism field.

GOT1 Inhibitors

We and others have identified several molecules that can serve as leads for more potent GOT1 inhibitors[36–39], still, identifying a potent and selective GOT1 inhibitor has been challenging. These inhibitors target the transaminase active site, which is highly conserved, thus preventing GOT1 selectivity. The active site is highly charged, polar, and specially constrained by a pyridoxal phosphate co-factor[37]. Thus, the nature of the active site prevents the binding of cell-permeable ligands[36].

One potential strategy to overcome these limitations is to identify allosteric inhibitors. Allosteric sites are chemically and functionally distinct from the enzyme active sites. Active sites tend to be small, polar, and include metal ions such that small molecules targeting these sites will mirror these chemical properties[40]. By contrast, allosteric sites tend to contain more hydrophobic residues than catalytic sites, making these sites amenable to drug-like molecules. Inhibition of conserved active sites can lead to off-target toxicity. Allosteric sites have evolved to adapt to their environment and are specific to the protein of interest. Hence, targeting allosteric sites would minimize the potential for off-target engagement and improve drug safety[40]. Allosteric targeting has also revealed strategies to enhance the tractability of traditionally “undruggable” targets[41–43]. While targeting allosteric sites is an attractive strategy, an allosteric pocket is not known for GOT1.

Identifying covalent ligands is an orthogonal approach to active site or allosteric inhibition. Several groups have reported fragment libraries targeting electrophilic residues on the surface of proteins[44], thus enabling a reactivity-based method for identifying ligandable hot spots on GOT1. Probe libraries have been developed against cysteine, methionine, lysine, and tyrosine[45–48]. The application of these probes has revealed novel targets and ligands through proteome-wide screens, where cysteine has been the most studied target. GOT1 contains three cysteine residues, offering potential opportunities for covalent attachment. While identifying potent and selective inhibitors of GOT1 has been challenging, synthetic allostery and covalent ligation are promising orthogonal strategies to meet this goal.

In vivo Characterization of Ferroptosis

Ferroptosis is a nascent and exciting field for which discoveries into the mechanistic details and roles in physiology and pathophysiology are being described near daily. Regulated forms of cell death involve the activation and assembly of molecular machinery that relays death signals. Regulated cell death include apoptosis, necroptosis, and pyroptosis. Regulated cell death pathways play a physiological role in development, tissue repair, and immune regulation. Ferroptosis plays roles in pathological situations including, ischemia-reperfusion injury[62] and glutamate-induced excitotoxicity in the brain[6]. Still, a role for ferroptosis in development has not been proposed.

Detailed methods to characterize ferroptosis *in vivo* has been lacking. Early studies have implicated ferroptosis in pathological conditions by employing conditional mouse models of GPX4 deletion and ferroptosis inhibitors[63]. Ferroptosis is described through lipophilic antioxidant and iron chelation, the accumulation of lipid ROS, and ruling out other forms of cell death, instead of a definitive molecular marker. A significant innovation of the work in chapter three are methods describing the histological features and gene expression patterns occurring during *in vivo* ferroptosis. The methods described here remedy a long-standing limitation in the field by providing a means to characterize ferroptosis *in vivo*. These methods provide tools to identify physiological and developmental roles for ferroptosis.

Triggering Ferroptosis *in vivo*

Harnessing ferroptosis *in vivo* has led to modest results, while its application in cultured cells universally leads to cell death. At current, our work harnessing ferroptosis via *SLC7A11* deletion or cyst(e)inase treatment is the first data demonstrating tumor regression and cell death in a genetically engineered cancer model. Previous reports showed *SLC7A11* deletion delayed PDA tumor engraftment and growth, and cystine/cysteine depletion in established tumors had little effect on tumor growth[64,65]. Corroborating with these studies, dietary dropout of cysteine also had little impact on tumor growth but was modestly enhanced by redox challenge through GOT1 inhibition. Moreover, we and others show that inhibiting glutathione synthesis only slows tumor growth[9]. Mixed results have also been observed for targeting GPX4 *in vivo*[7,14,66–68]. Overall, targeting GPX4 *in vivo* has been more robust in suppressing tumor growth compared with *SLC7A11*. The relative success of this strategy could stem from targeting ferroptosis-sensitive cell states[66–69]. Overall, *SLC7A11* or GPX4 inhibition has led to mixed results *in vivo*.

Several mechanisms could explain the discrepancy between *in vitro* and *in vivo* ferroptosis, including cell-cell contact, the nutrient status of cultured cells versus tumors, and immune competency of the mouse model. A recent report demonstrated that epithelial cancer cells suppress ferroptosis through cellular attachment[70]. High cell density activated Hippo signaling pathway and suppressed the expression of ACSL4 and TFRC, which contribute to ferroptosis sensitivity. Antagonizing this signaling axis restored the expression of these pro-ferroptotic genes and restored ferroptosis sensitivity *in vitro* and, to a lesser extent, *in vitro*. Thus, the high cell density of tumor models is one factor that contributes to ferroptosis resistance *in vivo*.

The differences in cell culture media and dietary composition could also account for the *in vitro* and *in vivo* discordance. The levels of cystine in standard DMEM culture media are four times higher than in PDA tumors[71]. Moreover, cystine levels dictate the extent to which glutamine is taken into the cell and used for glutathione synthesis[72], which would influence ferroptosis sensitivity. A significant effort in the cancer metabolism field is developing medias that better mimic *in vivo* conditions[72–74].

The levels of antioxidants and trace elements in standard rodent diets could influence ferroptosis sensitivity *in vivo*. Vitamin E and butylated hydroxyltoluene (BHT) are supplemented as preservatives for rodent formulations. These lipophilic antioxidants block ferroptosis in cultured cells and would blunt ferroptosis *in vivo*. Moreover, levels of iron, selenium[75], and fatty acids[16,17,76] in food could influence sensitivity to ferroptosis based data from cell culture. While it is established that diet can affect metabolite levels in tumors[77,78] and interstitial space[71], no study has examined how the presence of antioxidants in rodent formulations or dietary components directly influences *in vivo* ferroptosis.

Still, cell contact mechanisms are active, and a standard rodent diet was used in our autochthonous PDA tumors, where we demonstrate ferroptosis *in vivo* and tumor regression. One potential explanation for the efficacy of ferroptosis in autochthonous PDA mouse models could be the harsh metabolic environment of PDA tumors[8]. To test this, we compared the effectiveness of cyst(e)inase on established subcutaneous PDA tumors versus established tumors orthotopically implanted into the pancreas. Both models utilized immune-compromised mice. Cyst(e)inase treatment did not affect tumor growth **(Figure 50)**, suggesting the PDA metabolic environment made little difference for cyst(e)inase treatment. Moreover, cysteine free and cysteine free/low methionine diets had no impact on tumor growth **(Figure 50)**, indicating dietary restriction alone cannot induce *in vivo* ferroptosis. Immune competence may play a more critical role than diet in influencing ferroptosis *in vivo*.

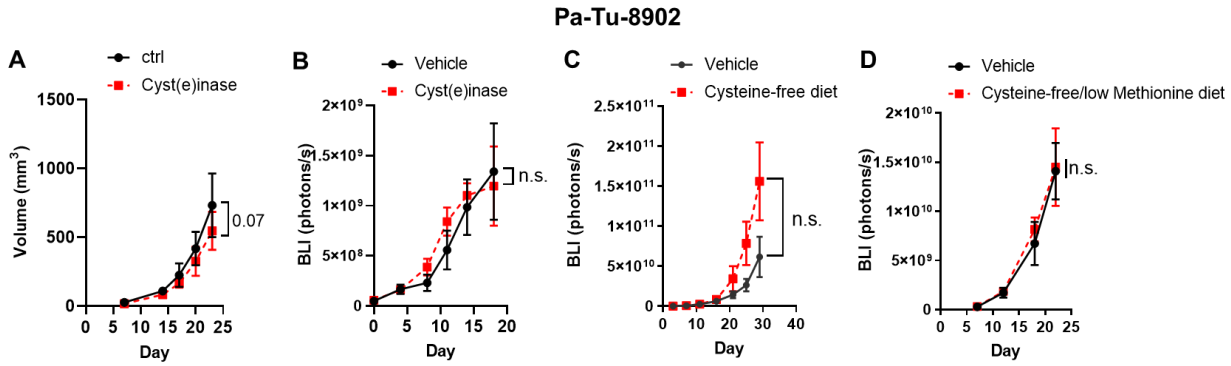

Figure 50. Cyst(e)ine deprevaion fails to initiate ferroptosis in implant models.
A-B) Cyst(e)inease treatment in subcutaneous (A) and orthotopiclly (B) implanted tumors.
C-D) Dietary modulation of cysteine (C) and cysteine with methionine (D) in orthopically implanted tumors.

Recent reports suggest ferroptosis that a competent immune system influences ferroptosis. Experiments utilizing a whole-body conditional GPX4 knockout mouse model (*GPX4*^{fl,fl}-Rosa-CreERT2) demonstrated a strong infiltration of macrophages into damaged kidney tissues[79]. The expression of pro-inflammatory cytokines and infiltration of neutrophils into damaged kidney tissue could be reversed by lipophilic antioxidant treatment in a pharmacological model of acute kidney injury[62]. In cancer models, immune therapy-associated cytokines such as TNFα and IFNγ influence ferroptosis sensitivity[69,80]. *SLC7A11* suppression can induce tumor regressions in combination with CTLA-4 blocking antibodies[81], suggesting a potential role of the immune system in regulating ferroptosis *in vivo*.

Uncovering the mechanism by which the immune system regulates ferroptosis is an exciting avenue with implications for cancer immune therapy. Immune competency likely plays a significant role in regulating ferroptosis *in vivo*.

Harnessing Ferroptosis for Therapy

Ferroptosis and targeted therapy could be harnessed in combination. Recent studies are revealing certain cell states are susceptible to ferroptosis. A panel of cancers resistant to receptor tyrosine kinase (RTK) inhibitors expressing mesenchymal markers were highly sensitive to GPX4 inhibition[67,68]. Given that cancer-associated fibroblasts (CAF) are a significant population contributing to pancreatic cancer survival and immune suppression, it is tempting to speculate that ferroptosis triggering strategies could ablate the CAF population while simultaneously targeting the PDA cells. Moreover, RTK and mitogen-activated protein kinase (MAPK) inhibition-resistant melanoma also susceptible to *SLC7A11* or GPX4 inhibition[69]. MAPK inhibitor combinations are being evaluated in several clinical trials[82]. Future studies should determine if PDA cells can become resistant to MAPK inhibitors and if these drug-tolerant cells are susceptible to ferroptosis. Moreover, Bryant *et al.* recently demonstrated that MAPK inhibition induces autophagy in PDA[83]. Based on our work, MAPK inhibition could induce labile iron release, increase lipid ROS, and render PDA cells susceptible to ferroptosis. Thus, there are several opportunities to explore combinations of ferroptosis with targeted therapies.

Triggering ferroptosis could augment immune checkpoint therapy in PDA. Recent studies have shown that targeting SLC7A11 can augment immune checkpoint therapies[81] and, conversely, lipophilic antioxidant treatment blunts response to immune checkpoint therapies[80]. The pro-inflammatory cytokines TNFα and IFNγ regulate the expression of GPX4 and SLC7A11, respectively[69,80]. These observations raise the exciting possibility that cyst(e)ine deprivation may sensitize PDA with immune checkpoint therapies, which have been ineffective in PDA. Still, these studies were conducted using highly immunogenic mouse cell lines, and it unknown whether the synergy observed would carry over to PDA, which exhibits moderate immunogenicity[84].

It is also tempting to speculate that ferroptosis may render PDA cells more immunogenic. ROS and endoplasmic reticulum (ER) stress mediates the cell surface exposure of calreticulin. Calreticulin is a hallmark of immunogenic cell death, which is a process that primes immune cells to identify cancers[85]. Dying cells communicate with the immune system by releasing 'find me' and 'eat me' signals, suggesting ferroptosis could release signature immunomodulatory signals. For example, cells undergoing ferroptosis release oxidized lipid species, where arachidonate 15-lipoxygenase (ALOX15)-derived lipids regulate dendritic cell maturation and modulate adaptive immune response[86]. Other mechanisms by which ferroptosis modulates the immune system have been reviewed previously[87]. Identifying the mechanisms of ferroptosis-immune cross-talk will be critical for harnessing ferroptosis for cancer immune therapy.

Identifying molecular markers predictive of ferroptosis sensitivity is crucial for therapeutic application in PDA and other cancers. KRAS status could predict ferroptosis sensitivity in PDA. Ferroptosis inducing compounds were first discovered through synthetic lethal screens in mutant RAS cell lines[88]. Many cancer cells have high levels of reactive oxygen species and adapt through the activation of antioxidant genes through the NRF2 transcriptional program **(Figure 42)**[89]. Oncogenic KRAS has been shown to increase the transcription of the NRF2 antioxidant response in pancreatic cancer cells and mouse models. The deletion of NRF2 slowed pancreatic cancer progression[90]. Which NRF2 transcriptional target, and how it contributes to PDA, progression are open questions. *SLC7A11*, iron, and glutathione biosynthetic genes are regulated by NRF2 **(Figure 42)**[89], and would thus influence ferroptosis susceptibility.

SLC7A11 is highly expressed in human tumors[8,80], suggesting the KRAS, NRF2, and SLC7A11 regulatory axis could operate in humans. The unique dependence of cancer cells on SLC7A11 contrasts its dispensability in normal tissue and may be linked to redox stress associated with tumorigenesis.

Given that PDA cells and autochthonous PDA tumors succumb to cystine deprivation, it is tempting to speculate that ferroptosis may be a KRAS dependency. This hypothesis can be tested in cell culture employing doxycycline-inducible KRAS cell lines[19,91]. If KRAS status is predictive of ferroptosis sensitivity, we expect KRAS to augment sensitivity to ferroptosis inducing perturbations. If this effect is due to upregulating *SLC7A11* through NRF2, then KRAS should increase the expression of *SLC7A11* and NRF2. Silencing NRF2 should decrease *SLC7A11* expression and inhibit cystine uptake. We also expect PDA tumors in iKRAS mice to have higher levels of *SLC7A11* through NRF2, measured by immunohistochemistry. Determining if ferroptosis is a KRAS vulnerability and mechanisms by which this occurs is of great interest, given that 90% of PDA patients harbor KRAS mutations.

Future studies should test the possibility that ferroptosis, e.g., cyst(e)inase, can be harnessed with targeted and immune therapies. Further, KRAS and SLC7A11 are highly expressed in human PDA and could serve as potential biomarkers for this therapeutic strategy. Overall, these concepts represent potential translational opportunities for PDA.

5.2 Future Perspective

The multi-disciplinary work presented here provides new resources for the growing fields of mass spectrometry metabolomics and ferroptosis. We propose new therapeutic strategies for pancreatic cancer, a disease where new therapeutic options are desperately needed.

We uncovered new tools to study ferroptosis, which can be used to dissect the role of ferroptosis in physiology, development, and cancer. We identified new nodes in the metabolic regulation of ferroptosis. These discoveries contribute to the growing body of literature, indicating ferroptosis is a metabolically coupled form of necrosis.

Currently, the best modality to trigger ferroptosis is cyst(e)inase, which is in clinical development for the metabolic disorder cystinuria. Future work aims to

determine how metabolism and signaling regulate ferroptosis. These studies could identify therapeutically tractable targets that could expand the arsenal of ferroptosis therapeutics. These studies are critical for determining proper therapeutic context (e.g. molecular markers) to apply ferroptosis inducing agents, such as cyst(e)inase. Future studies should also examine if ferroptosis can be harnessed in combination with targeted therapies or immune checkpoint inhibitors.

5.3 Chapter 5 References

1. Rinschen, M. M., Ivanisevic, J., Giera, M. & Siuzdak, G. Identification of bioactive metabolites using activity metabolomics. *Nat. Rev. Mol. Cell Biol.* **20**, 353–367 (2019).

2. Jang, C., Chen, L. & Rabinowitz, J. D. Metabolomics and Isotope Tracing. *Cell* **173**, 822–837 (2018).

3. Akella, N. M., Ciraku, L. & Reginato, M. J. Fueling the fire: emerging role of the hexosamine biosynthetic pathway in cancer. *BMC Biology* **17**, 52 (2019).

4. Sullivan, L. B., Gui, D. Y. & Heiden, M. G. V. Altered metabolite levels in cancer: implications for tumour biology and cancer therapy. *Nature Reviews Cancer* **16**, 680–693 (2016).

5. Kaelin, W. G. & McKnight, S. L. Influence of Metabolism on Epigenetics and Disease. *Cell* **153**, 56–69 (2013).

6. Dixon, S. J. *et al.* Ferroptosis: An Iron-Dependent Form of Nonapoptotic Cell Death. *Cell* **149**, 1060–1072 (2012).

7. Yang, W. S. *et al.* Regulation of ferroptotic cancer cell death by GPX4. *Cell* **156**, 317–331 (2014).

8. Badgley, M. A. *et al.* Cysteine depletion induces pancreatic tumor ferroptosis in mice. *Science* **368**, 85–89 (2020).

9. Harris, I. S. *et al.* Deubiquitinases Maintain Protein Homeostasis and Survival of Cancer Cells upon Glutathione Depletion. *Cell Metabolism* **29**, 1166-1181.e6 (2019).

10. Harris, I. S. *et al.* Glutathione and Thioredoxin Antioxidant Pathways Synergize to Drive Cancer Initiation and Progression. *Cancer Cell* **27**, 211–222 (2015).

11. Mandal, P. K. *et al.* Loss of Thioredoxin Reductase 1 Renders Tumors Highly Susceptible to Pharmacologic Glutathione Deprivation. *Cancer Res* **70**, 9505–9514 (2010).

12. Llabani, E. *et al.* Diverse compounds from pleuromutilin lead to a thioredoxin Inhibitor and inducer of ferroptosis. *Nature Chemistry* **11**, 521–532 (2019).

13. Doll, S. *et al.* FSP1 is a glutathione-independent ferroptosis suppressor. *Nature* **575**, 693–698 (2019).

14. Bersuker, K. *et al.* The CoQ oxidoreductase FSP1 acts parallel to GPX4 to inhibit ferroptosis. *Nature* **575**, 688–692 (2019).

15. Shimada, K. *et al.* Global survey of cell death mechanisms reveals metabolic regulation of ferroptosis. *Nat. Chem. Biol.* **12**, 497–503 (2016).

16. Magtanong, L. *et al.* Exogenous Monounsaturated Fatty Acids Promote a Ferroptosis-Resistant Cell State. *Cell Chem Biol* **26**, 420-432.e9 (2019).

17. Doll, S. *et al.* ACSL4 dictates ferroptosis sensitivity by shaping cellular lipid composition. *Nature Chemical Biology* **13**, 91–98 (2017).

18. Kagan, V. E. *et al.* Oxidized arachidonic and adrenic PEs navigate cells to ferroptosis. *Nature Chemical Biology* **13**, 81–90 (2017).

19. Ying, H. *et al.* Oncogenic Kras Maintains Pancreatic Tumors through Regulation of Anabolic Glucose Metabolism. *Cell* **149**, 656–670 (2012).

20. Kamphorst, J. J. *et al.* Hypoxic and Ras-transformed cells support growth by scavenging unsaturated fatty acids from lysophospholipids. *PNAS* **110**, 8882–8887 (2013).

21. Ward, N. P. & DeNicola, G. M. Chapter Three - Sulfur metabolism and its contribution to malignancy. in *International Review of Cell and Molecular Biology* (eds. Montrose, D. C. & Galluzzi, L.) vol. 347 39–103 (Academic Press, 2019).

22. Zhu, J. *et al.* Transsulfuration Activity Can Support Cell Growth upon Extracellular Cysteine Limitation. *Cell Metabolism* **30**, 865-876.e5 (2019).

23. Son, J. *et al.* Glutamine supports pancreatic cancer growth through a KRAS-regulated metabolic pathway. *Nature* **496**, 101–105 (2013).

24. Ezeriņa, D., Takano, Y., Hanaoka, K., Urano, Y. & Dick, T. P. N-Acetyl Cysteine Functions as a Fast-Acting Antioxidant by Triggering Intracellular H2S and Sulfane Sulfur Production. *Cell Chemical Biology* **25**, 447-459.e4 (2018).

25. Filipovic, M. R., Zivanovic, J., Alvarez, B. & Banerjee, R. Chemical Biology of H2S Signaling through Persulfidation. *Chem. Rev.* **118**, 1253–1337 (2018).

26. Dixon, S. J. *et al.* Ferroptosis: an iron-dependent form of nonapoptotic cell death. *Cell* **149**, 1060–1072 (2012).

27. Gao, M. *et al.* Role of Mitochondria in Ferroptosis. *Mol. Cell* **73**, 354-363.e3 (2019).

28. Gao, M., Monian, P., Quadri, N., Ramasamy, R. & Jiang, X. Glutaminolysis and Transferrin Regulate Ferroptosis. *Molecular Cell* **59**, 298–308 (2015).

29. Nelson, B. S. *et al.* Tissue of origin dictates GOT1 dependence and confers synthetic lethality to radiotherapy. *Cancer Metab* **8**, 1 (2020).

30. Balsa, E. *et al.* Defective NADPH production in mitochondrial disease complex I causes inflammation and cell death. *Nature Communications* **11**, 2714 (2020).

31. Birsoy, K. *et al.* An Essential Role of the Mitochondrial Electron Transport Chain in Cell Proliferation Is to Enable Aspartate Synthesis. *Cell* **162**, 540–551 (2015).

32. Jiang, L. *et al.* Reductive carboxylation supports redox homeostasis during anchorage-independent growth. *Nature* **532**, 255–258 (2016).

33. Sullivan, L. B. *et al.* Supporting aspartate biosynthesis is an essential function of respiration in proliferating cells. *Cell* **162**, 552–563 (2015).

34. Buck, M. D., Sowell, R. T., Kaech, S. M. & Pearce, E. L. Metabolic Instruction of Immunity. *Cell* **169**, 570–586 (2017).

35. Bailis, W. *et al.* Distinct modes of mitochondrial metabolism uncouple T cell differentiation and function. *Nature* **571**, 403–407 (2019).

36. Anglin, J. *et al.* Discovery and optimization of aspartate aminotransferase 1 inhibitors to target redox balance in pancreatic ductal adenocarcinoma. *Bioorganic & Medicinal Chemistry Letters* **28**, 2675–2678 (2018).

37. Holt, M. C. *et al.* Biochemical Characterization and Structure-Based Mutational Analysis Provide Insight into the Binding and Mechanism of Action of Novel Aspartate Aminotransferase Inhibitors. *Biochemistry* **57**, 6604–6614 (2018).

38. Sun, W. *et al.* Aspulvinone O, a natural inhibitor of GOT1 suppresses pancreatic ductal adenocarcinoma cells growth by interfering glutamine metabolism. *Cell Commun. Signal* **17**, 111 (2019).

39. Yoshida, T. *et al.* A covalent small molecule inhibitor of glutamate-oxaloacetate transaminase 1 impairs pancreatic cancer growth. *Biochemical and Biophysical Research Communications* **522**, 633–638 (2020).

40. DeLaBarre, B., Hurov, J., Cianchetta, G., Murray, S. & Dang, L. Action at a Distance: Allostery and the Development of Drugs to Target Cancer Cell Metabolism. *Chemistry & Biology* **21**, 1143–1161 (2014).

41. Ostrem, J. M., Peters, U., Sos, M. L., Wells, J. A. & Shokat, K. M. K-Ras(G12C) inhibitors allosterically control GTP affinity and effector interactions. *Nature* **503**, 548–551 (2013).

42. Ostrem, J. M. L. & Shokat, K. M. Direct small-molecule inhibitors of KRAS: from structural insights to mechanism-based design. *Nature Reviews Drug Discovery* **15**, 771–785 (2016).

43. Pricer, R., Gestwicki, J. E. & Mapp, A. K. From Fuzzy to Function: The New Frontier of Protein–Protein Interactions. *Acc. Chem. Res.* **50**, 584–589 (2017).

44. Parker, C. G. & Pratt, M. R. Click Chemistry in Proteomic Investigations. *Cell* **180**, 605–632 (2020).

45. Backus, K. M. *et al.* Proteome-wide covalent ligand discovery in native biological systems. *Nature* **534**, 570–574 (2016).

46. Hacker, S. M. *et al.* Global profiling of lysine reactivity and ligandability in the human proteome. *Nature Chemistry* **9**, 1181–1190 (2017).

47. Zheng, Q. *et al.* SuFEx-enabled, agnostic discovery of covalent inhibitors of human neutrophil elastase. *PNAS* **116**, 18808–18814 (2019).

48. Zambaldo, C. *et al.* 2-Sulfonylpyridines as Tunable, Cysteine-Reactive Electrophiles. *J. Am. Chem. Soc.* **142**, 8972–8979 (2020).

49. Thompson Legault, J. *et al.* A Metabolic Signature of Mitochondrial Dysfunction Revealed through a Monogenic Form of Leigh Syndrome. *Cell Reports* **13**, 981–989 (2015).

50. Mootha, V. K. *et al.* Errα and Gabpa/b specify PGC-1α-dependent oxidative phosphorylation gene expression that is altered in diabetic muscle. *PNAS* **101**, 6570–6575 (2004).

51. To, T.-L. *et al.* A Compendium of Genetic Modifiers of Mitochondrial Dysfunction Reveals Intra-organelle Buffering. *Cell* **179**, 1222-1238.e17 (2019).

52. Kühl, I. *et al.* Transcriptomic and proteomic landscape of mitochondrial dysfunction reveals secondary coenzyme Q deficiency in mammals. *eLife* **6**, e30952 (2017).

53. Hughes, C. E. *et al.* Cysteine Toxicity Drives Age-Related Mitochondrial Decline by Altering Iron Homeostasis. *Cell* **180**, 296-310.e18 (2020).

54. Yambire, K. F. *et al.* Impaired lysosomal acidification triggers iron deficiency and inflammation in vivo. *eLife* **8**, e51031 (2019).

55. Fujimaki, M. *et al.* Iron Supply via NCOA4-Mediated Ferritin Degradation Maintains Mitochondrial Functions. *Mol. Cell. Biol.* **39**, (2019).

56. Weber, R. A. *et al.* Maintaining Iron Homeostasis Is the Key Role of Lysosomal Acidity for Cell Proliferation. *Molecular Cell* **77**, 645-655.e7 (2020).

57. Shen, H. An IRON-clad Connection between Aging Organelles. *Cell* **180**, 214–216 (2020).

58. Hamdi, A. *et al.* Erythroid cell mitochondria receive endosomal iron by a “kiss-and-run” mechanism. *Biochimica et Biophysica Acta (BBA) - Molecular Cell Research* **1863**, 2859–2867 (2016).

59. Schoenfeld, J. D. *et al.* O2·− and H2O2-Mediated Disruption of Fe Metabolism Causes the Differential Susceptibility of NSCLC and GBM Cancer Cells to Pharmacological Ascorbate. *Cancer Cell* **31**, 487-500.e8 (2017).

60. Spangler, B. *et al.* A Novel Tumor-Activated Prodrug Strategy Targeting Ferrous Iron Is Effective in Multiple Preclinical Cancer Models. *J. Med. Chem.* **59**, 11161–11170 (2016).

61. Deu, E. *et al.* Ferrous iron-dependent drug delivery enables controlled and selective release of therapeutic agents in vivo. *PNAS* **110**, 18244–18249 (2013).

62. Linkermann, A. *et al.* Synchronized renal tubular cell death involves ferroptosis. *Proc. Natl. Acad. Sci. U.S.A.* **111**, 16836–16841 (2014).

63. Proneth, B. & Conrad, M. Ferroptosis and necroinflammation, a yet poorly explored link. *Cell Death & Differentiation* **26**, 14–24 (2019).

64. Daher, B. *et al.* Genetic Ablation of the Cystine Transporter xCT in PDAC Cells Inhibits mTORC1, Growth, Survival, and Tumor Formation via Nutrient and Oxidative Stresses. *Cancer Res* **79**, 3877–3890 (2019).

65. Kshattry, S. *et al.* Enzyme-mediated depletion of l -cyst(e)ine synergizes with thioredoxin reductase inhibition for suppression of pancreatic tumor growth. *npj Precision Oncology* **3**, 1–13 (2019).

66. Zou, Y. *et al.* A GPX4-dependent cancer cell state underlies the clear-cell morphology and confers sensitivity to ferroptosis. *Nat Commun* **10**, 1617 (2019).

67. Hangauer, M. J. *et al.* Drug-tolerant persister cancer cells are vulnerable to GPX4 inhibition. *Nature* **551**, 247–250 (2017).

68. Viswanathan, V. S. *et al.* Dependency of a therapy-resistant state of cancer cells on a lipid peroxidase pathway. *Nature* **547**, 453–457 (2017).

69. Tsoi, J. *et al.* Multi-stage Differentiation Defines Melanoma Subtypes with Differential Vulnerability to Drug-Induced Iron-Dependent Oxidative Stress. *Cancer Cell* **33**, 890-904.e5 (2018).

70. Wu, J. *et al.* Intercellular interaction dictates cancer cell ferroptosis via NF2–YAP signalling. *Nature* **572**, 402–406 (2019).

71. Sullivan, M. R. *et al.* Quantification of microenvironmental metabolites in murine cancers reveals determinants of tumor nutrient availability. *eLife* **8**, e44235 (2019).

72. Muir, A. *et al.* Environmental cystine drives glutamine anaplerosis and sensitizes cancer cells to glutaminase inhibition. *eLife* **6**, e27713 (2017).

73. Vande Voorde, J. *et al.* Improving the metabolic fidelity of cancer models with a physiological cell culture medium. *Sci Adv* **5**, (2019).

74. Cantor, J. R. *et al.* Physiologic Medium Rewires Cellular Metabolism and Reveals Uric Acid as an Endogenous Inhibitor of UMP Synthase. *Cell* **169**, 258-272.e17 (2017).

75. Stockwell, B. R. *et al.* Ferroptosis: A Regulated Cell Death Nexus Linking Metabolism, Redox Biology, and Disease. *Cell* **171**, 273–285 (2017).

76. Beatty, A. *et al.* Conjugated linolenic fatty acids trigger ferroptosis in triple-negative breast cancer. *bioRxiv* 556084 (2019) doi:10.1101/556084.

77. Maddocks, O. D. K. *et al.* Modulating the therapeutic response of tumours to dietary serine and glycine starvation. *Nature* **544**, 372–376 (2017).

78. Lien, E. C. & Vander Heiden, M. G. A framework for examining how diet impacts tumour metabolism. *Nature Reviews Cancer* **19**, 651–661 (2019).

79. Friedmann Angeli, J. P. *et al.* Inactivation of the ferroptosis regulator Gpx4 triggers acute renal failure in mice. *Nature Cell Biology* **16**, 1180–1191 (2014).

80. Wang, W. *et al.* CD8 + T cells regulate tumour ferroptosis during cancer immunotherapy. *Nature* **569**, 270–274 (2019).

81. Arensman, M. D. *et al.* Cystine–glutamate antiporter xCT deficiency suppresses tumor growth while preserving antitumor immunity. *PNAS* **116**, 9533–9542 (2019).

82. Nevala-Plagemann, C., Hidalgo, M. & Garrido-Laguna, I. From state-of-the-art treatments to novel therapies for advanced-stage pancreatic cancer. *Nature Reviews Clinical Oncology* **17**, 108–123 (2020).

83. Bryant, K. L. *et al.* Combination of ERK and autophagy inhibition as a treatment approach for pancreatic cancer. *Nature Medicine* **25**, 628–640 (2019).

84. Schumacher, T. N. & Schreiber, R. D. Neoantigens in cancer immunotherapy. *Science* **348**, 69–74 (2015).

85. Obeid, M. *et al.* Calreticulin exposure dictates the immunogenicity of cancer cell death. *Nat Med* **13**, 54–61 (2007).

86. Rothe, T. *et al.* 12/15-Lipoxygenase-mediated enzymatic lipid oxidation regulates DC maturation and function. *J. Clin. Invest.* **125**, 1944–1954 (2015).

87. Friedmann Angeli, J. P., Krysko, D. V. & Conrad, M. Ferroptosis at the crossroads of cancer-acquired drug resistance and immune evasion. *Nature Reviews Cancer* **19**, 405–414 (2019).

88. Dolma, S., Lessnick, S. L., Hahn, W. C. & Stockwell, B. R. Identification of genotype-selective antitumor agents using synthetic lethal chemical screening in engineered human tumor cells. *Cancer Cell* **3**, 285–296 (2003).

89. Gorrini, C., Harris, I. S. & Mak, T. W. Modulation of oxidative stress as an anticancer strategy. *Nature Reviews Drug Discovery* **12**, 931–947 (2013).

90. DeNicola, G. M. *et al.* Oncogene-induced Nrf2 transcription promotes ROS detoxification and tumorigenesis. *Nature* **475**, 106–109 (2011).

91. Collins, M. A. *et al.* Oncogenic Kras is required for both the initiation and maintenance of pancreatic cancer in mice. *J Clin Invest* **122**, 639–653 (2012).

Data Appendix

HIF1α is a key transcriptional regulator that allows cancer cells to adapt to low-oxygen conditions. HIF1α stabilization by hypoxia has profound effects on cellular metabolism. HIF1α increased anaerobic glycolysis and glutamine-mediated reductive carboxylation to support cell proliferation[1]. Pervious data have suggested that Hypoxia-inducible factor-1α (HIF1α) can suppress GOT1 expression in VHL-deficient human

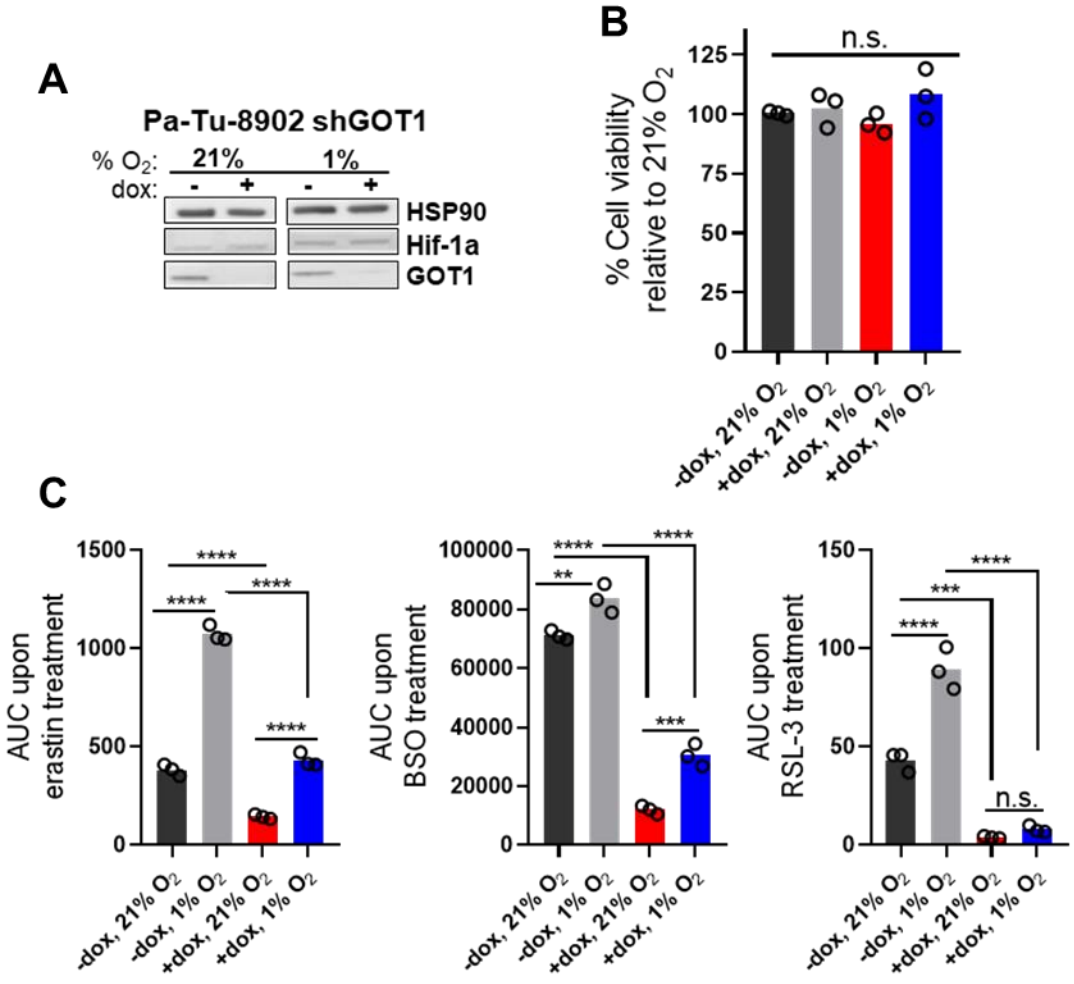

Figure 51. Influence of atmospheric oxygen on GOT1 inhibition and ferroptosis.
A-B) Hif-1 induction and effect on cell viability (B) following GOT1 and oxygen modulation.
C) Effect of atmospheric oxygen levels on ferroptosis sensitivity in Pa-Tu-8902 iDox-shGOT1 cells.

renal carcinoma (RCC)[2]. We thus wondered how hypoxia would regulate GOT1 expression and if hypoxia would affect cell viability, given that PDA tumors are highly hypoxic. To test this we cultured GOT1 proficient and knockdown PDA cell lines under normoxia (21% O_2) and hypoxia (1% O_2). Hypoxia stabilized HIF1α, but did not alter GOT1 expression **(Figure 51a)**, as in RCC cell lines[2]. Hypoxia did not affect cell viability **(Figure 51b)**. Hypoxia modulates all enzymes that utilize O_2, an alternative experiment to test if HIF stabilization would directly modulate GOT1 expression would be to inhibit negative regulators of HIFs, using the PHD inhibitor FG-4592.

Because ferroptosis is an oxidative form of cell death, we wondered how hypoxic conditions would influence ferroptosis sensitivity. Previous data indicate that hypoxia had no effect on ferroptosis in HT-1080 and DU-145[3]. To test this in pancreatic cancer we treated GOT1 proficient and knockdown Pa-Tu-8902 iDox-shGOT1 cells with erastin, BSO, and RSL3 for 24 hours and assessed the effect on cell viability. To our surprise, we found that hypoxia uniformly blunted the response to ferroptosis inducers **(Figure 51c)**. Oxygen is a substrate for lipoxygenase enzymes which execute lipid peroxidation[4], thus hypoxia could suppress ferroptosis in some cell types. GOT1 inhibition restored ferroptosis sensitivity, which could be attributed to labile iron release, however future studies would need to demonstrate labile iron release under hypoxic conditions.

References:

1. Fendt, S.-M. *et al.* Reductive glutamine metabolism is a function of the α-ketoglutarate to citrate ratio in cells. *Nat Commun* **4**, 2236 (2013).

2. Meléndez-Rodríguez, F. *et al.* HIF1α Suppresses Tumor Cell Proliferation through Inhibition of Aspartate Biosynthesis. *Cell Reports* **26**, 2257-2265.e4 (2019).

3. Dixon, S. J. *et al.* Pharmacological inhibition of cystine–glutamate exchange induces endoplasmic reticulum stress and ferroptosis. *eLife* **3**, e02523 (2014).

4. Conrad, M. & Pratt, D. A. The chemical basis of ferroptosis. *Nature Chemical Biology* **15**, 1137–1147 (2019).